Multiscale Modeling of Polymer-Colloid Interactions in Waterborne Coatings

by

Alyssa Travitz

A dissertation submitted in partial fulfillment
of the requirements for the degree of
Doctor of Philosophy
(Macromolecular Science and Engineering and Scientific Computing)
in the University of Michigan
2021

Doctoral Committee:

Professor Ronald G. Larson, Chair
Dr. Heather B. Mayes, National Renewable Energy Laboratory
Professor Michael J. Solomon
Professor Emeritus Alan S. Wineman

Alyssa Travitz
atravitz@umich.edu
ORCID iD: 0000-0001-5953-8807

ACKNOWLEDGEMENTS

I first want to thank my advisor, Professor Ronald G. Larson, for welcoming me into your research group when I was a first-year student with no computational background, and for your patience and guidance as I developed these entirely new skillsets. Thank you for being an example of not only an extraordinary scientist and mentor, but also an incredibly kind and generous person.

I would also like to thank the rest my thesis committee: Professor Michael Solomon, Dr. Heather Mayes, and Professor Alan Wineman, for your encouragement and guidance from candidacy now through graduation.

I am fortunate to have so many incredible mentors and colleagues at U-M. This thesis would would not exist without Professor Elnaz Hajizadeh, who I hope I've made proud with my contributions to Pop-BD. I also want to thank Dr. Ryan Marson for introducing me to colloidal simulations, and for being the mentor I most try to emulate when training new students. Thank you both for for your warm welcomes to the Larson group. To Prof. Ethayaraja Mani, it's been a joy working with and learning from you on challenging problems. And to Dr. Joshua Anderson, thank you for your patience and guidance in navigating HOOMD-blue.

I want to thank the entire Macro community for creating such a supportive and caring environment. Julie Pollak and Adam Mael, you have both been constant sources of support and reassurance, I can't imagine trying to navigate graduate school without you. Leanna, Rosy, Ryan, Harry, and all the other POLY/PMSE and REACT folks, thank you for making these such special student organizations. Ayśe Muñiz, thank you for being my co-leader in so many things and for making enormous undertakings feel easy. I'm so proud of the work we've done. To Nisha Hollingsworth, Grace Tan, Bradley Dice, Julia Dshemuchadse, and all the other folks in the office past and present too many to name, thanks for making it a great place to do research.

Last but not least, I want to thank my friends, family, and teachers for getting me to the point that I could attempt this at all. To Rick Leuschner and Marcus Roush, thank you for teaching me to love chemistry and math, and for always expecting the best from me. Nikki Moore, thank you

for feeling like family, always picking up the phone, and reminding me that materials science is the coolest. Thanks to Emily Bayer, for the meticulously planned summer adventures and constant validation. I have to thank my dog, Comet, for holding me to a strict sleep schedule and reminding me to go for walks every day. Mom, Dad, and Gregg, thank you for everything, but mostly for your constant support and always finding a way to make things happen. To Andy - thank you for being here for all of it the past 12 years, and for everything wonderful that is ahead of us.

TABLE OF CONTENTS

LIST OF FIGURES

FIGURE

LIST OF TABLES

TABLE

ABSTRACT

Formulations containing rheology modifying polymers and nanometer sized colloids have widespread use in pharmaceuticals, personal care products, and waterborne coatings. When combined in solution, hydrophobic endcaps of the polymers temporarily adsorb to the colloids and act as bridges, forming a dynamic network with characteristic timescales spanning many orders of magnitude. It is computationally infeasible to capture the full range of relaxation times while maintaining atomistic resolution, but the coarse-grained hybrid population balance-Brownian dynamics model (Pop-BD) has been shown to capture qualitative behavior consistent with more fine-grained models[10, 11]. In this work, we detail efforts to improve Pop-BD to be more accurate, simulate experimentally relevant system sizes, and capture long timescale behavior. In the chapter 2, we quantify the inter-colloidal repulsions induced by adsorbed polymers using a combination of Brownian dynamics simulations and self-consistent field theory. With predictions of particle interactions that account for polymer defects and non-uniform surface coverages, we can predict phase behavior of these mixtures and inform the inter-colloidal potentials used in Pop-BD. In chapter 3, we use Brownian dynamics simulations to quantify bridge-to-loop and loop-to-bridge transition rates that are crucial to capturing dynamic behavior in Pop-BD. We show that the ratio of the fraction of polymers in the bridge configuration to the fraction of those in the loop configuration is equal to the ratio of the bridge-to-loop time to loop-to-bridge time, so that by using the equilibrium bridge and loop configuration information from the self-consistent field theory approach in chapter 2, we can easily compute the slower loop-to-bridge time from the bridge-to-loop time. In studying bridge-to-loop transition times, we observe two distinct regimes, one where the polymer relaxation time dominates for weak hydrophobes and long chains, and another, for strong hydrophobes and short chains, where the hydrophobe desorption time dominates and transition

time scales exponentially with the hydrophobic strength. The complexities seen in the scaling of the bridge-to-loop times indicate that Brownian dynamics simulations are currently necessary for experimentally-relevant parameters, and so we present bridge-to-loop and the corresponding loop-to-bridge transition times for the systems of interest. Chapter 4 contains a thorough investigation of existing theories for modeling the escape of a particle from an adsorptive surface along with a general equation for predicting this escape time across all damping regimes. The Brownian (overdamped) escape times from this study are additionally used to understand the bridge-to-loop transition in Chapter 3. In Chapter 5, we drastically improve the computational efficiency of Pop-BD by integrating it into HOOMD-blue, adopting on-the-fly correlator, and introducing dynamic bonding functionality. We also incorporate the findings from the smaller-scale models in chapters 2-4 into the Pop-BD model so that it may capture the complexities of polymer-colloid interactions more accurately. In doing so, we have made significant progress toward developing the first multi-scale model to understand and predict the behavior of these formulations with the ultimate goal of aiding the formulation development process for waterborne coatings.

CHAPTER 1

Introduction

1.1 Introduction to Waterborne Coatings

Waterborne coatings offer a cost-effective and environmentally friendly alternative to more traditional solvent-based coatings, which rely on volatile organic compounds (VOCs) [12]. However, their rheological behavior is significantly different from that of the more established VOC-based coatings and can be challenging to formulate. Qualities such as poor levelling, short open time, and strong shear-thinning behavior all contribute to the difficulty of formulating a waterborne coating with a precise viscosity profile [13]. Computational models can aid this formulation process by providing insight into and predictions of waterborne coatings' rheological behavior.

The primary components of waterborne coatings are water, colloidal particles (often latex), pigments, rheology modifying polymers, and surfactants, as shown in Fig.1.1 and Table 1.1. Rheology-modifying polymers are added to colloidal suspensions in water to control viscosity at relatively low colloidal volume fractions [9]. Common rheology-modifying polymers, such hy-

Component	**Example**	**Concentration**	**Size**
colloidal particles	Latex	5-35% (vf)	100-300 nm diameter
rheology-modifying polymers	HEUR	0.02-5% (w/w)	30-65 kg/mol
pigments	TiO2	7% (vf)	300-10,000 nm diameter
surfactants	SDS	0.1-1% (w/w)	288 g/mol

Table 1.1: Typical composition of a latex paint formulation [9]. A common surfactant, sodium dodecyl sulfate, is abbreviated as SDS.

drophobically modified ethylene oxide urethanes (HEUR), are telechelic polymers that consist of hydrophilic poly(ethylene oxide) (PEO) backbones with hydrophobic regions, or "stickers". The hydrophobic groups typically end-cap the PEO backbone, making a telechelic polymer, but can also be incorporated along the backbone. Solutions of only rheology modifying polymers and water been studied extensively and have complex rheological behavior. Below their critical micelle concentration (CMC), HEUR solutions have very low viscosities. At moderate concentrations just above the CMC, the HEURs self-assemble into flower-like micelles with hydrophobic cores and

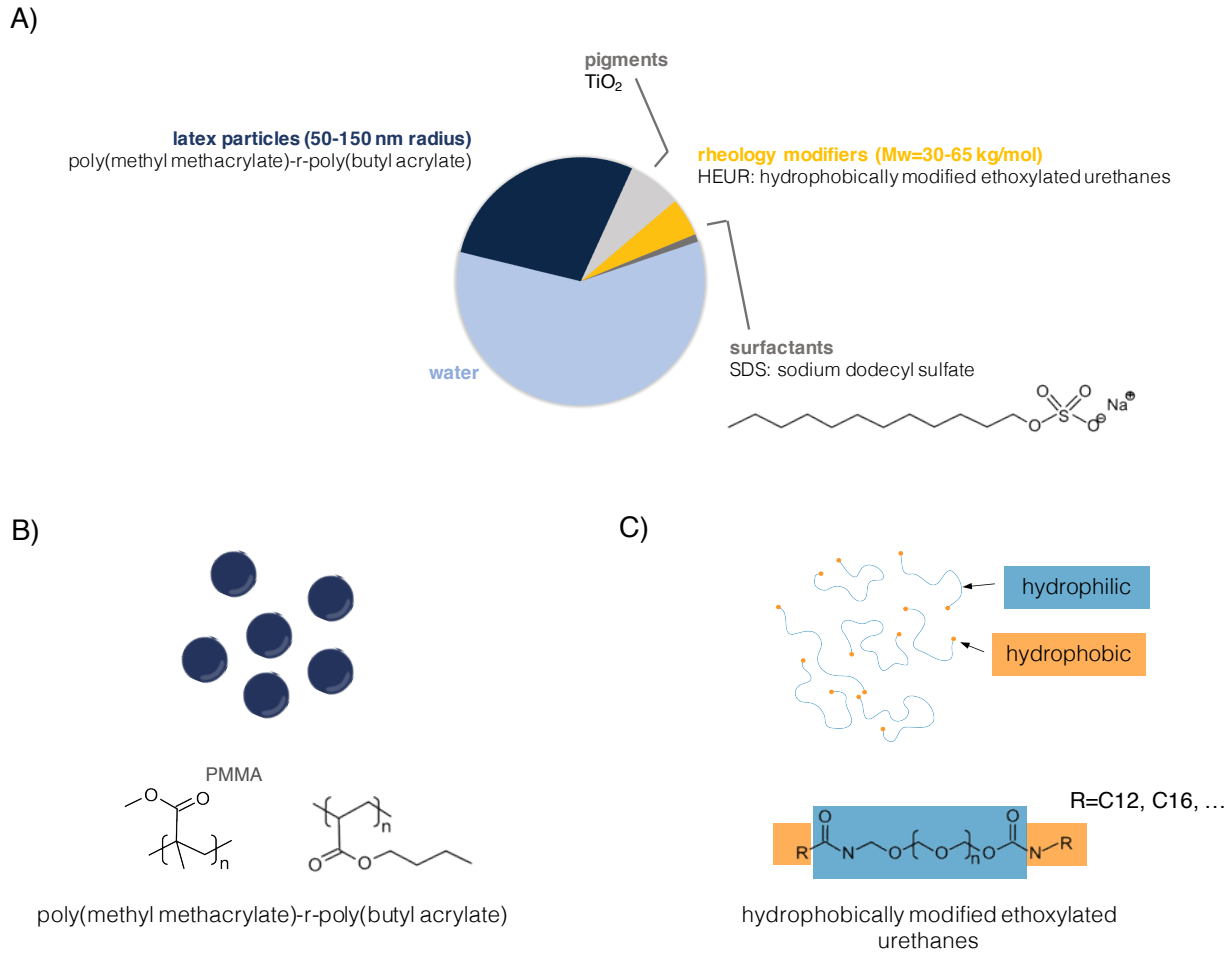

Figure 1.1: A) Approximate composition of a waterborne coating formulation, precise values given in Table 1.1. B) Colloidal latex particles and chemical structure of a common latex poly(methyl methacrylate)-r-poly(butyl acrylate). C) Chemical structure of hydrophobically-modified ethoxylated urethanes where hydrophilic region is highlighted in blue and hydrophobic end cpas are highlighted in yellow.

hydrophilic (PEO) coronas [14]. At higher concentrations, bridges begin to form between adjacent micelles, where the end cap from one HEUR is in the center of one micelle, and its second end cap is in the center of the adjacent micelle [15]. When concentrations are high enough to have many bridges, it is possible for a percolative or gelled network to form.

Because the hydrophobic interactions between the stickers are relatively weak (and of the same order of magnitude as the thermal vibrations in the system), the bridges between micelles can continually break and reform, leading to interesting rheological behavior. For example, network solutions of HEURS exhibit a non-monotonic viscosity vs. shear stress profile. At moderate shear stress, the bridges between the micelles are stretched and these spring stretching forces cause shear-thickening behavior. When shear stress is sufficiently high, the bridges then break and the formulation shows shear thinning behavior. Tanaka and Edwards determined that the relaxation of a transient network of telechelic polymers is dependent on the escape time of a sticker end from a hydrophobic micelle core. They defined this relationship as $\tau = \tau_0 \exp[\Delta G/k_B T]$, where ΔG is the free energy cost of the sticker leaving the micelle and $\tau_0 \sim 1 - 10$ ns [16]. Tam et al. expanded on this model in their experimental studies and developed a structural model to explain the Maxwellian behavior at low shear stress, shear-thickening at moderate shear stress, and shear-thinning at high shear stresses.

Although there are extensive theoretical and experimental studies of transient polymer networks, the addition of colloidal particles to an aqueous solution of telechelic polymers introduces further rheological complexities. At very dilute concentrations of colloids, there is a decrease in viscosity due to the hydrophobic stickers adsorbing to colloids and interrupting the network. At sufficiently high concentrations, the ”gallery spacing”, or gap, between colloids is small enough that polymer bridges between colloids form, resulting in a net increase in viscosity [6]. Beshah et al. demonstrated through diffusion-weighted pulsed field gradient NMR that essentially all hydrophobes are absorbed to colloid surfaces at typical formulation concentrations. These results established the currently accepted model of loops with sticker ends adsorbed to the colloid surfaces, with and bridges forming when a the sticker ends adsorb to neighboring colloids [17]. This

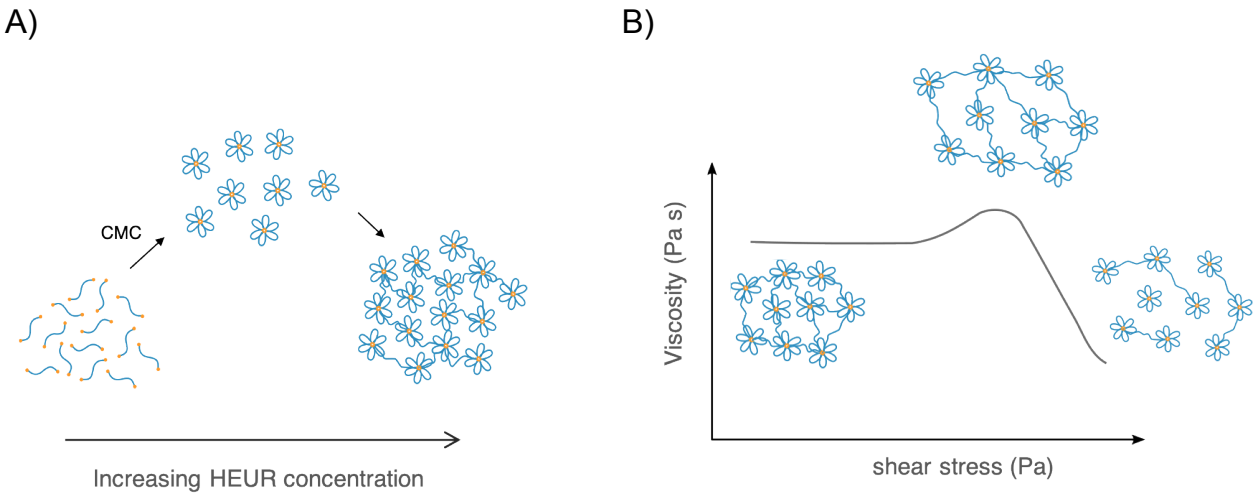

Figure 1.2: A) Diagram showing self-assembly of HEUR flower-like networks formation for increasing concentration in water, where "CMC" refers to the critical micelle concentration, adapted from Tam et. al [1]. B) Diagram showing HEUR network response for increasing shear stress and the resulting non-monotonic viscosity, adapted from Yekta et. al [2].

is in contrast to the prior model that treated the composition as primarily flower-like micelles with some colloids acting as nodes [18]. At concentrations where a viscosity increase is observed, the viscosity of these polymer-colloid mixtures is often at least an order of magnitude higher than the viscosity of either of the constituents alone [13]. In addition to this synergistic viscosity-building, polymer-colloid mixtures exhibit multiple relaxation times, in contrast to the single relaxation time typically seen in pure HEUR solutions. Experimental data alone cannot explain the molecular arrangements responsible for this complex rheology, but simulations offer a method to connect analytical theory and experimental results in an effort to explain and predict the phase behavior, structure, and dynamics of these complex polymer-colloid interactions in waterborne coatings.

1.2 Overview of Models of Waterborne Coatings at Multiple Scales

The work in this thesis builds on many years of simulations aimed at modeling waterborne coatings by understanding the small-scale interactions between components. Yuan and Larson presented a

coarse-grained model based on atomistic simulations of HEUR polymers that predicted escape times of hydrohobes from the HEUR micelle core that are in agreement with experimental data [19]. At the same time, Wang and Larson took a similar approach, but to parameterize an implicit-solvent model of PEO from explicit-solvent and atomistic models. They used this implicit-solvent PEO model to simulate hydrophobe end-capped PEO molecules on the order of 100 monomomers in length and showed good agreement between their predicted phase separation concentrations and experimental data [20].

Ginzburg and coworkers expanded on this coarse-graining to model the adsopriton of HEURs on latex surfaces, additionally incorporating a self-consistent field theory method to access a wider parameter space of interest to expermentalists. They were able to show that structures of the adsorbed HEUR layers include admicelles and suggest that micelles in solution may form nodes that allow for two HEUR polymers to join and span colloidal particles as a two-component bridge [21]. In 2018, Rezvantalab and Larson used Brownian dynamics simulations along with forward flux sampling to model the multimode transition of a polymer chain from the loop configuration to bridge configuration. They also show the feasibility of a high, 20-to-1, degree of coarse-graining for modeling polymer chains without excluded volume [11]. The two models that immediately pre-date this work and simulate both colloidal particles and rheology-modifying polymers are the FENE-BD model presented by Wang and Larson and the Population-Balance Brownian Dynamics model, presented by Hajizadeh, Yu, and Larson [10, 22].

FENE dumbbell Brownian dynamics model The FENE dumbbell Brownian dynamics (FENE-BD) model is able to capture multiple relaxation times characteristic of latex colloids in solution with HEUR polymers [22]. In this model, colloids are represented as spheres with excluded volume defined by a Weeks-Chandler-Anderson potential and HEUR polymers are represented as finitely extensible nonlinear elastic (FENE) dumbbells. The dumbbell ends, representing the hydrophobic end caps of the HEUR molecules, are modeled as having no excluded volume. The hydrophobic attraction between the dumbbell and the colloid surface is represented as a shifted Lennard Jones

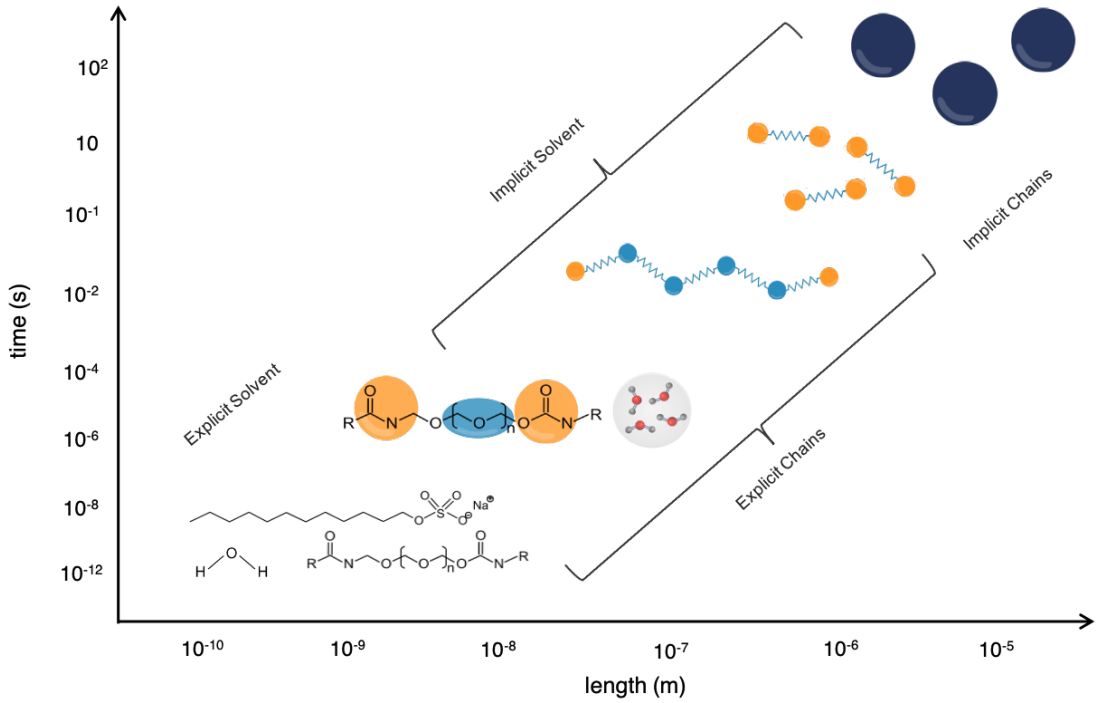

Figure 1.3: Schematic depicting varying degrees of coarse-graining from atomistic (bottom left) up to Pop-BD (top right), with increasing degree of coarse-graining from left to right.

potential where the attractive strength between the dumbbell beads and the colloids is mapped to the strengh of the hydrophobic end-cap of a HEUR polymer, or approximately $6-10k_BT$, meaning that the dumbbell beads and bind and unbind from the colloidal surface during the simulation. The FENE-BD model qualitatively captures four distinct relaxation times, which from shortest to longest timescale are attributed to (1) chain stretching, (2) translational-rotational rearrangements of polymer loops over the colloidal surface, (3) loop/bridge transitions, and (4) particle or particle cluster relaxation. It is important to note that this model captures the characteristic behavior of such polymer-colloid formulations, but is computationally limited to small colloids and few particles because it must resolve every polymer in the system as two beads and one spring bond.

Population Balance Brownian Dynamics The Population Balance Brownian dynamics (Pop-BD) model was developed as the next level of coarse-graining after the FENE-BD model. As such, the Pop-BD builds off of and is validated by the FENE-BD model. The colloid-colloid

repulsions remain modeled as Weeks-Chandler-Anderson potentials, but rather than a dumbbell representation of the telechelic polymers, only the spring force from bridging is applied between the two colloids' centers of mass. A key advantage of Pop-BD is that it scales independently of the number of polymer chains in the system, since the polymers are represented implicitly. Pop-BD considers only bridge and loop polymer configurations, because dangling and free-chains are rare at the concentrations of interest [18]. The number of bridges per particle pair at each time step is determined by the population balance algorithm, which includes bridge-to-loop and loop-to-bridge transition rates. The loop-to-bridge rate, $L(d_{ij})$ is defined as

$$L(d_{ij}) = \Omega \exp\big[- \frac{1}{k_B T}(\Delta G + U_S(d_{ij} - r_c))\big] \tag{1.1}$$

and the loop formation (bridge destruction) rate, $M(d_{ij})$ is defined as

$$M(d_{ij}) = \Omega \exp\big[- \frac{1}{k_B T}(\Delta G - U_S(d_{ij}) + U_S(d_{ij} - r_c))\big] \tag{1.2}$$

where $\Omega = 1.2 \times 10^9 s^{-1}$ is the thermal fluctuation frequency, determined fitting the stress relaxation predictions to those of the FENE-BD model. ΔG is well depth of the attraction potential, r_c is the width of the potential well, and the spring potential $U_s(d)$ is equivalent to U_{FENE} described in the FENE-BD model.

As seen in Figure 1.4, the efficiency of Pop-BD comes with the caveat that short timescale behavior (on the order of 1×10^{-9} seconds) is lost because the rearrangement and hydrophobe fluctuations that are captured by the FENE-BD model are not accounted for. However, long timescale behavior is the primary focus of experimental data, and so the convergence of Pop-BD to the FENE-BD simulations is satisfactory for the end-goal of predicting experimental behavior.

1.3 Objectives and Outline

The primary aim of this thesis is to inform and improve the coarse-grained Pop-BD model through a series of finer-grained studies that investigate the complex interactions between the telechelic rheology-modifying polymers and colloidal particles in waterborne coatings. In Chapter 2, we model the intercolloidal potential between two interacting colloids with coronas of telechelic polymers adsorbed to their surfaces. We use a lattice self-consistent field theory approach that is informed and validated by Brownian dynamics simulations. This study shows that when the colloids are squeezed together, the polymer loops rearrange on the colloids' surfaces to create a long range and relatively weak intercolloidal potential. Using this same self-consistent field theory method, we predict overall effective potentials that account for the attractive contributions of the polymer bridges at equilibrium. From simulations using these potentials we offer insights into defects leading to phase stability in experimental systems.

Chapters 3 and 4 focus on capturing the dynamic behavior of the hydrophobic end caps on telechelic rheology-modifiers. In chapter 3, we simulate the polymers transitioning between loop

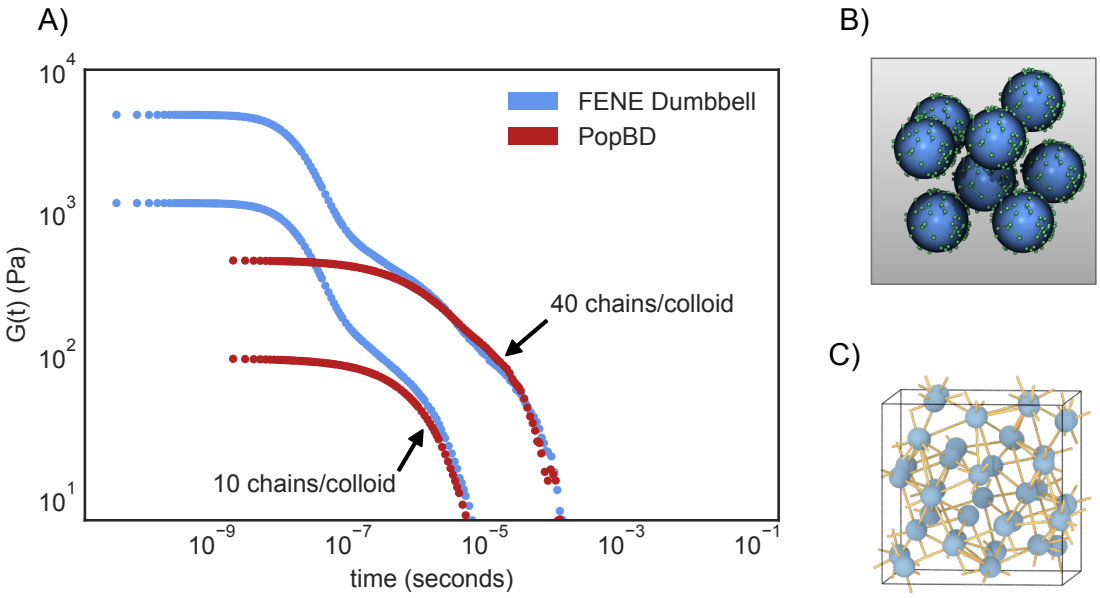

Figure 1.4: A example of stress relaxation curves compute from the Pop-BD method (red) and the FENE-BD (blue) method for 10 and 40 polymer chains per colloid, as indicated in the figure. B) A simulation snapshot of a FENE-BD simulation and C) a Pop-BD simulation .

and bridge configurations, approximating the colloids as flat surfaces. We show that using the equilibrium number of bridges and loops, from the self-consistent field theory approach in chapter 2, to relate the bridge-to-loop and loop-to-bridge transitions times allows us to focus only on simulating the faster bridge-to-loop transition. From Brownian dynamics simulations of experimentally relevant system sizes, we present a complete picture of transition times between surfaces for a wide parameter space. Chapter 4 supports the work in chapter 3, in that it focuses specifically on the escape of a lone hydrophobe (not connected to a HEUR) from an adsorptive wall, but also investigates the transition from underdamped to overdamped particle motion. We perform Langevin and Brownian dynamics simulations and compare the simulated escape times to three theories from Kramers, Mel'nikov and Meshkov (MM), and Larson and Lightfoot (LL). We show that the more commonly used Kramers and MM approaches do not apply to a Lennard-Jones potential for an overdamped particle. By combining the MM theory in the underdamped regime and the LL theory in the overdamped regime, we present a comprehensive approach to predicting the escape of a particle from a Lennard-Jones potential for all damping regimes.

In chapter 5, we extend the functionality of the open-source simulation software, HOOMD-blue, sothat it can perform Pop-BD simulations with signficantly improved efficiency. We also apply the work from chapters 2 and 3 to improve the accuracy of the Pop-BD method. From chapter 2, we include intercolloidal potentials calculated by self-consistent field theory that account for softer, longer range interactions induced by the the polymer loops. From chapter 3, we introduce bridge-to-loop and loop-to-bridge rates to PopBD that account for the more complicated transitions observed in our simulations. This new, updated, Pop-BD model is able to simulate experimentally-relevant system sizes efficiently enough to capture long timescale behavior and account for the complex polymer-colloid interactions we observe in our more detailed studies.

CHAPTER 2

Modeling Intercolloidal Interactions Induced by Adsorption of Mobile Telechelic Polymers onto Particle Surfaces

2.1 Abstract

We combine self-consistent field theory and the Derjaguin approximation to predict the polymer-induced colloidal interactions and the non-uniform distributions of loops and bridges of telechelic polymers adsorbed onto particle surfaces when the polymers are compressed or stretched as a function of inter-particle distance. We validate our approach by comparing its predictions to those of Brownian dynamics simulations. We also determine the dependence of inter-colloidal interactions on particle size and surface coverage as well as molecular structures of telechelic polymers, including chain length and missing associating ends, which are important parameters in the design of commercial latex coatings. By mapping the predicted inter-particle interaction strengths to Baxter temperatures, we can quantitatively predict the phase behaviors of mixtures of colloids and

telechelic polymers.

2.2 Introduction

Amphiphilic polymers can selectively adsorb onto different surfaces in aqueous solutions. For example, the hydrophobic ends of telechelic polymers can adsorb onto the hydrophobic surfaces of colloids, leading to the formation of polymer loops on single particles and bridges between two nearby particles. These loops and bridges thus induce effective interactions between particles, which in turn affect the assembly and flow behaviors of colloid/polymer mixtures for a wide variety of biological and synthetic fluids, such as blood, in which platelet-polymer plugs assemble at the site of injury[23, 24], and waterborne coatings [25, 17].

The strength and range of the induced interactions in such polymer/colloid suspensions depend on many factors, including the polymer lengths and architectures, and surface densities of the associating polymers, as well as the size of the colloids. Polymers with one associating block per chain can only form dangling chains, that induce only repulsive interactions between colloids[26, 27]. Telechelic polymers with two associating ends, one at each end of the chain, can generate short-ranged attraction by forming bridges between the surfaces of two colloids[28, 29, 30, 31]. Such an attraction may induce the formation of a transient network of particles that in turn affects the rheology of the colloidal suspension[17]. Predicting the effective interactions induced by telechelic polymers would be useful for designing polymer/colloid mixtures, such as latex paints.

However, analytical tools for predicting quantitatively these polymer-induced effective potentials for colloids are still mostly lacking. While particle-based simulations have been applied to predict the colloidal interactions induced by associating polymers, they generally are limited to small particles[26, 27] or low surface densities of polymer[31] to keep computational costs manageable. Self-consistent field theory (SCFT) calculations, on the other hand, have been used to calculate interactions induced by telechelic polymers between two flat surfaces[28] and the swelling of the center B block in lamellar ABA triblock copolymer mesogels[32], but to date have not been

used for polymers bridging particle pairs. Indeed, while calculations in bi-spherical coordinates have been performed for phantom telechelic chains on two particles[29], SCFT calculations in bi-spherical coordinates, however, are numerically expensive for telechelic chains with excluded volume interactions. While brush theory (under the strong stretching approximation)[33, 34], together with the Derjaguin approximation, has been used to approximate the interactions between large colloids coated by telechelic chains[30],this approach neglects fluctuations of chain configurations about their classical paths and may only work for colloids coated with strongly stretched brushes.

The methods mentioned above also neglect the fact that polymers under compression can migrate away from the zone of near contact between particles, since the associating ends are not chemically bound to the particle surfaces. Such rearrangements of polymers can lead to non-uniform distributions of chains and reduced effective repulsions at small inter-particle distances. In fact, Pincus and coworkers predicted using a scaling approach that such redistribution can occur for "polymer mushrooms" compressed between the flat surface on which they adsorbed and a parallel disk[35]. We expect that a similar rearrangement may occur for semidilute telechelic brushes on colloids under compression due to presence of another nearby particle.

Here, we develop a theoretical approach that combines SCFT and the Derjaguin approximation to calculate the effective interactions induced by telechelic polymers that may slide along colloid surfaces to avoid compressed zones, thereby giving rise to changes in translational entropy. We minimize the total free energy of the polymers, including both the compression free energy and translational entropy, with respect to the local surface density to obtain the non-uniform distribution of the polymers. At small inter-particle distances, polymers tend to escape from the small-gap region between the poles of particles. In this way, excluded volume interactions among the polymers are reduced at the cost of reduced translational entropy. We validate our predictions by comparing them to those of direct Brownian dynamics (BD) simulations. Using these simulations, we also show that the rearrangement of polymers on particle surfaces becomes less pronounced as the average polymer surface density increases.

For colloids coated rather densely with telechelic chains, we assume a uniform surface distribution of polymers and predict the interactions between a pair of colloids as a function of the number of telechelic bridges. Because the dynamic breakage and formation of bridges and loops can lead to slowly-varying inter-particle forces, the bridge-dependent potentials will be useful for constructing coarse grained models for predicting the rheological behaviors of telechelic polymer/colloid mixtures in flows[10].

Because excluded volume interactions near colloidal surfaces can stretch real polymers and in turn promote the formation of telechelic bridges, the bridge-dependent potentials would also be helpful for improving the previous predictions of loop-to-bridge transition rates, obtained by treating telechelic polymers as phantom and multi-mode Rouse chains[11].

Finally, we demonstrate that varying surface densities and lengths of telechelic chains can modulate the strength and range of effective interactions between colloidal particles. We also predict that by incorporating small fractions of chains with missing telechelic ends (as is typical in commercial products), the attractive interactions between colloids are significantly reduced, which may help explain the stability of commercial latex suspensions with telechelic polymers against phase separation.

2.3 Methods

2.3.1 Theory for polymers adsorbed uniformly on colloids

Slow transitions between the loop and bridge states of telechelic polymers prevent direct sampling of the equilibrium potential of mean force between colloids in molecular simulations. We therefore combine self-consistent field theory (SCFT), the Derjaguin approximation, and the calculus of variations to predict the effective interactions induced by mobile telechelic polymers on colloidal particles.

The free energies and configurations of telechelic chains are first calculated using a lattice version of self-consistent field theory, which has been successfully applied to describe many

interfacial phenomena, including chain adsorption onto a surface and gradient copolymer self-assembly[36, 37, 28, 38, 39, 40]. In the lattice SCFT, we treat the telechelic chains as random walks of Kuhn segments on a pseudo-one-dimensional lattice with discrete distances from the surface $\{h_i\}$, biased by a chemical potential field $W(h_i)$. The value of h_i represents the spatial location of the ith lattice layer. The lattice spacing in our work equals the Kuhn length l_k of PEO (1.1 nm) so that each lattice site represents a layer of PEO solution with a thickness of l_k. In this way, our results can be mapped onto hydrophobically modified ethoxylated urethane (HEUR) polymer, a rheology modifier used in waterborne coatings. The hydrophilic interior monomers of HEUR are PEO segments.

The chemical potential field $W(h_i)$ arises from the excluded volume interactions between Kuhn monomers. Here we assume that polymer segments interact via pair-wise excluded volume interactions:

$$\frac{W(h_i)}{kT} = v\rho(h_i) \tag{2.1}$$

where v is the excluded volume of a Kuhn segment and ρ is the local number density of Kuhn monomers (in units of l_k^{-3}).

We assume a strong short-ranged attraction between the chain ends and particle surfaces so that the conditional Boltzmann factors (propagators) for placing the first monomer is non-zero only in the surface layer:

$$p(h_i, 1) = \begin{cases} e^{-W(h_i)/kT} & \text{if } h_i = \text{surface layer,} \\ 0 & \text{if } h_i \neq \text{surface layer,} \end{cases} \tag{2.2}$$

In this way, telechelic chain ends always absorb on colloid surfaces and no dangling chains can form. The second argument in the function $p(h_i, n)$ is the chain coordinate, ranging from 1 to N in numbers of Kuhn monomers, along the chain.

For chains between two flat surfaces, the initial propagator is zero everywhere except at the left

(h_1) and right (h_L) surfaces:

$$p_r(h_1, 1) = e^{-W(h_1)/kT}$$
$$p_l(h_L, 1) = e^{-W(h_L)/kT} \tag{2.3}$$

in which r and l denote the right and left surfaces, respectively, and L is the total number of lattice layers. Tracking the evolution of Boltzmann factors from $p_r(h_1, 1)$ and $p_l(h_L, 1)$ separately allows us to calculate the fractions of loops and bridges.

The evolution of the conditional Boltzmann factor is governed by a recursion relation, which is a discretized version of the SCFT propagator equation:

$$p(h_i, n) = [\lambda_- p(h_{i-1}, n-1) + \lambda_0 p(h_i, n-1) + \lambda_+ p(h_{i+1}, n-1)]e^{-W(h_i)/kT} \tag{2.4}$$

The transition probabilities λ_-, λ_0, and λ_+ describe the probabilities that a Kuhn step along the polymer from step $n-1$ to n leads to layer i, from, respectively, layer $i-1$, i and $i+1$ [40]. For chains on a cubic lattice (between flat surfaces), λ_-, λ_0, and λ_+ are 1/6, 4/6, 1/6, respectively, reflecting the fractions of nearest neighbors on the cubic lattice in each of the three layers on which the next Kuhn step might reside. For chains on a spherical lattice (on an isolated spherical particle), the transition probabilities λ_-, λ_0, and λ_+ are functions of radial distances from the particle center, as $(R + h_i - l_k)/(6(R + h_i))$, 4/6, and $(R + h_i + l_k)/(6(R + h_i))$, respectively, where R is the radius of the particle. The differences arise because for sites of equal volume, the numbers of sites are different in different lattice layers. Later we fit our SCFT results for polymers near an isolated particle to results from Brownian dynamics (BD) simulations to obtain the excluded volume of a HEUR monomer.

To describe chains on an isolated particle, we apply non-penetration and reflecting boundaries so that

$$p(h_0, n) = 0 \tag{2.5}$$

and

$$p(h_{L+1}, n) = p(h_L, n) \tag{2.6}$$

We choose L to be large enough that $p(h_{L+1}, n)$ is zero. For chains between two flat surfaces, two non-penetration boundaries are applied so that

$$p(h_0, n) = p(h_{L+1}, n) = 0 \tag{2.7}$$

The Boltzmann weight for a chain segment n to reside at the ith layer is

$$Q(h_i, n) = p(h_i, n)p(h_i, N - n + 1)e^{W(h_i)/kT} \tag{2.8}$$

Because both $p(h_i, n)$ and $p(h_i, N-n+1)$ include the bias for placing segment n at the same lattice layer, the total penalty for monomer n to reside at layer i, calculated using $p(h_i, n)p(h_i, N-n+1)$, is double-counted as $e^{-2W(h_i)/kT}$. We use the exponential term in eqn 2.8 to cancel this double-counting. The single chain partition function Z is therefore the sum of Boltzmann weights for chain conformations to have any monomer located at any lattice layer:

$$Z = \sum_{n=1}^{N} \sum_{i=1}^{L} A(h_i)Q(h_i, n) \tag{2.9}$$

where $A(h_i)$ is the number of sites in the ith lattice layer. On a spherical lattice, $A(h_i) = 4\pi(R + h_i)^2$. On a cubic lattice, $A(h_i)$ is a constant A for all h_i.

The density distribution $\rho(h_i)$ is therefore calculated as:

$$\rho(h_i) = \frac{JN \sum_{n=1}^{N} Q(h_i, n)}{Z} \tag{2.10}$$

where J equals the total number of chains, given as $A(R)\sigma_0$ and $2A\sigma_0$ for chains on an isolated particle and between two flat surfaces, respectively. The value of σ_0 represents the uniform surface density of telechelic chains.

We can self-consistently solve the density distribution of polymers for any given excluded volume v near isolated particles. To obtain the excluded volume v for HEUR polymers, we perform coarse grained BD simulations of telechelic chains near isolated particles. In our BD simulations, the HEUR polymers are purely repulsive beads connected by harmonic springs of rest length l_k and spring constant $400kT/l_k^2$. Monomer beads interact with each other via a Weeks-Chandler-Anderson potential:

$$U_{bb}(r) = \begin{cases} 4\epsilon_{bb}\left[\left(\frac{\sigma_{bb}}{r}\right)^{12} - \left(\frac{\sigma_{bb}}{r}\right)^{6} + \frac{1}{4}\right] & r < 2^{1/6}\sigma_{bb} \\ 0 & r \geq 2^{1/6}\sigma_{bb} \end{cases} \tag{2.11}$$

where $\epsilon_{bb} = 1.0kT$. The interaction range σ_{bb} is set to be $0.4l_k$, which was chosen so that the BD simulations give the correct radius of gyration for PEO in dilute aqueous solutions (Fig. 2.1a). The attractions between the end monomers of the telechelic chains and the colloid surfaces are described using a shifted Lennard-Jones (LJ) potential with a deep attractive well (40 kT). In this way, the end monomers of HEUR polymers are always absorbed on particle surfaces. Details of our BD simulations are included in the section 2.6 Appendix: Brownian Dynamics Simulation Methodology.

By fitting our SCFT-calculated Kuhn monomer distributions of adsorbed loops on an isolated particle to the corresponding results for BD simulations with BD bead size determined from experiments as described above, we can obtain the SCFT excluded volume $v = 0.23l_k^3$ for HEUR polymers. The distribution of polymer segments in the radial direction is governed by the excluded volume interactions. For various surface densities of polymers, the distributions of Kuhn segments from our SCFT calculations with $v = 0.23l_k^3$ agree well with the results from our BD simulations (Fig. 2.1b). For brush-like telechelic chains absorbed on particle surfaces, the mean-field SCFT theory works well, indicating the fluctuations in the polymer density field are negligible. However, for chains in the mushroom-regime, the SCFT model may fail due to the significant fluctuations in the density field of polymer segments.

Because the osmotic pressure of a semidilute polymer solution is $v\bar{\rho}^2kT/2$ ($\bar{\rho}$ is the monomer

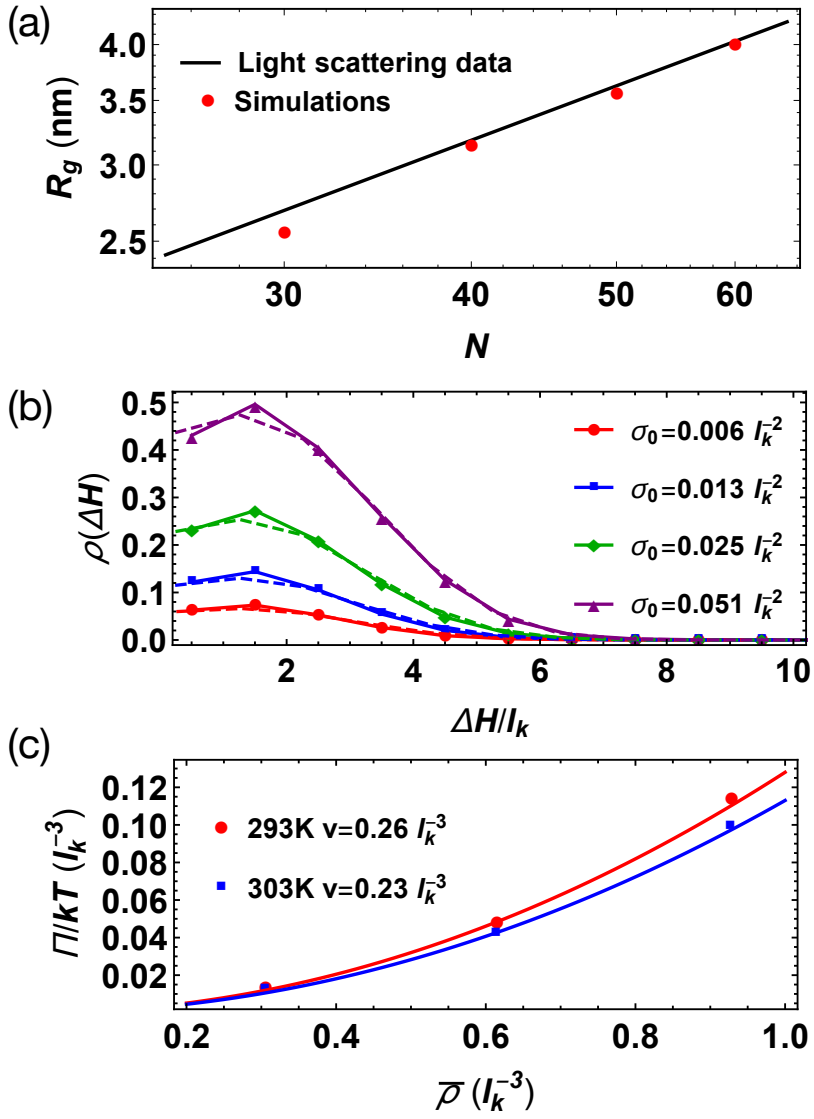

Figure 2.1: (a) Radius of gyration R_g vs. number of Kuhn segments N for PEO in water from coarse grained BD simulations. Light scattering data from Devanand et al.[3] (b) Density distribution of monomers $\rho(\Delta H)$ of polymers with length $N = 40$ near isolated particles of radius $R = 25l_k$. ΔH is radial distance from particle surface. BD simulations (symbols and solid curves). SCFT with $v = 0.23l_k^3$ (dashed curve). (c) Osmotic pressure Π of aqueous PEO solutions vs. Kuhn monomer concentration $\bar{\rho}$ at two temperatures. Experimental data (symbols)[4]. Fit to $\Pi = v\bar{\rho}^2 kT/2$ (curves).

number concentration)[41], the value of v can be also measured experimentally using osmometry. Using the reported osmotic pressures of aqueous PEO solutions with concentrations similar to those in the brush layers near colloidal particles[4], we estimate v to be about $0.23l_k^3$ at room temperature (see Fig. 2.1c), which matches the value we obtained by fitting the polymer distributions from SCFT to BD simulation results.

After justifying our choice of v, we now calculate the free energy of HEUR chains between two flat surfaces, which will be used with the Derjaguin approximation to predict the effective interactions between two colloidal particles. We solve the SCFT equations for $p(h_i, n)$ on a cubic lattice, from which the single chain partition function Z can be obtained. The free energy per chain is:

$$\frac{F(\Delta H)}{kT} = -\ln Z - \frac{l_k}{4\sigma_0}\sum_{i=1}^{L} v\rho(h_i)^2 \tag{2.12}$$

where σ_0 is the surface density of telechelic chains (the total number of chains is $2\sigma_0 A$, where A is the area of a flat surface). The distance between the two flat surfaces in the lattice description is given by $\Delta H = Ll_k$. The last term in eqn 2.12 is used to avoid double counting the pair-wise excluded volume interactions.

We use the Derjaguin approximation and the free energy for chains between two flat surfaces to estimate the effective interactions between two spherical colloidal particles. In the Derjaguin approximation, the curved surfaces of particles are discretized into a series of circular bands (Fig 2.2a). The polymer chains are assumed to be confined between the two facing parallel bands on different particles. The inter-band distance and surface area of the discretized bands increase as we move from the poles to the equators of the particles.

Assuming a uniform surface density σ_0, the net interactions between two particles are obtained by integrating the polymer free energy over all the discretized bands:

$$\frac{f(\Delta H_0)}{kT} = 4\pi R^2 \int_{-1}^{1} \sigma_0 F(\Delta H_0, \mu) d\mu \tag{2.13}$$

in which ΔH_0 is the distance between the poles of two particles (see Fig. 2.2) and $\mu = \cos\theta$. The

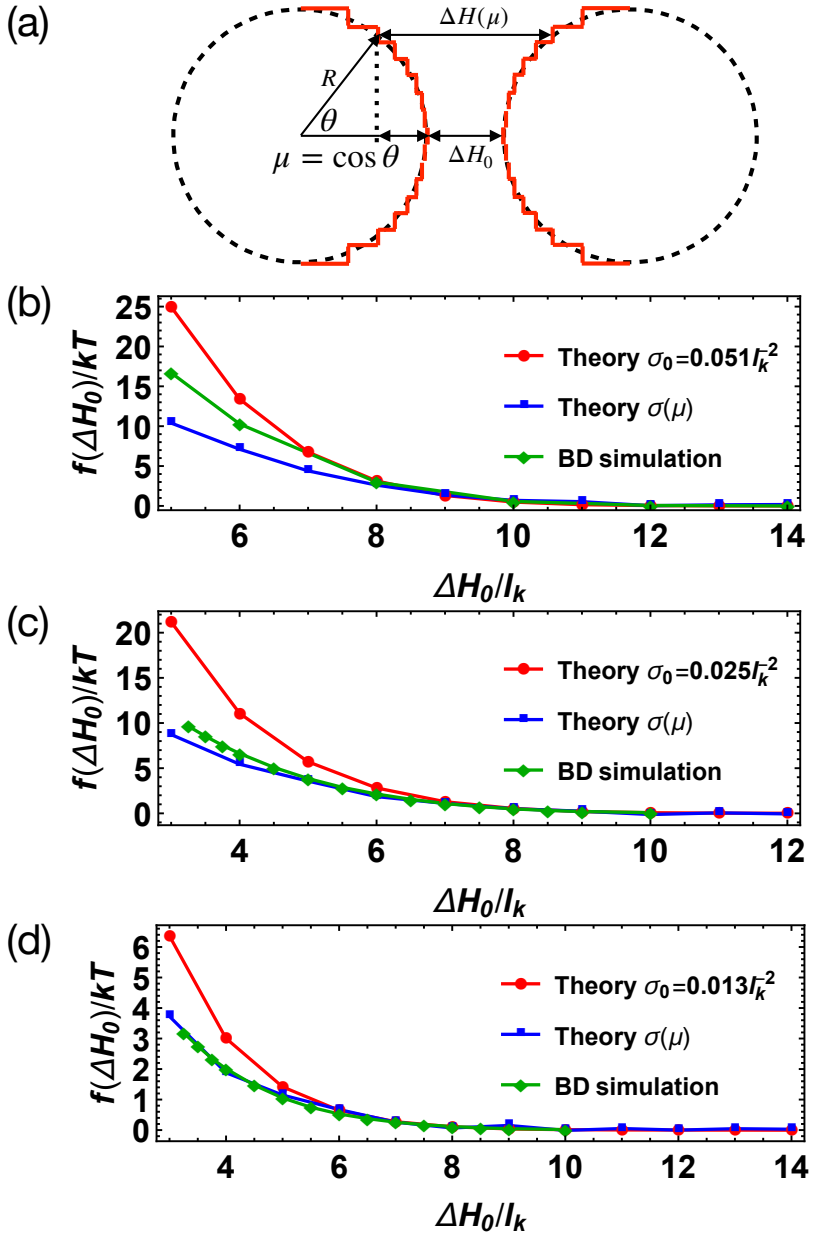

Figure 2.2: (a) Cartoon of two colloidal particles discretized using the Derjaguin approximation. (b-d) Effective repulsion between two colloids of radius $R = 25l_k$, induced by telechelic loops of $N = 40$ Kuhn steps at various average surface densities σ_0. Theory for uniform (red), and non-uniform (blue) density. BD simulations that allow non-uniform surface density (green). The average density imposed for each non-uniform case (both blue and green curves) is the same as in the corresponding uniform distribution.

inter-band distance $\Delta H(\mu)$ is $2R(1-\mu)+\Delta H_0$.

To validate this approach, we compare its prediction of the effective potential generated by telechelic loops to that predicted by BD simulations. The free energy per loop between two flat surfaces can be easily obtained from eqn 2.12 and a modified Boltzmann weight for loops Q_l:

$$Q_l(h_i,n) = \left(p_r(h_i,n)p_r(h_i,N-n+1) + p_l(h_i,n)p_l(h_i,N-n+1)\right) e^{W(h_i)/kT} \tag{2.14}$$

where p_r and p_l are the propagators evolved from the initial Boltzmann factors for placing a monomer at right and left walls.

The effective interactions between two colloids coated by telechelic loops is obtained from BD simulations by varying the inter-particle gap ΔH_0 and measuring the net force on each particle f_n to obtain the effective potential from $f(\Delta H_0) = \int_{\Delta H_0}^{\infty} dH f_n(H)$. The same approach has been used to compute the effective potential of nanoparticles induced by one-end grafted polymer brushes[27]. We only measured the effective interactions induced by loops because obtaining the equilibrium numbers of bridges in BD simulations is impractical due to the excessively long runs required to equilibrate the bridge/loop ratio.

Assuming uniform distributions of polymers on particle surfaces, the predicted repulsive interactions agree with those sampled from BD simulations at large inter-particle distances ΔH_0 (Fig. 2.2b–d). At small ΔH_0, however, our theory with uniform surface density of loops overpredicts the repulsive interactions, especially for small σ_0 as shown by comparing the red and green lines in Fig. 2.2b–d. The weaker repulsion in BD simulations seen in Fig. 2 relative to the theory with uniform polymer distribution likely arises from the depletion in BD simulations of telechelic loops from the compression region at small ΔH_0. By escaping from the compression region where the distance between particle surfaces is smaller than the chain size, polymers in BD simulations reduce the compression penalty at the expense of some decrease in translational entropy.

2.3.2 Theory for non-uniform surface distributions of telechelic chains

We therefore now account for the rearrangement of polymers on the particle surface within our theory by allowing the chain density to vary along the particle surface and by including the resulting translational entropy in the Derjaguin approximation:

$$f(\Delta H_0) = 4\pi R^2 \int_0^1 (\sigma(\mu) F(\sigma(\mu), \Delta H_0, \mu) + \sigma(\mu) \ln \sigma(\mu))\, d\mu \tag{2.15}$$

Here F is the free energy per chain between two flat surfaces, calculated at different surface densities of chains. We can solve the polymer density distribution $\sigma(\mu)$ by minimizing the above free energy with respect to $\sigma(\mu)$ under the constraint: $\int_0^1 \sigma(\mu) d\mu = \sigma_0$, where σ_0 is the uniform surface density attained when ΔH_0 is sufficiently large.

Indeed, this modified Derijaguin approximation predicts that polymers may rearrange on colloidal surfaces to reduce the compression free energy (Figure 2.3a). At small σ_0, our theory accurately predicts the rearrangement of polymers seen in the BD simulations. The polymer distributions in the BD simulations are calculated by projecting the centers of mass of polymer loops onto the particle surfaces. For dense polymer layers, however, our theory overpredicts the depletion at small ΔH_0. Dense telechelic polymer brushes may not be able to escape the compression region since the colloidal surfaces are too crowded for the sticky ends to rearrange. Instead, in the BD simulations those dense chains may tilt to reduce the excluded volume interactions (Fig. 2.3b), which cannot be captured by our theory, which relies on the Derjaguin approximation with its assumption that each chain sees only a flat surface.

By including the non-uniform distributions $\sigma(\mu)$ of polymers on particle surfaces, our theory predicts a weaker effective repulsion induced by loops when ΔH_0 is small (Fig. 2.2b, c, and d) than when a uniform adsorbed density is assumed. The weaker repulsion agrees nicely with BD simulations when the average surface density σ_0 is low. For denser loops, the assumption of a uniform polymer distribution agrees better with the BD simulations (Fig. 2.2d).

We next compute the effective potential induced by non-uniformly distributed polymers in the

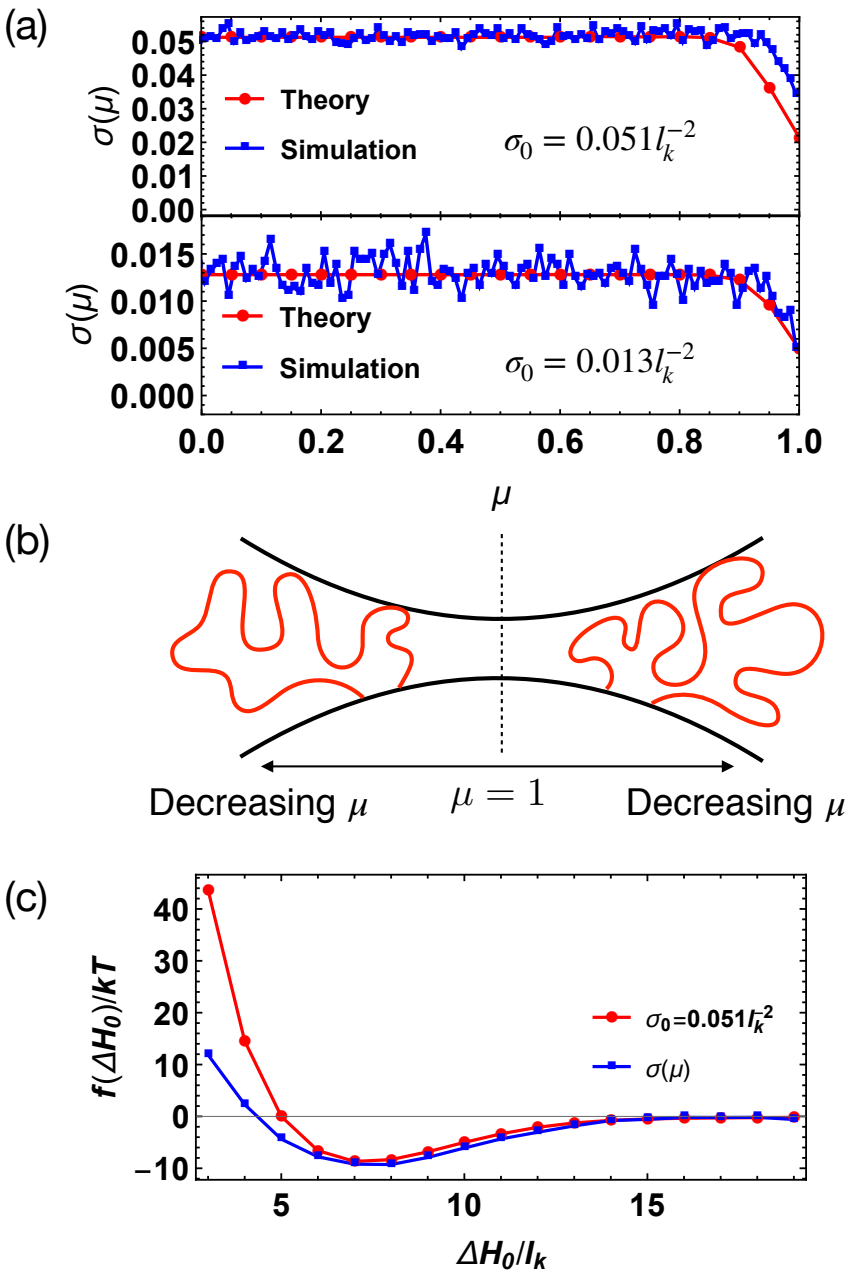

Figure 2.3: (a) Polymer distributions on surface of particle with radius $R = 25l_k$ when $\Delta H_0/l_k = 4$. (b) Cartoon of slightly depleted and tilted telechelic loops. (c) Interactions between particles with radius $R = 25l_k$ induced by polymer loops and bridges using SCFT and the Derjaguin approximation. Uniform (red) and non-uniform (blue) distribution of chains.

presence of the equilibrium number of bridges, which can be calculated using the single-chain partition functions of loops and bridges (details in the next section). As in the case without bridges, the rearrangement of chains reduces the repulsion at small ΔH_0 relative to uniform chain distribution. The bridge-induced attraction, however, is rather similar to that obtained by assuming a uniform polymer distribution (Fig. 2.3c). Since dense telechelic brushes produce relatively uniform chain distributions, we may assume a constant σ_0 to predict their polymer-induced effective interactions.

2.3.3 Theory for systems with non-equilibrium numbers of bridges

Using a uniform distribution of polymers on the particle surface, we can also compute the effective interactions between colloids with any given number of bridges N_b. The bridge-dependent potentials will be useful in future work for predicting the rheological properties of telechelic polymer/colloid mixtures in flows, where the dynamical breakage and formation of bridges and loops are important[10].

We first compute the free energy per chain of telechelic chains between two flat surfaces with fixed bridge and loop fractions:

$$\frac{F(\Delta H, \eta)}{kT} = -(1-\eta)\ln Z_l - \eta \ln Z_b - \frac{l_k}{4\sigma_0}\sum_{i=1}^{L} v\rho(h_i)^2 + \eta\ln\eta + (1-\eta)\ln(1-\eta) \quad (2.16)$$

where η is the fraction of chains that are bridges, and the last two terms give the Shannon entropy, arising from the possible ways of assigning different polymers as loops and bridges. Z_l and Z_b are the single-chain partition function of loops and bridges, obtained using eqn 2.9 and the Boltzmann weights for loops (eqn 2.20) and bridges:

$$Q_b(h_i, n) = 2p_l(h_i, n)p_r(h_i, N-n+1)e^{W(h_i)/kT} \quad (2.17)$$

For a given value of η, we self-consistently solve Q_b, Q_l, and the density field ρ:

$$\rho(h_i, \eta) = \frac{\eta JN \sum_{n=1}^{N} Q_b(h_i, n)}{Z_b} + \frac{(1-\eta) JN \sum_{n=1}^{N} Q_l(h_i, n)}{Z_l} \tag{2.18}$$

Unless η equals the equilibrium bridge fraction, the density distribution ρ should be different from the equilibrium density profile (eqn 2.10). The gap-dependent free energy of a system with equilibrium numbers of loops and bridges (eqn 2.12) is represented as the locus of saddle points on the free energy surface $F(\Delta H, \eta)$ (Fig 2.4a).

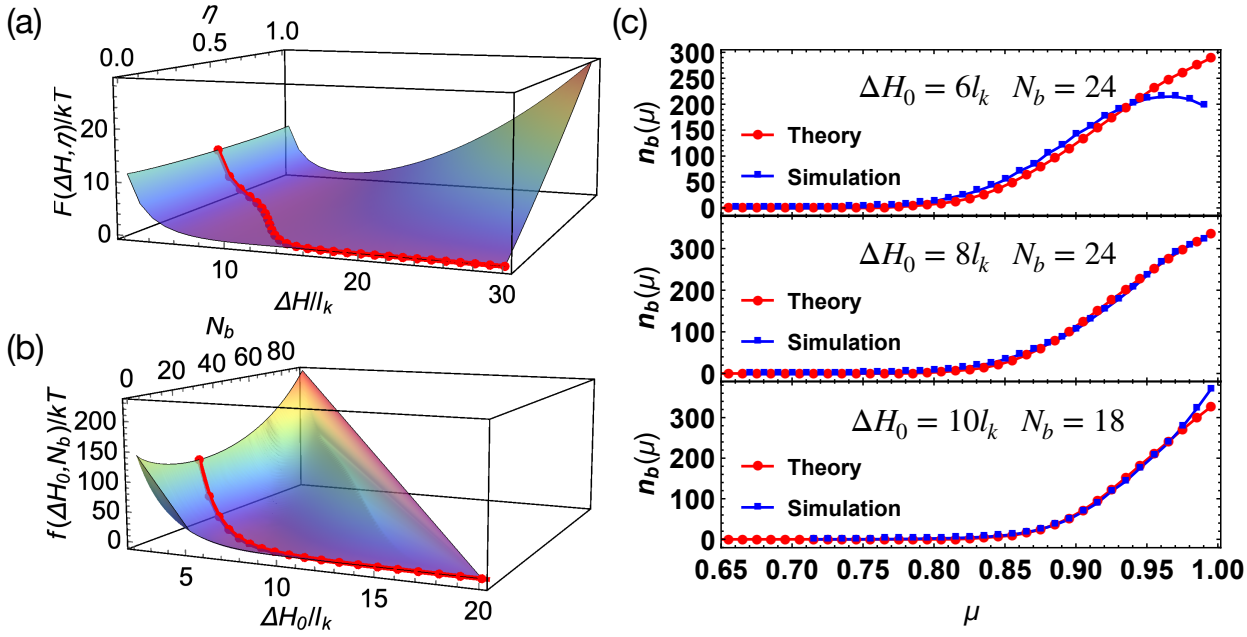

Figure 2.4: (a) Free energy per chain as a function of seperation ΔH and bridge fraction η. (b) Total free energy of two colloids with constrained number of bridges N_b. In both (a) and (b), saddle points are given by red symbols. (c) Distributions of N_b bridges on particles for various separations ΔH_0. Surface density $\sigma_0 = 0.051 l_k^{-2}$, chain length $N = 40$, and particle radius $R = 25 l_k$ for all plots.

We minimize the polymer free energy under the Derjaguin approximation with respect to the distribution of bridge fractions $\eta(\mu)$. The minimization is carried out with the total number of bridges constrained to $N_b = \int_0^1 4\pi R^2 \sigma_0 \eta(\mu) d\mu$. Using the η that minimizes the free energy, we generate a free energy surface in the $N_b - \Delta H_0$ plane for two interacting colloidal particles

(Fig 2.4b).

Our model described above for systems with constrained numbers of bridges is useful for validating our SCFT approach using BD simulations, which are not fast enough to equilibrate the bridge/loop ratio. Thus, in Fig. 4(c), we compare BD to SCFT results for fixed numbers of bridges. The distribution of bridge fractions $\eta(\mu)$, obtained by free energy minimization, allows us to further test the validity of SCFT and the modified Derjaguin approximation by comparing their predictions against BD simulations with a specified fixed number of permanent bridges. In theory, we can obtain the bridge distribution $n_b(\mu)$, which quantifies the bridge density per unit μ, for any imposed fixed total number of bridges $N_b = \int_0^1 n_b(\mu)d\mu$ and inter-particle distance ΔH_0. We can also obtain the bridge distribution $n_b(\mu)$ from BD simulations which shows, as expected, that the bridges tend to distribute near the narrowest gap $\mu = 1$ (Fig. 2.4c). A discrepancy between theory and simulations can be observed at small inter-particle distance ΔH_0 (Fig. 2.4c- top). The reduced surface density of polymers in the BD simulations near $\mu = 1$ (see Fig. 2.3a) may lead to the smaller n_b than that predicted by our theory. Nonetheless, our predicted bridge distributions agree reasonably well with those from the BD simulations.

In our theory and BD simulations, the telechelic polymers only form loops and bridges. In reality, since the attraction between the hydrophobic ends of polymers and colloidal surfaces is finite, these telechelic chains may form dangling and even free chains (polymers that are desorbed from colloidal surfaces) when the surface absorption density σ_0 is sufficiently high. For telechelic polymers such as HEUR in water-borne coatings, however, typical attractions between chain ends and colloidal surfaces are about 10 kT[42]. The rather large attraction prevents the formation of dangling and free chains.

To demonstrate that the dangling and free chains are negligible when the attraction between chain ends and colloidal surfaces is large, we estimate the fractions of dangling and free chains

near isolated particles using SCFT by modifying the initial propagator (eqn 2.2):

$$\begin{aligned} p_s(h_i, 1) &= e^{-(W(h_i)-E)/kT}\delta_{i,1} \\ p_m(h_i, 1) &= e^{-W(h_i)/kT}\Theta(i-1) \end{aligned} \tag{2.19}$$

where p_s and p_m are the conditional Boltzmann weights for placing a chain end at the colloidal surface and in the solution, respectively, and E is the strength of attraction between particle surfaces and chain ends. Θ and δ are the Heaviside theta and Kronecker delta functions. The attraction E enhances the probability for a chain end to reside at the particle surface. When E is sufficiently large, p_s is much greater than p_m. Using the modified initial propagator, we self-consistently solve the density field and compute the fractions of loops (f_l), dangling (f_{dg}) and free chains (f_f) as:

$$\begin{aligned} f_l &= \frac{p_s(h_1, 1)p_s(h_1, N)e^{(W(h_1)-E)/kT}}{Q_0} \\ f_{dg} &= \frac{p_s(h_1, 1)p_m(h_1, N)e^{(W(h_1)-E)/kT}}{Q_0} \\ f_f &= \frac{\sum_{i=2}^{L} p_m(h_i, 1)p_m(h_i, N)e^{W(h_i)/kT}}{Q_0} \end{aligned} \tag{2.20}$$

where Q_0 is a normalization factor, and $p_s(h_i, N)$ and $p_m(h_i, N)$ are the conditional Boltzmann weights for a chain end to locate at h_i after N steps, given that the initial conditions $p_s(h_i, 1)$ and $p_m(h_i, 1)$ are different. When the attraction strength E is greater than 10 kT, the fractions of dangling and free chains are negligible even for rather large surface densities of absorbed chains (Fig. 2.5). For interacting particles, we expect that the strong attractions between chain ends and the colloidal surfaces promote the formation of bridges, instead of dangling chains. As a consequence, our current model is valid for telechelic chains with strong attractive ends. For polymers with weak attractive ends, the formation of dangling and free chains can be easily included by modifying our model.

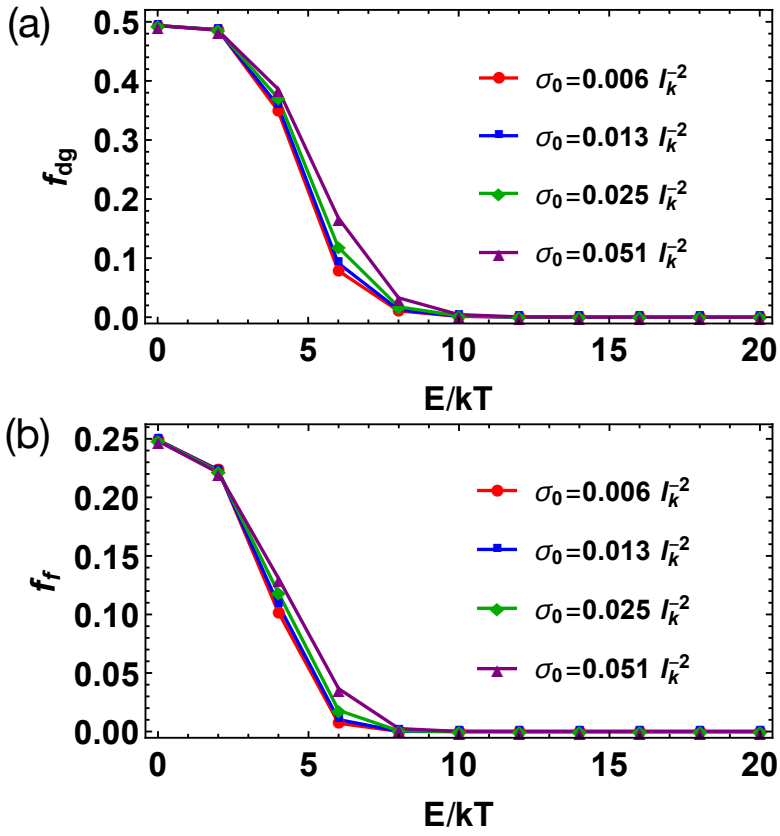

Figure 2.5: Fractions of (a) dangling and (b) free chains on isolated particles vs. attraction strength E between chain ends and colloidal surfaces. Chain length $N = 40$ and particle radius $R = 25l_k$.

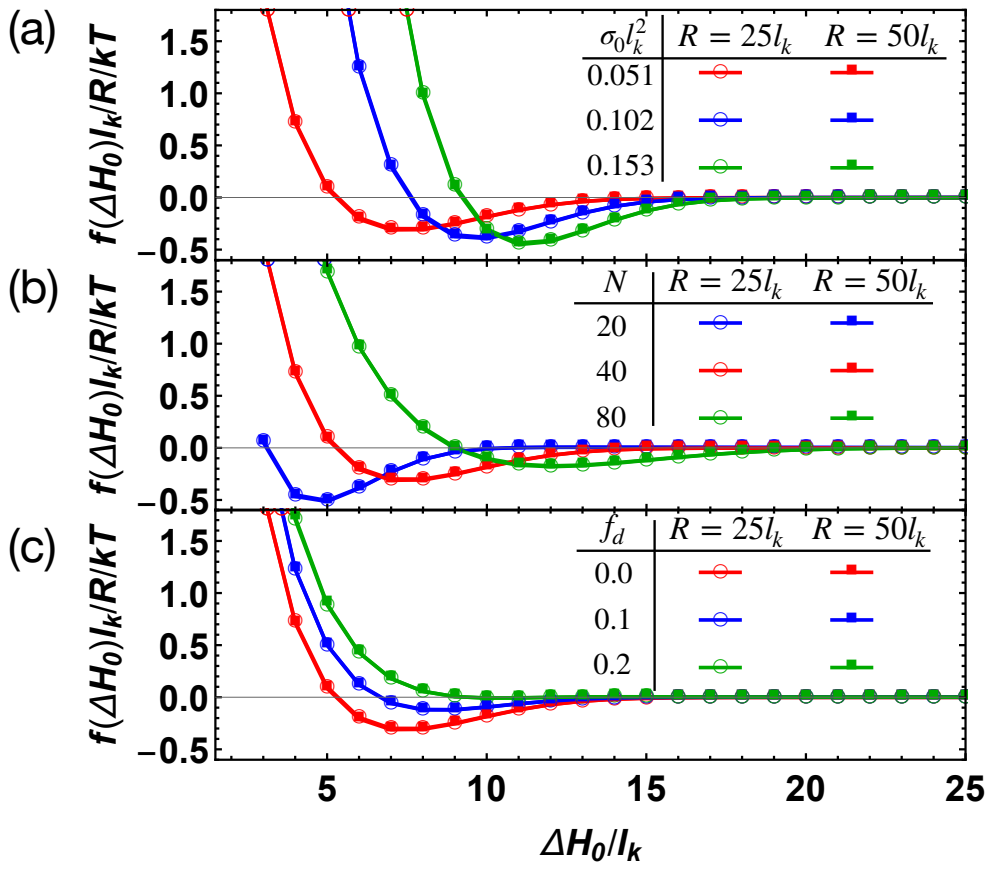

Figure 2.6: Effective interactions induced by telechelic polymers: (a) for chain length of $N = 40$ at different surface densities σ_0 on particles of different sizes R, (b) for chains of various lengths N on particles of different sizes R for surface density $\sigma_0 = 2l_k^{-2}N^{-1}$, (c) for chains of $N = 40$ with various fractions f_d of defective dangling chains (one sticker end per chain) for surface density $\sigma_0 = 0.051l_k^{-2}$.

2.4 Results and Discussions

Having validated our model, we now compute the effective interactions between two colloidal particles that are coated by brush-like telechelic polymers with various surface densities σ_0, particle radii R, and lengths N. Here we assume that the surface density is sufficiently high that polymer distributions on particle surfaces are uniform. Because smaller curvature can enhance the contact areas for polymers on different particles, the effective potential increases linearly with particle radius R (Fig. 2.6).

For polymers with a given length N, the strength and range of induced attraction increases with

increasing surface density σ_0 (Fig. 2.6a). The enhanced attraction results from the extra bridges formed in denser polymer layers. Because higher surface densities lead to more stretched chain conformations and promote the formation of bridges at larger ΔH_0, the range of attraction also increases with increasing σ_0.

At a fixed ratio of total polymer size to particle surface area ($\sigma_0 l_k^2 N$), increasing polymer length results in longer ranged but weaker attractions between the colloidal particles (Fig 2.6b). Although longer chains can form longer bridges at larger ΔH_0, the total number of bridges decreases with decreasing σ_0, which leads to weaker attractions.

We also predict that small amounts of single-end functionalized chains can significantly reduce the attraction between particles. In our lattice SCFT calculations, we introduce an initial Boltzmann factor for the defective ends as $p_d(h_i, 1) = e^{-W(h_i)/kT}$, which can be non-zero in lattice layers that are not adjacent to particle surfaces. By evolving $p_d(h_i, n)$ from the initial state, we can compute the Boltzmann weight for dangling chains as:

$$Q_d(h_i, n) = (p_l(h_i, n) + p_r(h_i, n))p_d(h_i, N - n + 1)e^{W(h_i)/kT} \tag{2.21}$$

where p_l and p_r are obtained from monomers that are initially placed next to the left and right surfaces, respectively. By summing Q_d over all lattice layers and monomer indices, we obtain the single chain partition function for dangling polymers Z_d. The free energy of telechelic polymers with dangling chains of fraction f_d between two flat surfaces is simply:

$$\frac{F(\Delta H, f_d)}{kT} = -(1 - f_d)\ln Z - f_d \ln Z_d - \frac{l_k}{4\sigma_0}\sum_{i=1}^{L} v\rho(h_i)^2 + f_d \ln f_d + (1 - f_d)\ln(1 - f_d) \tag{2.22}$$

in which Z is the single chain partition function of perfect telechelic polymers that can form loops and bridges, obtained using eqn 2.9.

By introducing about 20% defective chains, the interactions between particles, induced by telechelic chains of length $N = 40$, is reduced to nearly zero (Fig 2.6c). These dangling chains provide long ranged repulsion between particles and compensate the net attraction induced by

telechelic bridges.

We expect small fractions of defective telechelic chains can be useful for stabilizing colloidal suspensions. To show this, we map our attractive effective interactions to the Baxter temperature τ, which quantifies the phase behaviors of hard spheres with short range attractions (adhesive hard spheres)[43, 44]. Lu and coworkers have demonstrated that various short-ranged attractive interactions, such as square-well, Lennard-Jones, and Asakura-Oosawa potentials, can be all mapped to τ for predicting phase separation in colloidal suspensions[45].

The value of τ can be obtained by equating the reduced second virial coefficient B_2^* of the effective inter-colloid potential $f(\Delta H_0)$ to that of an adhesive hard sphere:

$$B_2^* = 1 - \frac{1}{4\tau} = \frac{3}{8R_*^3}\int_{2R}^{\infty}(1 - e^{-f(r-2R)/kT})r^2 dr \tag{2.23}$$

in which $R_* = R + \Delta H_0^*/2$ is the overall radius of the polymer coated particle[45]. ΔH_0^* is the value of ΔH_0 at which the potential is zero, and beyond which the effective potential f becomes attractive. Using τ, the phase behaviors of colloids coated by different telechelic chains can be estimated using the phase diagram of adhesive hard spheres[5, 46, 47] (Fig. 2.7a).

We test the phase behaviors of colloidal suspensions by performing Monte Carlo (MC) simulations in the NVT ensemble for 500 colloids of size $R = 25l_k$ starting from random initial configurations using the Metropolis method and the effective potentials corresponding to telechelic polymers of length $N = 40$ and surface densities $\sigma_0 = 0.051l_k^{-2}$ including the effect of a gap-dependent equilibrium number of bridging chains, which assumes that the number of bridges instantaneously adjusts as the gap between particles changes. Different fractions of dangling chains f_d are used to control the strengths of the inter-colloid interactions. When a sufficient fraction of dangling chains is introduced ($f_d > 0.10$), the colloids remain dispersed with a gas-like pair correlation function $g(r)$, whose intensity decays quickly to unity after a single peak (Fig. 2.7c). When f_d is small, however, the inter-particle attractions are strong and the colloidal suspension can undergo a gas-liquid phase separation, indicated by the formation of dense liquid domains (Fig. 2.7b

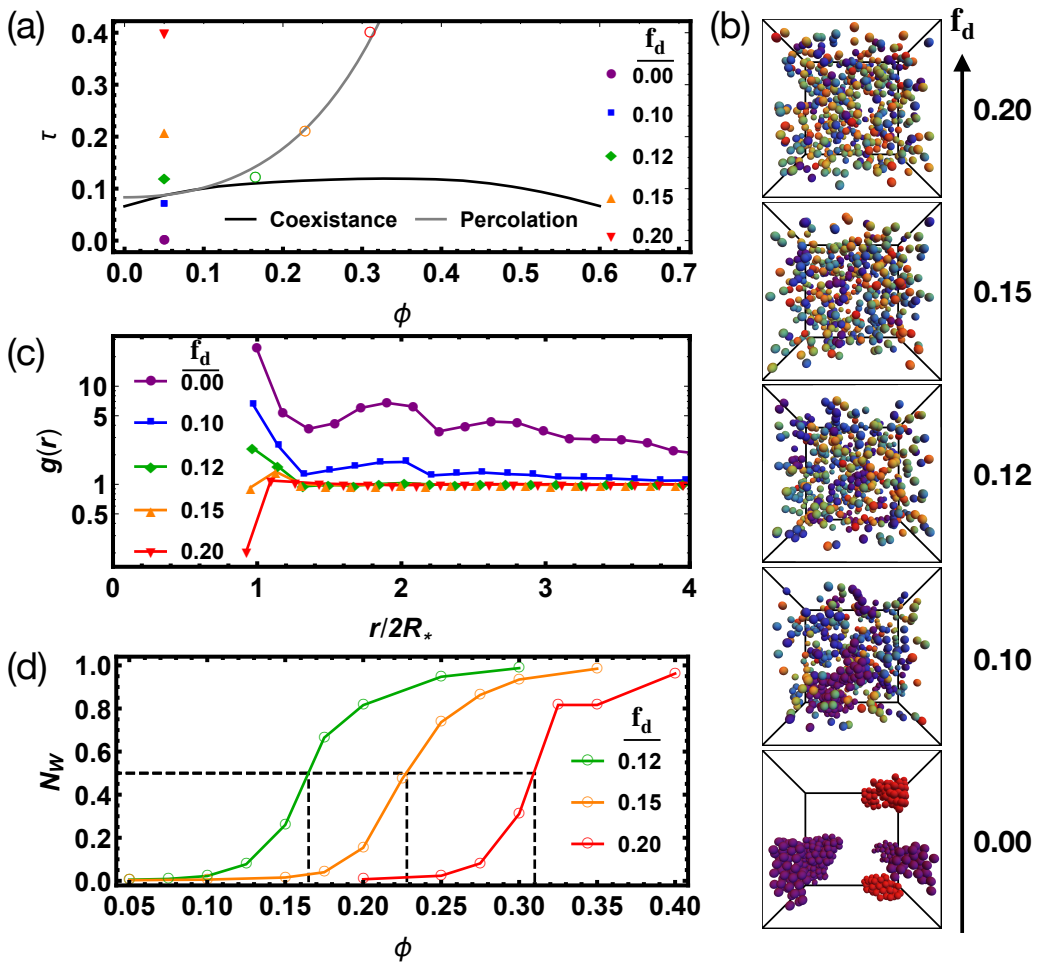

Figure 2.7: (a) Phase diagram for colloids coated by telechelic chains of $N = 40$ and surface densities $\sigma_0 = 0.051 l_k^{-2}$ at various fractions of defects f_d. Volume fraction of the colloids is given by $\phi = 4\pi\rho R_*^3/3$. Percus-Yevick coexistence (black curve) and percolation (gray curve) boundaries are from Chiew and Glandt [5]. Critical volume factions for percolation computed from Monte Carlo simulation results in (d) are given by open circles. (b) Snapshots of simulations at $\phi = 0.05$ with particles colored by cluster index. (c) Pair-correlation function $g(r)$ of colloids in MC simulations. (d) Second moment N_w of cluster size distribution. System starts to percolate when $N_w > 0.5$ (dashed lines), giving values of phi plotted in (a).

near the bottom) and a liquid-like $g(r)$ with multiple short-range peaks. The phase behaviors in simulations for colloidal suspensions with 5% colloids by volume show a transition to a phase separated structure (Fig. 6b) at a fraction of dangling chains between 10% and 12%, which agrees with the transition predicted by the Baxter phase diagram for adhesive hard spheres[5] with Baxter temperature obtained from the potential calculated for these systems, as shown in Fig. 6a.

Mapping the polymer-induced interactions to Baxter temperature τ is also useful for estimating the percolation behaviors of colloids. We show that the percolation transition of colloids can be rather accurately captured by the prediction for adhesive hard sphere using the Percus-Yevick (PY) approximation[5]. To show this, we estimate the critical volume fraction for percolation in MC simulations by first computing the cluster size distribution:

$$p(n_c) = \langle \frac{N_{n_c}}{N_{tot}} \rangle \tag{2.24}$$

in which N_{n_c} is the number of clusters that are composed of n_c colloids and N_{tot} is the total number of particles in the simulations. We group colloids that share common neighbors into a cluster. Two particles are considered to be neighbors when the inter-particle distance is smaller than the range of the effective attraction (about 15 l_k). The percolation transition is characterized using the second moment of $p(n_c)$:

$$N_w = \frac{1}{N_{tot}} \langle \sum_{n_c} n_c^2 p(n_c) \rangle \tag{2.25}$$

When N_w is greater than 0.5, we consider the system to be percolated[48] (Fig. 2.7d). The critical volume factions for percolation in our MC simulations agree well with the PY percolation boundary (Fig. 2.7a).

2.5 Conclusion

We have applied an analytical approach, combining self-consistent field theory (SCFT) and the Derjaguin approximation to predict the effective interactions between colloids induced by

telechelic polymers in solutions. The chain ends of telechelic polymers can physically absorb onto the particle surfaces, forming loops and bridges, which in turn induce effective interactions between colloidal particles. We validate our theoretical approach by comparison to direct Brownian dynamics simulations.

When two spheres are pressed together, our theory predicts that telechelic polymers may rearrange and distribute non-uniformly on the colloidal surfaces. In this way, polymers reduce their excluded volume interactions at the cost of a reduction in translational entropy. Our predicted non-uniform distributions of polymers agree with results from BD simulations when polymer surface density is relatively low but still in the brush regime, so that the SCFT is still valid. However, such rearrangement of polymers become less likely when the surface density increases, as observed in our BD simulations. Dense brushes of telechelic chains distribute rather uniformly on particle surfaces even under rather strong compression.

We expect our overall approach to be useful for designing formulations for applications such as waterborne coatings, in which telechelic rheology modifier is adsorbed on latex particles[25]. For example, the bridge-dependent inter-colloid potential, calculated using our method, is necessary for constructing hybrid coarse grained simulation methods for predicting the viscoelastic response of telechelic polymer/colloid mixtures in flows[10]. Our approach also enables efficient estimation of the stability of colloidal suspensions in which the molecular structures and surface densities of associating polymers vary.

2.6 Appendix: Brownian Dynamics Simulation Methodology

All simulations were performed using HOOMD-blue, a particle simulation software package optimized for GPU performance [49, 50, 51]. HEUR polymers are represented as series of purely repulsive beads connected by stiff harmonic springs, with each spring representing one Kuhn step.

The harmonic spring between adjacent beads is defined as

$$U_{bond}(r) = \frac{1}{2}k(r - r_0)^2 \tag{2.26}$$

where $k = 400kT/l_k^2$ and $r_0 = 1.0l_k$. The value of l_k is 1.1 nm in our work, representing the length of one Kuhn step of PEO, the interior segments of HEUR.

The repulsive interactions between polymer beads are modeled using a Weeks-Chandler-Anderson potential,

$$U_{bb}(r) = \begin{cases} 4\varepsilon_{bb}\left[\left(\frac{\sigma_{bb}}{r}\right)^{12} - \left(\frac{\sigma_{bb}}{r}\right)^{6} + \frac{1}{4}\right] & r < 2^{1/6}\sigma_{bb} \\ 0 & r \geq 2^{1/6}\sigma_{bb} \end{cases} \tag{2.27}$$

where $\varepsilon_{bb} = 1.0kT$ and $\sigma_{bb} = 0.4l_k$.

We choose the value of σ_{bb} so that our model generates the correct radius of gyration for PEO in dilute aqueous solutions as shown by light scattering results[3] as shown in Fig. 2.8.

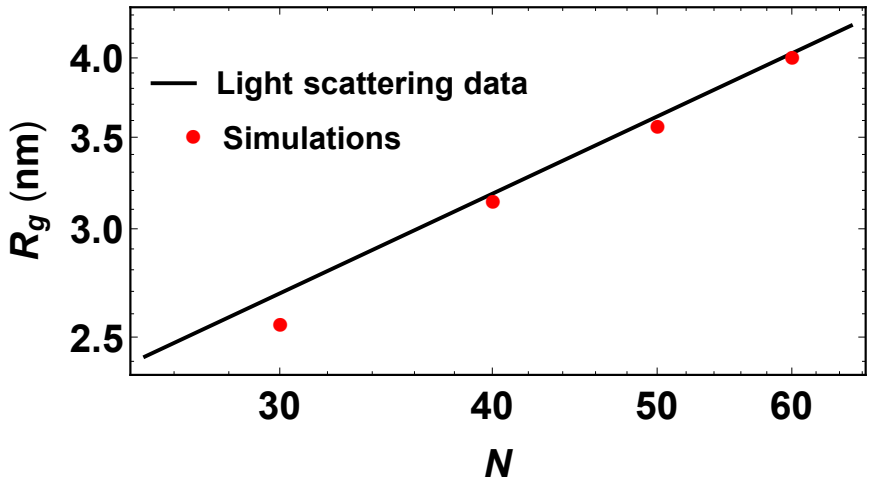

Figure 2.8: Radius of gyration R_g vs. number of Kuhn segments N for PEO in water. Experimental data from Devanand et al.[3]

We model the attraction of the hydrophobic chain ends of telechelic HEUR polymers to the

hydrophobic colloid surfaces using a shifted Lennard-Jones potential,

$$U_{sc}(r) = \begin{cases} 4\varepsilon_{sc}\left[\left(\frac{\sigma_{sc}}{r-\Delta_{sc}}\right)^{12} - \left(\frac{\sigma_{sc}}{r-\Delta_{sc}}\right)^{6}\right] & r < 3.0 + \Delta_{sc} \\ 0 & r \geq 3.0 + \Delta_{sc} \end{cases} \tag{2.28}$$

where $\Delta_{sc} = \left[\frac{D_{colloid}+D_{sticker}}{2} - 1\right]l_k$, $D_{colloid} = 50.0l_k$, $D_{sticker} = 1.0l_k$, and $\sigma_{sc} = 0.4l_k$. The strong interaction parameter $\varepsilon_{sc} = 40$ kT prevents chain ends from detaching while preserving translational freedom on the colloid surface. The interior beads of the polymer chain are purely repulsive with respect the colloid surface, and are represented by a shifted Weeks-Chandler-Anderson potential

$$U_{bc}(r) = \begin{cases} 4\varepsilon_{bc}\left[\left(\frac{\sigma_{bc}}{r-\Delta_{bc}}\right)^{12} - \left(\frac{\sigma_{bc}}{r-\Delta_{bc}}\right)^{6} + \frac{1}{4}\right] & r < 2^{1/6}\sigma_{bc} + \Delta_{bc} \\ 0 & r \geq 2^{1/6}\sigma_{bc} + \Delta_{bc} \end{cases} \tag{2.29}$$

where $\Delta_{bc} = \left[\frac{D_{colloid}+D_{bead}}{2} - 1\right]l_k$, $D_{colloid} = 50.0l_k$, $D_{bead} = 1.0l_k$, $\varepsilon_{bc} = 1.0$kT, and $\sigma = 0.4l_k$.

At each time step, the following Langevin equation for the particle velocities is integrated

$$m\frac{d\vec{v}}{dt} = \vec{F_C} - \gamma \cdot \vec{v} + \vec{F_R} \tag{2.30}$$

in which $\vec{F_C}$ is the conservative force from all potentials, $\vec{v}$ is the particle's velocity, and $\vec{F_R}$ is the random force. The drag coefficient γ is taken to be $1.0\frac{[m]}{[t]}$ for polymer beads and $100.0\frac{[m]}{[t]}$ for colloids, where $[m]$ is set to unity, thereby defining the unit of mass in our simulations and $[t] = \sqrt{[m]l_k^2/kT}$ is similarly set to unity. Hereafter, all units of length are assumed to be l_k and energies are in units of kT. Time steps are made small enough that results are insensitive to the exact value.

We prepare initial configurations for all simulations by generating two colloids with the given number of polymer loops randomly distributed on their surfaces using Packmol, an initial configuration generator [52]. The energy of the polymers is minimized for 10^4 time steps to avoid any overlaps or non-physical behavior, and then the polymer chains are equilibrated for 10^5 time steps.

To generate density distributions, $\rho(\Delta H)$, for non-interacting colloids, the colloids remain fixed at a distance $\Delta H_0 \gg 2 * Rg$, where ΔH is the distance from the surface of a particle in the radial direction, ΔH_0 is the closest surface-to-surface distance between two particles and R_g is the radius of gyration of a telechelic chain. Polymer chains are allowed to relax while data is sampled for 5×10^6 time steps.

For simulations where a specific interparticle gap is of interest, such as for polymer distributions at small ΔH_0 or for calculations of inter-particle force, we follow a protocol similar to that described by Verso et al. [26, 27, 53] First, we initialize two colloids at a distance large enough that the particles and chains adsorbed on them do not interact, and equilibrate the polymers on both colloids for 10,000 time steps. We then shift the particles closer by a distance $\delta r = 0.05 l_k$ and re-equilibrate the system, repeating this shift and equilibration procedure until the target interparticle gap is reached. We then run the simulations for 10^7 time steps, recording system information at intervals of 100 time steps. At each interparticle gap ΔH_0 of interest, the net force on each colloid is calculated by summing over all forces on the colloid and all polymers adsorbed to that colloid. The effective interaction $f(\Delta H_0)$ between particles can then be calculated by integrating over the net forces, $f_n(\Delta H_0)$, calculated at all interparticle gaps: $f(\Delta H_0) = \int_{\Delta H_0}^{\infty} f_n(H_0) dH_0$.

Acknowledgements

We acknowledge the funding from National Science Foundation (Grant No. CDS&E–1602183) and the computational resources provided by Extreme Science and Engineering Discovery Environment (XSEDE). We also thank Valeriy Ginzburg for helpful discussions.

CHAPTER 3

Bridging Dynamics of Telechelic Polymers Between Hydrophobic Surfaces

3.1 Abstract

We use Brownian dynamics (BD) simulations resolved at the level of a Kuhn step to calculate the rate at which a telechelic polymer with surface-adhering endcaps transitions from a bridge between two flat surfaces to a loop on a single surface. We then use self-consistent field theory (SCFT) to obtain the equilibrium ratio of bridges to loops and apply the principle of detailed balance to obtain the slower loop-to-bridge times from the faster bridge-to-loop times. The bridge-to-loop transition time has two scaling regimes: one where it is approximately equal to the time for a lone hydrophobic particle to desorb from a surface, and the other where it is dominated by the retraction time of the polymer; approximate formulas for both times are given. The results are important for interpretating the dynamics and rheology of latex coating fluids, in which colloidal particles are dynamically bridged by telechelic rheology-modifying polymers.

3.2 Introduction

Telechelic rheology-modifying polymers have widespread applications in waterborne coatings (i.e. latex paints), pharmaceuticals, and personal care products [13, 12]. The addition of rheology-modifying polymers to these formulations allows for tuning of their rheological profiles, such as

controlling the zero-shear viscosity or increasing the controlling the high-shear viscosity for ease of application of a coating [13]. A common class of rheology-modifying polymers are Hydrophobically Modified Ethoxylated Urethanes, or HEURs, which consist of a hydrophilic polyethylene oxide (PEO) backbone and hydrophobic groups along the PEO backbone and/or end-capping the polymers.

The behavior of solutions of telechelic HEURs, with a purely hydrophilic backbone and two hydrophobic endcaps, in water (without colloids) is a rich area of study. The HEURs form flower-like micelles, in which the hydrophobic endcaps are aggregated into micelles bridged by some of the HEURs. Because the strength of the hydrophobic interactions is not much greater than the thermal energy, these bridges can easily break and reform. At sufficiently high concentrations, dynamic networks of flower-like micelles form [14]. Tanaka and Edwards determined that the characteristic relaxation time, τ, of a HEUR network is exponentially related to the strength of the HEURs' hydrophobic endcaps $\Delta G : \tau \propto \exp[\Delta G/k_B T]$ [54]. Using Monte Carlo simulations of a transient network of flower-like micelles and dynamic bridges, Annable et al. were able to semi-quantitively capture the dynamics and linear viscoelasticity of experimental HEUR solutions, confirming the formation of isolated flower-like micelles at low concentration and micelles linked into a network by bridges at higher concentrations [15]. Tripathi et al. then presented a constitutive model for the dynamic behavior of these telechelic polymer networks, approximating bridge-to-loop and loop-to-bridge transition rates that quantitatively capture the shear-dependent behavior of HEUR solutions [55]. These transition rates have since been used as approximate transition rates in the Population balance - Brownian dynamics model of polymer-colloid mixtures by Hajizadeh and coworkers [10].

While the rheological behavior of solutions of HEURs is often relatively simple, in that it is often dominated by a single relaxation time, the addition of colloidal particles to HEUR solutions results in significantly more complex rheology [56, 57]. As in solutions of HEURs, the hydrophobic end-groups aggregate, not into micelles, but instead onto to the colloids' surfaces, forming coronas of hydrophobic loops coating the colloids. Just as with pure HEUR solutions, bridges

can form between colloids, resulting in a transient network of colloids interconnected by HEURs. However, experimental linear rheological data show much more complex behavior than with simple HEUR solutions [56, 57]. A partial explanation is suggested by recent Brownian dynamics simulations that represent the HEUR's by dumbbells whose beads stick to much larger colloids. These simulations suggest that there are at least four distinct relaxation modes governing the behavior of these solutions, including the characteristic times describing the transition of a telechelic polymer between bridge and loop configurations [22].

A prior study by Rezvantalab and Larson investigated the loop-to-bridge transition process for bead-spring chains using forward flux sampling that neglected polymer excluded volume effects both within an individual polymer and between polymers, essentially limiting the work to dilute polymer adsorption. Their work found that the loop-to-bridge time depended on the level of resolution of the bead-spring molecule, suggesting that accurate results could only be attained by resolution at the level of a Kuhn step. Rezvantalab and Larson also assumed that the bridge-to-loop rate is a constant, independent of the stretch of the molecule [11]. Thus, a comprehensive, accurate, description of both bridge-to-loop and loop-to-bridge transition times of telechelic polymers between surfaces is still lacking. Such a description is needed to understand the dynamics of polymer-colloid interactions, as well as to inform coarse-grained modeling that might lead to an accurate theory of the rheology of suspensions of colloidal and telechelic polymers [10].

In this work, we use Brownian dynamics simulations to model HEUR polymers as bead-spring chains resolved at the level of a Kuhn step with excluded volume and study their transition times between two hydrophobic colloids approximated as flat surfaces. The study of transitions of chains between flat surfaces is a needed first step to determining transitions between curved spherical colloidal surfaces, which can be inferred from the flat-surface results by using the well-known Derjaguin approximation. BD simulations can be used to compute bridge-to-loop and loop-to-bridge transition times for systems with short chains, but are too computationally expensive for experimental chain lengths. Therefore, we show that the self-consistent field theory (SCFT) presented by Zhang et al. reasonably predicts the equilibrium number of bridges and loops for a given sys-

tem [58]. Using the detailed-balance principle, we then use the equilibrium SCFT information to obtain the ratio of the bridge-to-loop to the loop-to-bridge transition times, so that we need only to compute the faster bridge-to-loop transition time directly with BD simulations to obtain the full picture of bridging dynamics.

We compute bridge-to-loop transition times for varying chain lengths, and show that the time for a bridge's hydrophobe to desorb from a wall converges to the desorption time of a hydrophobic particle (not connected to a spring) for small normalized gaps. However, the total bridge-to-loop transition time is usually much longer than the hydrophobe desorption time, especially for long, experimentally relevant, 200-Kuhn-step chains. At small gaps we propose that this longer transition time is due to multiple re-entries into the potential well, and at large gap, and lower hydrophobe adsorption strength, the required time for the polymer to retract once the hydrophobe desorbs begins to dominate the bridge-to-loop time. This contradicts the assumption, commonly made for solutions of HEURs without colloids, that the bridge-to-loop transition time can be simply approximated as the desorption time of a lone hydrophobe, with no influence of the connecting polymer chain.

3.3 Simulation Model

HEURs (hydrophobically modified ethoxylated urethanes) are telechelic polymers that consist of PEO backbones with typical molecular weights around 24-35 kg/mol and hydrophobic endcaps that adsorb to the surface of colloids with an attractive strength of 10-20 k_BT [57, 18]. Since, for PEO, the number of Kuhn steps is related to the molar mass through the relationship $M_W \approx N_K \cdot 137 g/mol$, the above range of molecular weights correspond to chains that are 175-255 Kuhn steps in length [59] The simulations in this study use reduced units that can be mapped to real units. Thus, all energies are in units of k_BT where k_B is Boltzmann's constant and T is 298 K. Lengths are in units of b_K, which represents one Kuhn step of a PEO polymer, or 1.1 nm, and the water solvent viscosity is held constant at $\eta_s = 8.90 \times 10^(-4) Pa \cdot s$ at $298K$ [59] All other reduced

units can then be derived from these definitions of k_BT,η_s, and b_k. In particular, the reduced time unit, $[t]$, is calculated to be $[t] = (\eta_s b_K^3)/k_BT = 0.288ns$.

All simulations were performed using HOOMD-blue, a particle simulation software package optimized for GPU performance [60]. We represent each HEUR as a chain of purely repulsive beads connected by stiff harmonic springs with zero force at a finite extension (i.e., a "Fraenkel spring"), with each spring representing one Kuhn step, and the hydrophobic end group (or "sticker") represented by a single bead whose binding strength to the colloid can be varied. The harmonic spring potential between adjacent beads is

$$U_{bond}(r) = \frac{1}{2}k(r - r_0)^2 \tag{3.1}$$

where $k = 400k_BT/b_k^2$, $r_0 = 1.0b_K$, and r is the distance between the particle centers. The purely repulsive polymer bead-bead interactions (including the "sticker" bead) are modeled using a Weeks-Chandler-Anderson (WCA) potential,

$$U_{bb}(r) = \begin{cases} 4\varepsilon_{bb}\left[\left(\frac{\sigma_{bb}}{r}\right)^{12} - \left(\frac{\sigma_{bb}}{r}\right)^{6} + \frac{1}{4}\right] & r < 2^{1/6}\sigma_{bb} \\ 0 & r \geq 2^{1/6}\sigma_{bb} \end{cases} \tag{3.2}$$

where $\varepsilon_{bb} = 1.0k_BT$ and $\sigma_{bb} = 0.4b_K$ and r is the center-to-center distance between beads. In our earlier work, this value of σ_{bb} was chosen to generate the correct radius of gyration for PEO in dilute aqueous solutions as shown by light scattering results [58, 3].

We model the attraction of the hydrophobic sticker bead to the hydrophobic flat surfaces by defining a shifted-Lennard-Jones potential in terms of the distance from the wall to the particle center, Δx,

$$U_{ws}(\Delta x) = \begin{cases} 4\varepsilon_{ws}\left[\left(\frac{\sigma_{ws}}{\Delta x}\right)^{12} - \left(\frac{\sigma_{ws}}{\Delta x}\right)^{6}\right] & \Delta x < 2.5\sigma_{ws} \\ 0 & \Delta x \geq 2.5\sigma_{ws} \end{cases} \tag{3.3}$$

where $\sigma_{ws} = 1.0b_K$, and ε_{ws} depends on the length of the experimental hydrophobe and ranges from 4-12 k_BT in this study. We choose the cutoff distance to be where the potential goes ap-

proximately to zero, $\Delta x = 2.5\sigma_{ws}$, and the potential is shifted slightly vertically so that it goes to exactly zero at this cutoff. The minimum in the potential is at $\Delta x = 2^(1/6)\sigma_{ws}$. We take the origin of the simulation box to be where the left wall's potential goes to infinity, and so $\Delta x = x$ is the distance from the left wall, where x is the particle's position with respect to the origin. The right wall location L_x, is also where the potential goes to infinity, so that for the right wall, $\Delta x = L_x - x$, in Eq. 3.3. The interior beads of the polymer chain are taken to be purely repulsive with respect to the flat surfaces, as represented by a shifted WCA potential:

$$U_{wb}(\Delta x) = \begin{cases} 4\varepsilon_{wb}\left[\left(\frac{\sigma_{wb}}{\Delta x}\right)^{12} - \left(\frac{\sigma_{wb}}{\Delta x}\right)^{6} + \frac{1}{4}\right] & \Delta x < 2^{1/6}\sigma_{wb} \\ 0 & \Delta x \geq 2^{1/6}\sigma_{wb} \end{cases} \tag{3.4}$$

where $\sigma_{wb} = 1.0b_K$ and $\varepsilon_{wb} = 1.0k_BT$ so that the particle begins to interact with the wall at the same position that the sticker potential, U_{ws}, is at its minimum, and so both potentials approach infinity at 0 and L_x for the left and right walls, respectively.

An actual PEO polymer in solvent at low concentration has a relaxation time that is influenced by hydrodynamic interactions (HI), but our simulated chains are freely draining, i.e., they approximate Rouse chains. We can correct, approximately, for the omission of HI, by choosing the drag coefficient of each bead ζ_{bead} in the freely draining Rouse chain to account implicitly for hydrodynamic interaction. We start by noting that the Rouse relaxation time for a polymer chain is related the intrinsic viscosity of that chain by [61]

$$\tau_R^{Rouse} = \frac{6[\eta]M_W\eta_s}{\pi^2 N_A k_B T} \tag{3.5}$$

where $\eta_s = 8.9 \times 10^{-4} Pa \cdot s$ is the solvent viscosity of water, $M_W = N_K \cdot 137 g/mol$ is the PEO polymer molecular weight, N_A is Avogadro's number, and $[\eta] = KM_W^{\nu}$ is the intrinsic viscosity of the polymer. For dilute PEO, the empirical constants in this expression are $K = 8.75 \times 10^{-6} m^3/kg$ and $\nu = 0.79$ [62]. For these given values, the "Rouse" relaxation time from Eq.3.5 is then $\tau_R^{Rouse} = 1.277 \times 10^{-11} N_K^{1.79} s$. We note that this relaxation time is a "Rouse" time only in the

sense that it depends on the intrinsic viscosity according to the formula, Eq.3.5, from Rouse theory. But the intrinsic viscosity, $[\eta] = KM_W^{\nu}$ with empirical exponent $\nu = 0.79$, scales with molecular weight according to "good solvent" scaling with internal HI within the chain. Thus, the formula for relaxation time above accounts for excluded volume (EV) and internal HI indirectly through the formula for intrinsic viscosity.

Because the simulated chains are Rouse chains with N_K Kuhn steps, the Rouse relaxation time can be related to the bead drag coefficient by

$$\tau_R^{multibead} = \frac{\zeta_{bead}(N_K+1)^2}{4\pi^2 k_B T}\frac{2b_K^2}{3} \tag{3.6}$$

Therefore, by setting $\tau_R^{multibead} = \tau_R^{Rouse}$, the bead drag coefficient ζ_{bead} can be estimated by:

$$\zeta_{bead} = \frac{36[\eta]M_W\eta_s}{N_A(N_K+1)^2 b_K^2} \tag{3.7}$$

Since $[\eta] \propto M_W^{0.79}$, and $M_W \propto N_K$, the bead drag coefficient given by Eq.3.7 is dependent on chain length. This is necessary so that the Rouse scaling of $\tau_R^{Rouse} \propto N_K^2$ is corrected to the scaling of $\tau_R^{Rouse} \propto N_K^{1.79}$ expected for a PEO chain in water, which is influenced by HI and excluded volume. The drag coefficients of a bead in chains of various lengths are given in Table 3.1. Transition times between loop and bridge conformations will be all given in terms of τ_0, a characteristic frictional time defined as $\tau_0 \equiv \zeta_{bead} b_K^2/k_B T$. We note that this use of the experimental intrinsic viscosity to calculate a chain-length-dependent bead drag coefficient is approximate not only in that it neglects the influence of HI and EV on the shape of the polymer relaxation mode distribution, but it also neglects screening of HI due to other nearby chains. The polymer adsorption density considered here however, is roughly in the "mushroom" to weakly overlapping "brush" regime, and so these approximations are hopefully not too severe.

N_K	τ_R^{Rouse}/s	$\tau_R^{Rouse}/[t]$	$\zeta_{bead}[t]/[m]$ or $\zeta_{bead}(\eta_s b_K)^{-1}$
10	7.87 $\times 10^{-10}$	2.73	1.34
40	9.41 $\times 10^{-9}$	32.70	1.15
200	1.68 $\times 10^{-7}$	582.99	0.85

Table 3.1: Rouse times and drag coefficients of HEUR polymer chains, as calculated from Eqs. 3.5, 3.6, and 3.7.

3.4 Simulation Methods

We consider the geometry in Fig. 3.1A of two parallel surfaces to which the polymers' hydrophobic endcaps can adsorb and seek to calculate the times to transition between the loop state in which both stickers are attached to the same surface, and the bridge state in which the two stickers are attached to opposing surfaces, where the attachment interaction is governed by Eq. 3.3. Our primary goal is to investigate transitions between loop and bridge configurations, between which is a "dangling" configuration with one of the stickers binding to neither surface. To avoid uninteresting (and very rare) "free chain" states in which both stickers are unbound, we simplify the simulations by taking one sticker to be adsorbed essentially irreversibly to its "anchoring wall" with binding strength $\epsilon_{ws} = 40 k_B T$, and the other "weak" sticker to be attracted to both walls with strength ϵ_{ws} set to a value between 4 and 12 $k_B T$. To relate our calculated times to those for chains with two weak sticker, we consider that, for a loop with two weak stickers transitions to a bridge, either sticker can break to form the bridge so that the transition rate is twice that of a chain with one permanently adsorbed sticker. When a polymer bridging two colloids breaks, it forms a loop on either particle with the average time of the time for a bridge with an anchored sticker to transition from bridge-to-loop, and so it does not require a correction factor.

Bridge, loop, and dangling configurations are defined by dividing the simulation box into three distinct regions along the x axis, as shown in Fig. 3.1. The boundaries of these three regions are defined using a distance $\Delta x_{cut,-1}$ from each wall, at which $U(\Delta x_{cut,-1}) = -1 k_B T$, for that wall's LJ potential, also shown in Fig. 3.1A. The value of $\Delta x_{cut,-1}$, based on the criterion that $U(\Delta x_{cut,-1}) = -1 k_B T$, varies over the range 1.57 b_K - 1.91 b_K, depending on the well potential

depth and justification for this criterion is given in the Supplemental Information in section 3.7. A chain is defined as a "loop" if its weak sticker is within the distance $\Delta x_{cut,-1}$ of the anchoring wall, as a "bridge" if its weak sticker is within $\Delta x_{cut,-1}$ of the opposite wall, and as "dangling" if the weak sticker is between the adsorption cutoffs of either wall. The 40 k_BT attraction strength between the irreversibly strong sticker end and the anchor wall ensures that the chain is always a loop, a bridge, or a dangling chain, and is never a free chain. For simplicity, from here forward, values of "sticker strengths" will always refer to the weaker of the two stickers, since we only vary the strength of this weaker sticker.

We control the grafting density of the chains by keeping the number of chains per surface fixed (N_{chains} = 500 unless stated otherwise) and adjusting the length, L_y, of a periodic simulation box with dimensions $L_x \times L_y \times L_y$, with x as the direction perpendicular to the surfaces. Polymer chains are all randomly initialized in the loop configuration (unless otherwise stated) and tethered to each of the two flat walls, with the same number of loops anchored to each wall [52]. The grafting density to each surface is then $\sigma_0 = \frac{N_{chains}}{L_y^2}$, which we make dimensionless as $2\sigma_0 R_g^2$, where $R_g = \sqrt{\frac{1}{2}\frac{N_K}{6}}b_K$ is the radius of gyration of a polymer half chain, since we assume the majority of the polymers are in the loop configuration.

When $2\sigma_0 R_g^2 < 1$, the system is in the "mushroom" regime where chains are isolated, and when $2\sigma_0 R_g^2 > 1$, it begins to enter the "brush" regime, where chains overlap and begin to stretch perpendicular to the adsorption surface.

We now wish to calculate the mean time that a chain requires to transition between loop and bridge configurations. In doing so, we wish to leave out the dangling category, which is a transitional state between a bridge and a loop. Thus, as seen in Fig. 3.1B, we regard a chain that transitions from loop to dangling and back to loop again as having not left the loop configuration, and likewise with bridge configurations. We eliminate the intermediate dangling classification because coarse-grained models, such as the population balance model of Hajizadeh et al., ignore the dangling chains, whose existence is relatively brief, because of the relatively high binding strength of the sticker [10, 21]. In addition, the "dangling" category represents a broad range of

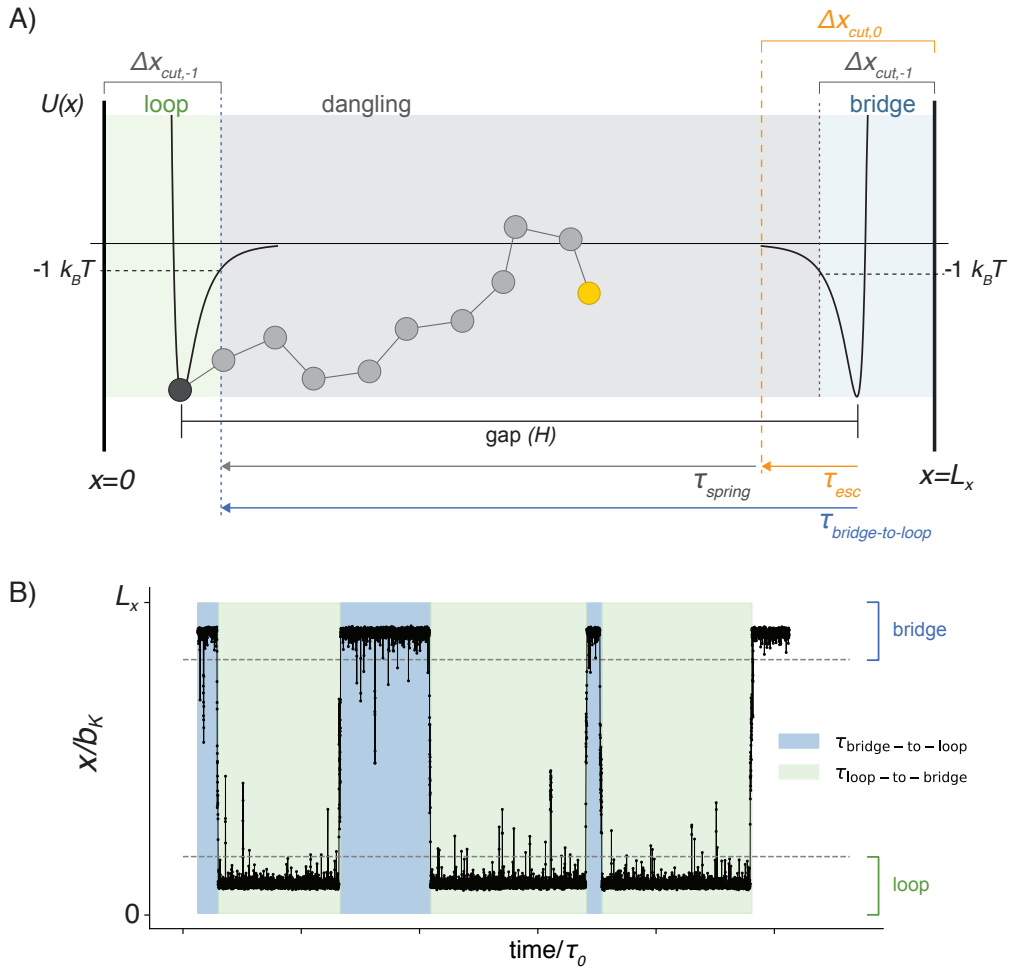

Figure 3.1: A) Diagram of a 10-Kuhn-step chain and the attractive shifted Lennard-Jones potentials defining the interaction between the weak hydrophobe (yellow) and the two boundary walls. The gap, H, indicates the distance between the two well minima. The distance $\Delta x_{cut,-1}$ from either wall is where the interaction strength between the particle and the anchor or opposing wall, respectively, is $U(x_{cut,-1}) = -1.0 k_B T$. The black bead represents the strong, "anchored," hydrophobe that is adsorbed to the anchor wall with a strong potential strength $\epsilon_{ws} = 40 k_B T$ (this strong adsorption potential is not shown), and the grey interior beads are purely repulsive with respect to the boundary walls. Green, grey, and blue shaded regions define loop, dangling, and bridge classifications for determining configuration fractions $\phi_{bridge}, \phi_{loop}, \phi_{dangling}$. B) Example trajectory of a hydrophobe transitioning between bridge and loop configurations. Dashed lines represent distances $x_{cut,-1}$ from either anchor or opposing wall as indicated. Each blue highlighted region begins when a bridge has formed by migration of the weak hydrophobe into the region denoted as "bridge" (within $\Delta x_{cut,-1}$ of the opposing wall at $x = L_x$, and ends when the bead has crossed into the region denoted "loop" (within $\Delta x_{cut,-1}$ of the anchor wall, at $x = 0$) which initiates the beginning of the green region. The width of each region samples the bridge-to-loop and loop-to-bridge transition times, respectively.

chain configurations spanning from "almost bridge" to "almost loop," and so bridge-to-loop and loop-to-bridge transitions are more relevant than accounting for various intermediate stages. Thus, we define the bridge-to-loop transition time as the time between the crossing of a chain's weak sticker to within the distance $\Delta x_{cut,-1}$ of the non-anchoring, opposite, wall (on the right side of Fig. 3.1A), and the first time it not only escapes that surface but crosses to within $\Delta x_{cut,-1}$ of the anchoring wall (blue shaded region of Fig. 3.1A). Similarly, the loop-to-bridge time is the time between a crossing to within $\Delta x_{cut,-1}$ of the anchoring wall and the first crossing thereafter back to within $\Delta x_{cut,-1}$ of the non-anchoring wall (green shaded region of Fig. 3.1A). All times at which the chain is in a dangling state are thus allocated to either the bridge-to-loop interval or the loop-to-bridge interval. Examples of the assignment of loop-to-bridge and bridge-to-loop intervals are shown in Fig. 3.1B.

3.5 Results and Discussion

3.5.1 Equilibrium Configurations

We first investigate short chains of 10 Kuhn steps. We equilibrate the system by running the simulation until the numbers of bridges, loops, and dangling chains reach constant values except for fluctuations. As seen in Fig. 3.2A, the loop-to-bridge and bridge-to-loop transition times are approximately equal at small normalized gap $H/(N_K b_K)$, where H is the distance between the minima at each of the two walls, as show in Fig. 3.1A, and is defined as $H = L_x - 2(2^{1/6}\sigma_{ws})$. For larger gaps, there is a stretching penalty for the polymer chains to achieve the bridging configuration, and so the loop-to-bridge time becomes longer and the bridge-to-loop time becomes shorter, by as much as two orders of magnitude for the former at large normalized gap. Fig. 3.2B shows transition times for varying surface coverage, which has its most pronounced effect at intermediate gap.

Although it is relatively easy to equilibrate a small system of 10-Kuhn-step chains, chain lengths more relevant to typical HEUR polymers are on the order of 200 Kuhn steps long (molec-

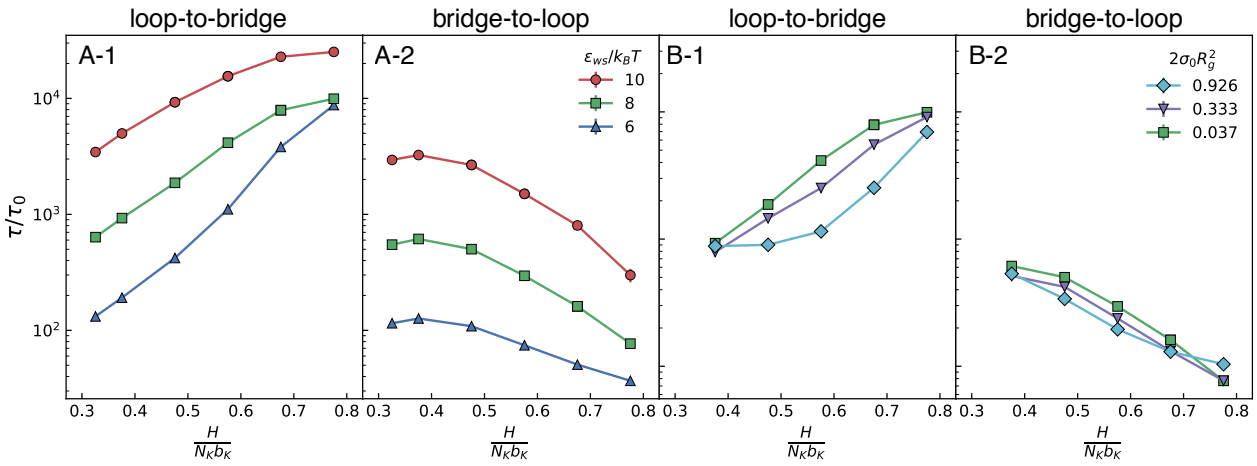

Figure 3.2: Normalized loop-to-bridge transition and bridge-to-loop transition times for equilibrated simulations of 10-Kuhn-step chains for varying normalized gap, $H/N_K b_K$, for A) varying sticker adsorption strength, ε_{ws}, at $2\sigma_0 R_g^2 = 0.037$ and B) varying surface coverage, $2\sigma_0 R_g^2$ at $\varepsilon_{ws} = 8k_BT$

ular weight $M_W \approx 27kDa$) and thus require timescales too long to readily equilibrate the bridge and loop populations and the transitions between them. However, we can circumvent these computationally expensive simulations by using the self-consistent theory (SCFT) described by Zhang et al. to compute the equilibrium numbers of bridge, loop, and dangling configurations for telechelic polymers with hydrophobes adsorbed to parallel walls [58]. At thermodynamic equilibrium, the ratio of transition rates between loops and bridges should be equivalent to the ratio of equilibrium fractions of bridges and loops $\phi_{bridges}$and ϕ_{loops}, that is:

$$\frac{\phi_{bridge}}{\phi_{loop}} = \frac{\tau_{bridge-to-loop}}{\tau_{loop-to-bridge}} \tag{3.8}$$

To check the accuracy of Eq. 3.8, we first assess how well self-consistent field theory predicts the equilibrium configuration fractions of loops, bridges, and dangling chains as calculated by the equilibrated Brownian dynamics simulations. Fig. 3.3A shows that as the sticker strength becomes large, the fraction of dangling species seen in the BD simulations diminishes and the SCFT predictions predict the configuration fractions well. However, at a high surface coverage (Fig. 3.3B), simulations show a significant fraction of dangling chains not predicted by self-consistent field theory, such that both loop and bridge configurations are less than predicted by SCFT.

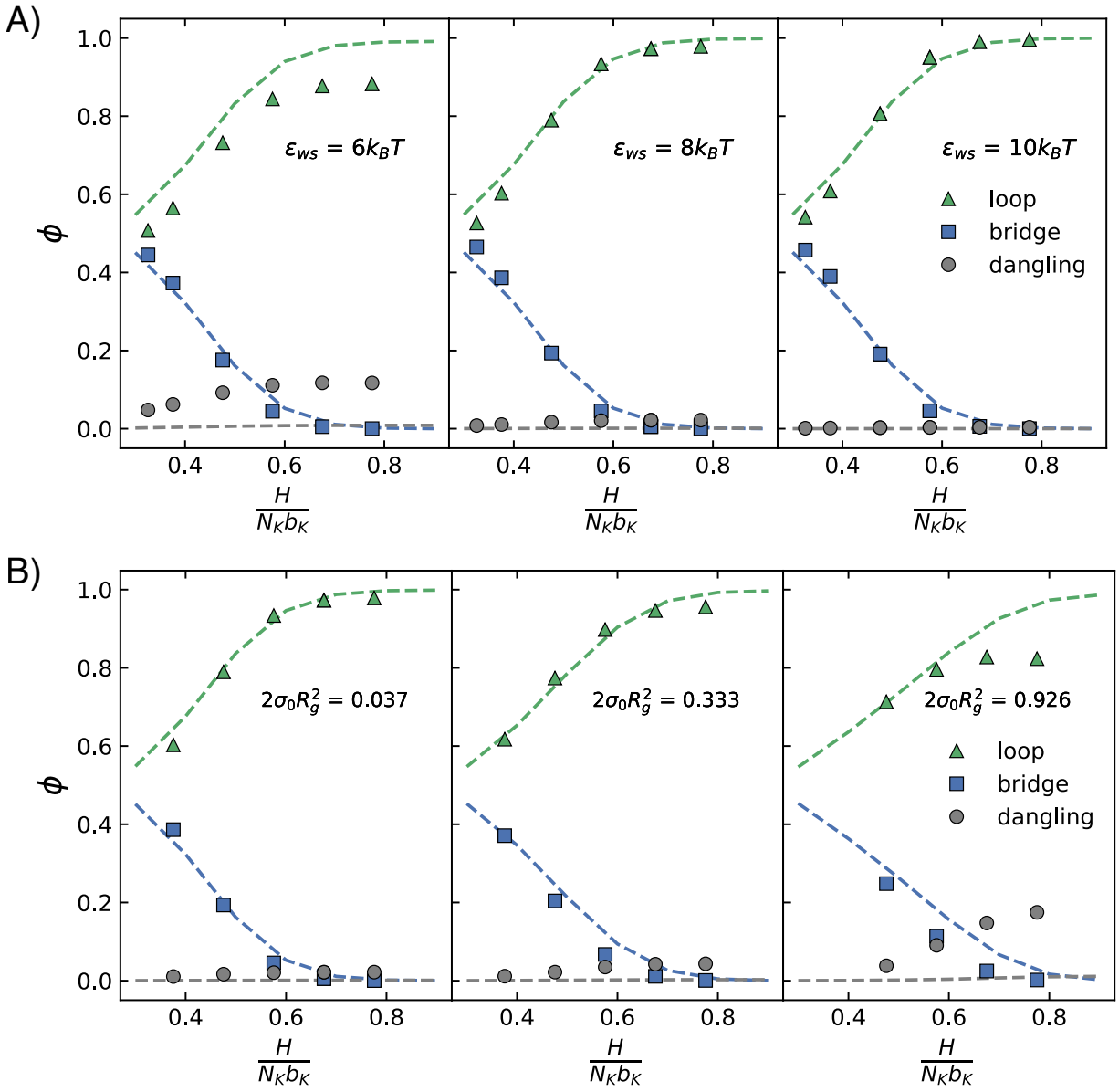

Figure 3.3: Fraction of polymer chains in loop (triangles), bridge (squares), and dangling (circles) configurations as a function of normalized gap ($H/N_K b_K$) for A) varying hydrophobic strengths ($\varepsilon_{ws} = 6, 8, 10 k_BT$) at $2\sigma_0 R_g^2 = 0.037$ and B) varying surface densities ($2\sigma_0 R_g^2 = 0.037, 0.333, 0.926$) for hydrophobic sticker strength of $\varepsilon_{ws} = 8k_BT$. For all sub-figures, symbols represent configuration fractions from equilibrated Brownian dynamics simulations and dashed lines are configuration fractions from self-consistent field theory, for 10-Kuhn-step chains.

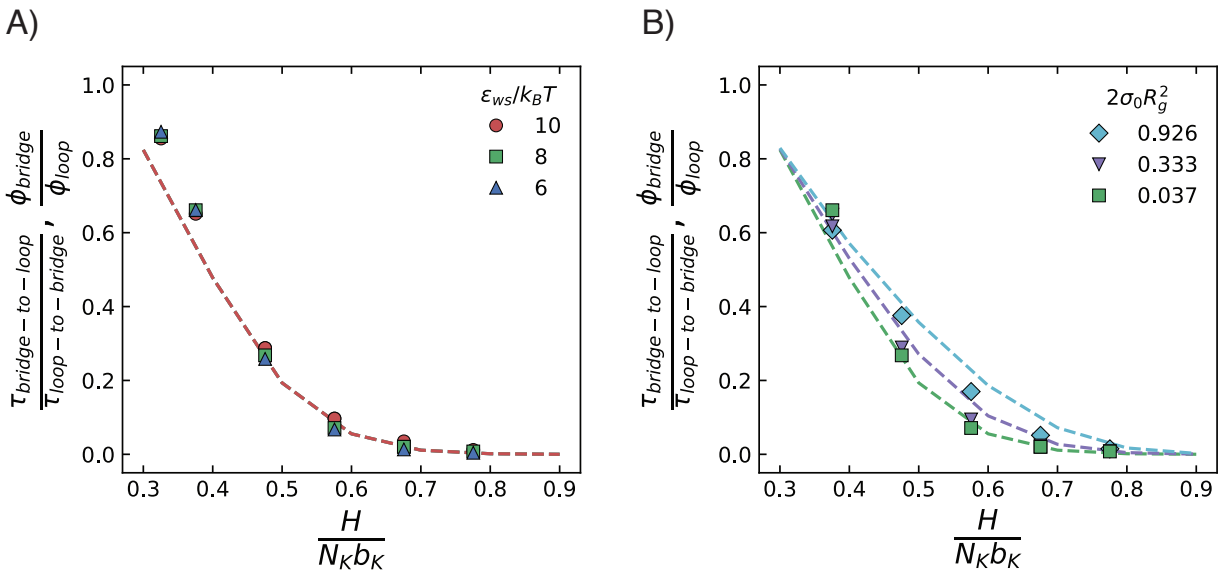

Figure 3.4: SCFT predictions for the ratio of chains in bridge and loop configurations, $\phi_{bridge}/\phi_{loop}$ (dashed lines), and the ratio of transition times, $\tau_{bridge-to-loop}/\tau_{loop-to-bridge}$, calculated from equilibrated BD simulations (markers) for A) varying weak hydrophobic strengths ($\varepsilon_{ws} = 6, 8, 10 k_BT$) at $2\sigma_0 R_g^2 = 0.037$ and B) varying surface densities ($2\sigma_0 R_g^2 = 0.037, 0.333, 0.926$) for hydrophobic sticker strength of $\varepsilon_{ws} = 8 k_BT$.

A comparison of $\phi_{bridge}/\phi_{loop}$ predicted by SCFT and $\tau_{bridge-to-loop}/\tau_{loop-to-bridge}$ calculated from BD simulations is shown in Fig. 3.4A. Both the predictions and simulations each collapse onto curves that are independent of the sticker strength, indicating that these ratios are equilibrium properties. There is a noticeable difference between predicted and simulated results at small inter-surface gap, which is likely due to the SCFT calculations being discretized on a lattice of 1 b_K segments. At small gaps that are approaching the size of the lattice segments themselves, the lattice is no longer an accurate approximation of continuous space.

Fig. 3.4B shows that the ratios N_{bridge}/N_{loop} and $\tau_{bridge-to-loop}/\tau_{loop-to-bridge}$ both increase for increasing surface coverage, but SCFT over-predicts this effect. The increase in this ratio is likely due to "squeeze-out" of chains from loops configurations into less crowded bridge configurations as chain density increases. However, given the slight-to-moderate effect of surface density on transition rate, only low surface coverage cases will be considered in the remainder of this work.

We can now use self-consistent field theory to predict $\phi_{bridge}/\phi_{loop}$, and therefore the ratio of transition times, for longer chain lengths whose equilibration is inaccessible with BD simulations.

Fig. 3.5A the shows predicted bridge, loop, and dangling configurations for 10, 40, and 200 Kuhn step chains. For all chain lengths, the configuration fractions converge at high sticker strengths ($\varepsilon_{ws} \geq 10k_BT$), with longer chains requiring larger values of ε_{ws} to converge. As seen in Fig. 3.5B, the ratios $\phi_{bridge}/\phi_{loop}$ for all chain lengths collapse onto a single curve when the inter-surface gap is normalized by $b_K\sqrt{N_K}$, or the root-mean-squared end-to-end distance of a freely jointed polymer chain N_K Kuhn steps in length. We empirically fit the following function to the collapsed curve:

$$\frac{\phi_{bridge}}{\phi_{loop}} = \frac{1}{1+\exp\left[4.88\left(\frac{H}{b_K\sqrt{N_K}}\right)-1.32\right]} \tag{3.9}$$

This curve, shown in Fig. 3.5B, and can be used along with the relationship given in Eq. 3.8 to calculate the inaccessibly long $\tau_{loop-to-bridge}$ times from the much shorter, more computationally feasible, $\tau_{bridge-to-loop}$ times:

$$\tau_{loop-to-bridge} = \tau_{bridge-to-loop}\left(1+\exp\left[4.88\left(\frac{H}{b_K\sqrt{N_K}}\right)-1.32\right]\right) \tag{3.10}$$

Therefore, the focus of the remainder of this work is the calculation of bridge-to-loop transition times for longer, more experimentally relevant, polymer chains.

3.5.2 Calculating bridge-to-loop transition times

To calculate the bridge-to-loop transition times, we run simulations identical to those described in the previous section, but with 200 of the 500 polymers on each surface initialized in the bridging configuration. For 200-Kuhn-step polymers, 100 of 200 polymers on each surface were initialized as bridges to the opposite surface and the remainder were left as loops. The simulations were then run until all the polymers initialized as bridges had transitioned to the loop configuration, as indicated by $\tau_{bridge-to-loop}$ in Fig. 3.1A.

We analyze the bridge-to-loop transition time by dividing it into two distinct processes as shown in Fig. 3.1A, each with a characteristic time: 1) τ_{esc}, the time for the sticker (attached to a polymer) to escape from the Lennard Jones well and 2) τ_{spring}, the time for a sticker to travel

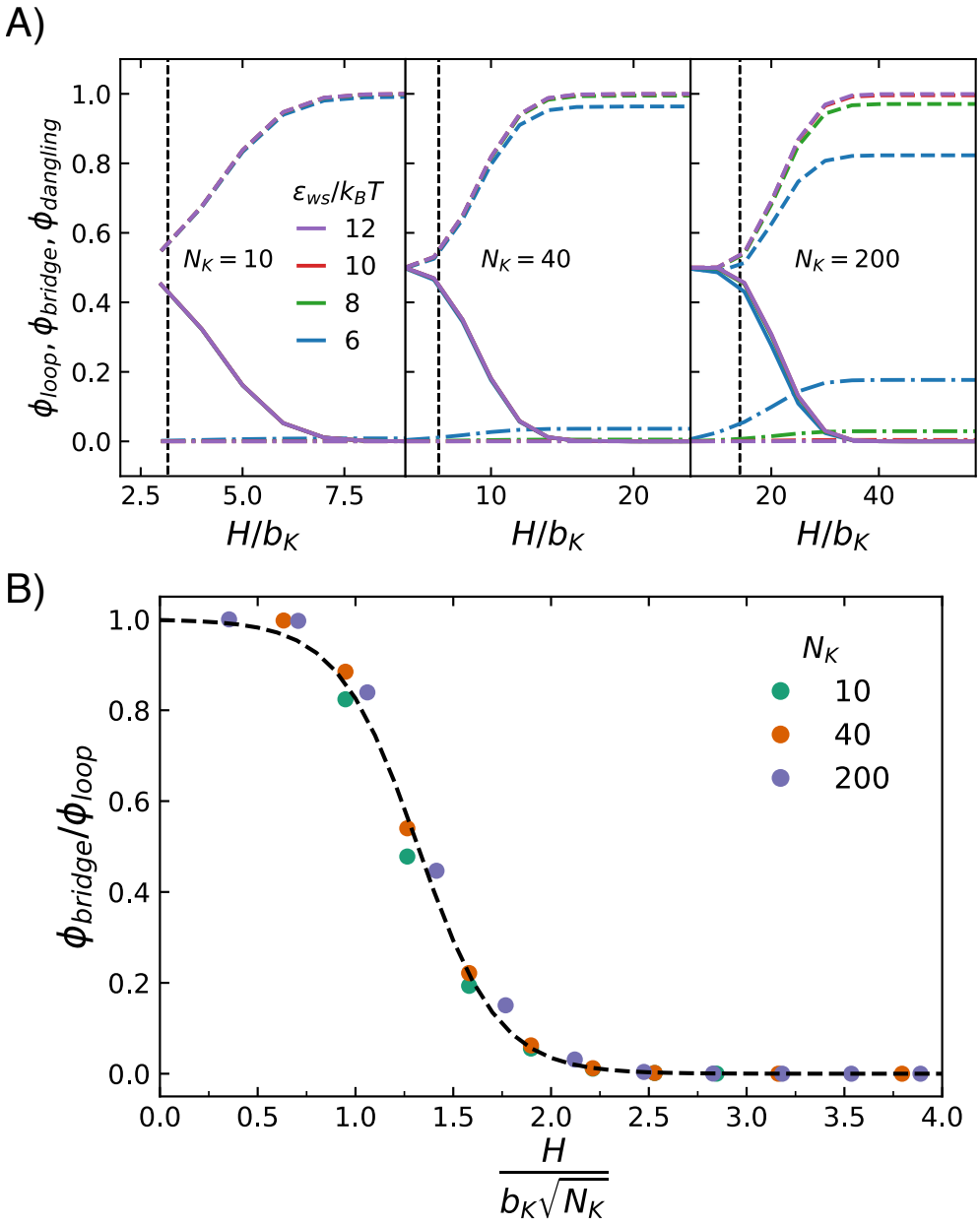

Figure 3.5: A) Self-consistent field theory predictions for fraction of chains in loop (dashed lines), bridge (solid lines), and dangling (dot-dashed lines) configurations for polymer chains 10, 40, and 200 Kuhn steps in length. B) Ratio of the number of chains in bridge configurations to the number of chains in loop configurations for 10, 40, and 200 Kuhn steps where the inter-surface gap, H, is normalized by the theoretical root-mean-squared end-to-end distance of the polymer chain, $b_K\sqrt{N_K}$. Black dashed line represents Eq. 3.9.

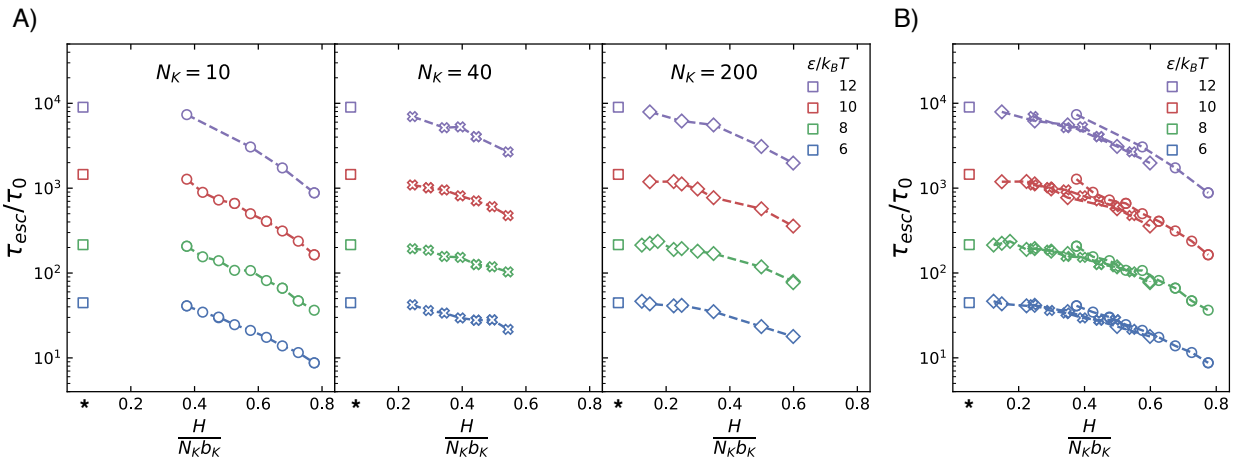

Figure 3.6: A) Normalized escape times for polymers with lengths 10 (circles), 40 (x's), and 200 (diamonds) Kuhn steps and hydrophobic sticker strengths listed in the legend. Open squares represent normalized escape times of a single hydrophobic particle not attached to a polymer $\tau_{esc}^{particle}$, also indicated by the "*" label on the x-axis. B) Identical data to A), but combined into a single plot, where the symbols have the same meaning as in A).

from the edge of the potential back to the loop configuration in the absence of the sticker wall potentials. At small normalized gap, the escape time of the polymer's hydrophobic end-bead, τ_{esc}, converges to the particle escape time for a lone hydrophobic bead not attached to a polymer chain, $\tau_{esc}^{particle}$, (open squares in Fig. 3.6). At large normalized gap, the tension of the stretched polymer chain counteracts the attractive adsorption potential, so that the escape time decreases with increasing normalized gap. Fig. 3.6B demonstrates that τ_{esc} is nearly independent of the polymer chain length, N_K, and instead only depends on the normalized gap that the polymer chain spans in the bridging configuration, $H/N_K b_K$, and the hydrophobe strength, ε_{ws}. Because for 200 Kuhn steps (the chain length of experimental interest) there is a vanishingly small fraction of bridges at inter-surface distances larger than 50 b_K, we are most interested in capturing the behavior smaller than this inter-surface distance, or where $H/(N_K b_K) \leq 0.25$. Therefore, we can assume that, in the regime of long chains and small or moderate interparticle gaps, that the escape time, τ_{esc} for a hydrophobe attached to a chain is approximately equal to that of a lone particle.

In models of HEUR telechelic chains, it has been approximated that $\tau_{esc}^{particle}$ is equivalent to $\tau_{bridge-to-loop}$, which assumes that the bridge-to-loop transition time is not dependent on either

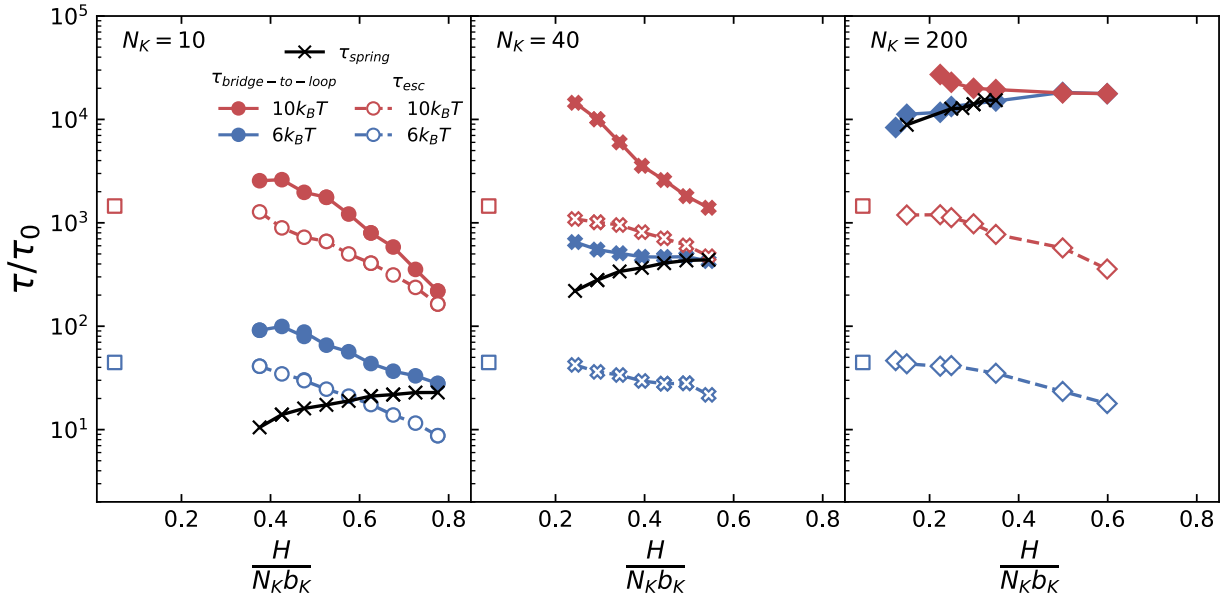

Figure 3.7: Characteristic times τ_{spring} (black line, x symbols), τ_{esc} (open symbols, dashed lines), and $\tau_{bridge-to-loop}$(filled symbols, solid lines) as shown in Fig. 3.1 for A) 10, B) 40, and C) 200 Kuhn step polymer chains with attractive sticker strength $\varepsilon_{ws} = 6k_BT$ (blue) and $10k_BT$ (red) at grafting density $\sigma_0 R_g^2 = 0.037$.

the normalized gap or the chain length (N_K) of the telechelic polymer [55, 10]. However, as seen in Fig. 3.7, $\tau_{bridge-to-loop}$ is longer than τ_{esc} (as well as $\tau_{esc}^{particle}$), and the difference between these two characteristic times becomes much larger for longer chain lengths. It is important to note that, for high hydrophobic strength, at small normalized gap, the deviation between τ_{esc} and $\tau + bridge - to - loop$ decreases as normalized gap increases. At high normalized gap, there is a low probability of the hydrophobe re-entering the potential well after its initial escape, due to the retractive spring force of the polymer chain, which causes a transition to a loop configuration once the sticker has escaped its well. The number of re-entries to the bridge state, which increases at smaller gaps, multiplies the escape time τ_{esc}, to give an increased bridge-to-loop transition time, since for every re-entry the particle must undergo a new escape process with time scale τ_{esc}.

The data in Fig. 3.7 show that for sufficiently long chains and weak hydrophobic strengths, τ_{spring} dominates the bridge-to-loop transition time and the wall potential has little effect. For long chains and moderate hydrophobic binding strength (ε_{ws}), the spring retraction time is considerably longer than the time required for a particle to escape the wall potential, $\tau_{spring} \gg \tau_{esc}^{particle}$, since the

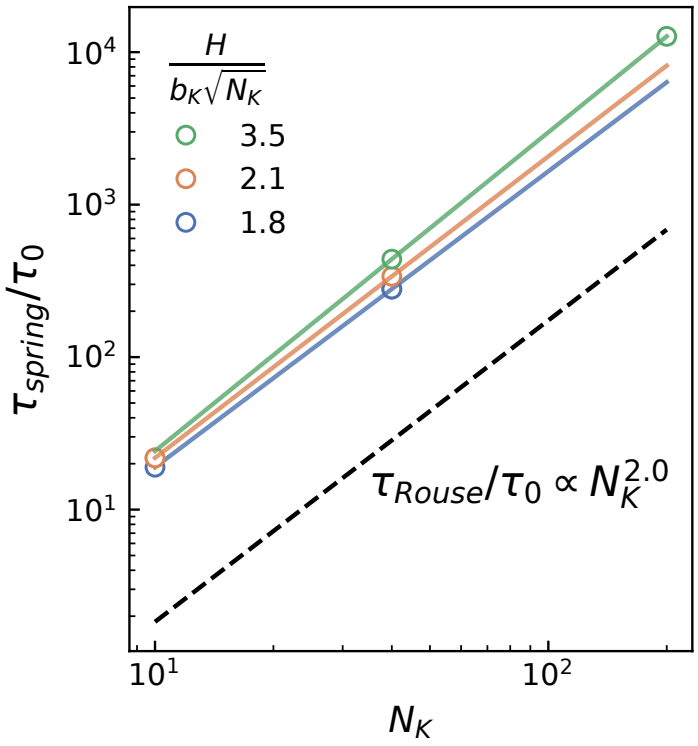

Figure 3.8: Spring retraction time, τ_{spring}, as a function of chain length N_K, for varying normalized gaps, $H/(b_K\sqrt{N_K})$ and approximate fits to show scaling behavior. Normalized Rouse times, τ_{Rouse}/τ_0 from Table 3.1 are shown as the black dashed line.

polymer retraction force is weak and the hydrophobe has a relatively long distance to retract. Fig. 3.8 shows that when inter-surface gap normalized by the root-mean-squared end-to-end distance is held fixed, the spring retraction time scales as the Rouse time, $\tau_R^{Rouse}/\tau_0 \propto N_K^2$. Note that while we attain Rouse scaling for τ_R^{Rouse}/τ_0, τ_R^{Rouse} itself scales as $N_K^{1.79}$ because τ_0 depends on the number of beads, through dependence of the drag coefficient, ζ_{bead}, on N_K as discussed earlier.

To understand how the scaling of τ_{esc} relates to $\tau_{bridge-to-loop}$, we use Larson and Lightfoot's theory for predicting the escape time of an overdamped Brownian particle from a Lennard-Jones potential well [63, 61]:

$$\tau_{esc} = \tau_0\left(\frac{\pi k_B T}{\varepsilon_{ws}}\right)^{1/2} \frac{\frac{\Delta x_{cut}}{b_K} - (\frac{4\varepsilon}{k_B T})^{1/n}\Gamma(1-\frac{1}{n})}{n2^{1/n}} e^{\varepsilon_{ws}/k_B T} \tag{3.11}$$

In Eq. 3.11, the characteristic frictional time is $\tau_0 \equiv \zeta_{bead} b_K^2/k_B T$, Δx_{cut} is the distance

from the wall at which the particle is considered escaped, taken here to be $\Delta x_{cut,0} = 2.5b_K$, and $n = 6$ is the Lennard-Jones coefficient for the 12-6 LJ potential we are using. In Fig. 3.9, it is clear that there are two distinct scaling regimes: 1) where $\tau_{bridge-to-loop}$ converges to τ_{spring} for weaker hydrophobic strength, and 2) where $\tau_{bridge-to-loop}$ appears to scale as $\tau_{esc}^{particle}$ when the $\tau_{esc}^{particle} \gg \tau_{spring}$. The short 10 Kuhn step chains' bridge-to-loop times have the same scaling as a lone particle's escape time for $\varepsilon_{ws} > 4k_BT$. However for $N_K = 40$ and $N_K = 200$, this transition doesn't occur until approximately $\varepsilon_{ws} > 8k_BT$ and $> 12k_BT$, respectively. From the trend shown in Fig. 3.9, it appears that the bridge-to-loop time of a 200 Kuhn step chain will approach the same scaling with ε_{ws} as exhibited by $\tau_{esc}^{particle}$ at sufficiently high ε_{ws}, although likely with an offset in the prefactor that depends on chain length, as indicated by the lack of convergence of the red and green curves to the grey one at large ε_{ws}.

Experimental HEUR polymers most relevant to waterborne coatings have hydrophobic strengths in the range of $\varepsilon_{ws} \approx 10 - 20k_BT$, and chain lengths of around $N_K \approx 100 - 500$. Thus, within these relevant ranges, $\tau_{bridge-to-loop}$ can be approximated to be a factor of 2-5 times τ_{esc}, at relatively high ε_{ws} ($> 12k_BT$) and/or low N_K (~ 200). At the other extreme of lower ε_{ws} ($\sim 10k_BT$) and higher N_K (> 100), τ_{spring} can provide an appropriate approximation of $\tau_{bridge-to-loop}$. For typical experimental HEURs for intermediate conditions between these ranges, neither τ_{spring} nor τ_{esc} provide appropriate approximations of $\tau_{bridge-to-loop}$.

More generally, we can directly compute bridge-to-loop transition times using BD simulations, and then use the relationship in Eq. 10 to compute the loop-to-bridge transition times to present a complete picture of bridging dynamics of HEUR polymers, as shown in Fig. 10.

3.6 Conclusions

We performed simulations of rheology-modifying polymers using a bead-spring model with excluded volume to compute the characteristic transition times between bridge and loop configurations between flat parallel surfaces. We used the equilibrium ratio of bridges and loops,

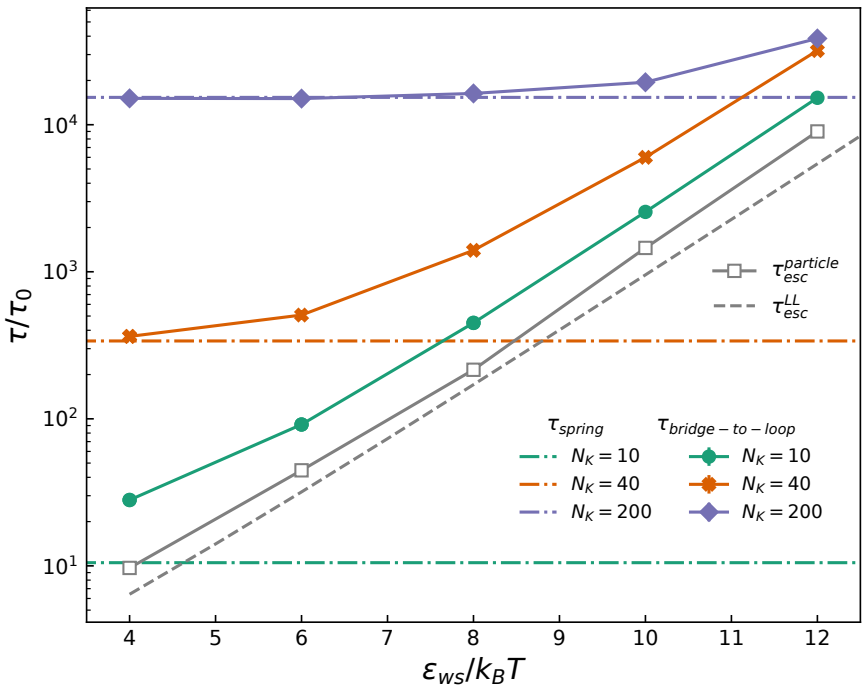

Figure 3.9: Bridge-to-loop transition times (solid symbols and solid lines) and spring retraction times (dot-dashed lines) for varying chain lengths, N_K, all at normalized gap $H/b_K N_K = 0.36$. Grey dashed line represents Larson-Lightfoot predictions from Eq. 3.11 and open grey squares with solid grey line represent escape times, $\tau_{esc}^{particle}$, for a hydrophobic particle not connected to a polymer chain.

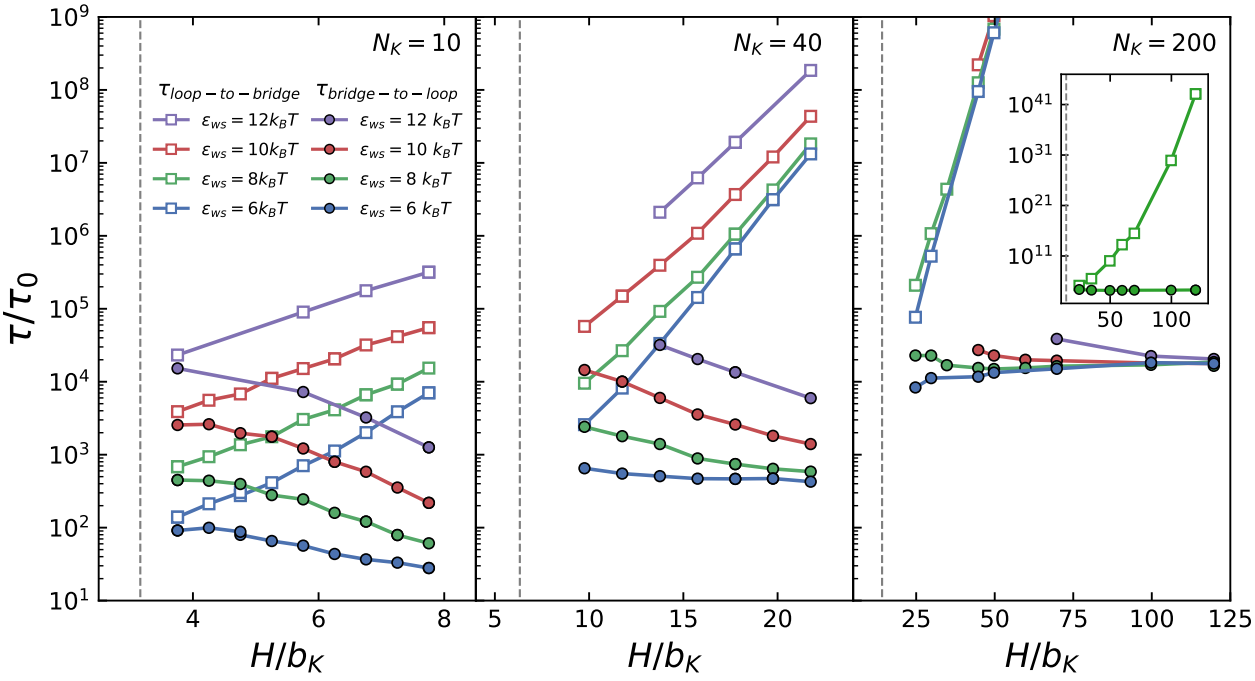

Figure 3.10: Normalized bridge-to-loop transition times (filled circles) of chains initialized in bridging configurations and corresponding predicted loop-to-bridge transition times (open squares) calculated from SCFT predictions and Eq. 3.10. Inset on far right shows data for $N_K = 200$ and $\varepsilon_{ws} = 8k_BT$, with an extended y-axis not shown on the main plot.

$\phi_{bridge}/\phi_{loop}$, predicted by an established lattice self-consistent field theory (SCFT) method, and showed that the equilibrium information from SCFT can be used to compute the slow loop-to-bridge transition from the faster and more computationally feasible bridge-to-loop time. We showed that $\phi_{bridge}/\phi_{loop}$ ratios from SCFT for various chain lengths as a function of the inter-surface gap collapses onto a single curve when the inter-surface gap is normalized by the root-mean-square end-to-end distance of the polymer chain. This eliminates the need for SCFT to be used for other chain lengths and allows the slower loop-to-bridge transition time to be calculated from BD simulations of the faster bridge-to-loop transition. From these elements, we present a complete picture of transition times for experimentally relevant chain lengths and hydrophobe strengths. We show that the bridge-to-loop transition time ($\tau_{bridge-to-loop}$) can only be approximated roughly by the time for a hydrophobe to desorb from a surface (τ_{esc}), in limited circumstances of strong hydrophobe binding and relatively short chains. For longer chains, but still within the typical experimental range, and weaker sticker strengths, the chain retraction time (τ_{spring}) is several orders of magnitude longer than the desorption time.

This approach to predicting dynamic polymer behavior can be useful for understanding the behavior of formulations containing colloids and telechelic polymers. Specifically, these transition rates have direct application to the Population balance – Brownian Dynamics (Pop-BD) simulations, a coarse-grained method for predicting the rheological behavior of waterborne coatings containing HEUR polymers and latex colloids [10]. Connecting the results obtained here to simulations of networks of HEURs bound to colloids will be the subject of future work.

3.7 Supplemental Information: Rationale of cutoff distance for computing transition times

In our studies of 10-Kuhn-step polymer chains at equilibrium, we initially took the value of Δx_{cut}, (the boundary between bridge and dangling or between loop and danging) to be 2.5 b_K from either wall, so that $\Delta x = 2.5 b_K$ in Eq. 3.3. Using this criterion, we observed a discrepancy between the

breakage times for chains that are initialized as bridges, or "primary bridges," and chains that are initialized as loops and subsequently form bridges, or "secondary bridges." This secondary bridge escape time can be significantly faster than the primary bridge time for large Δx_{cut} because the primary bridges are all allowed to go to the well minimum before the simulation starts, whereas the secondary bridges might only reach the cutoff distance Δx_{cut} without going fully to the well minimum before breaking again. These weakly adsorbed bridges thus can break faster than those initialized at the deepest part of the Lennard-Jones well.

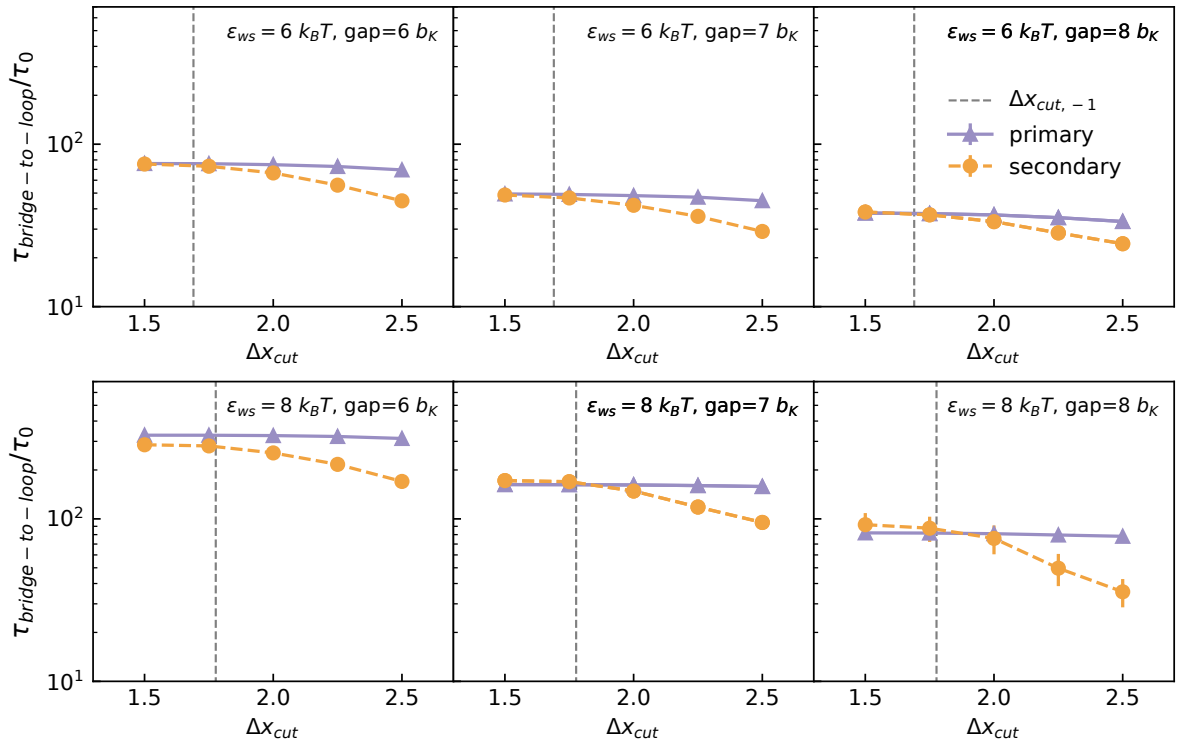

Figure 3.11: Primary (purple triangles connected by solid lines) and secondary (orange circles connected by dashed lines) for polymer chains 10 Kuhn steps in length and for weak sticker strengths, ε_{ws}, equal to $6k_BT$ (top) and $8k_BT$ (bottom) and "gap" or box length, L_x equal to 6, 7, and 8 b_K.Vertical grey dashed lines indicate $\Delta x_{cut,-1}$.

To take advantage of the relationship described in Eq. 3.8, we wished to specifically study the bridge-to-loop transition time of longer, 40- and 200-Kuhn-step, polymer chains by initializing a fraction of the polymer chains as primary bridges and tracking their transition to becoming loops. In this section, we show that choosing the cutoff criteria to be $x_{cut,-1}$, or the position at which

$U(x) = -1k_BT$, satisfies this requirement for our system of interest.

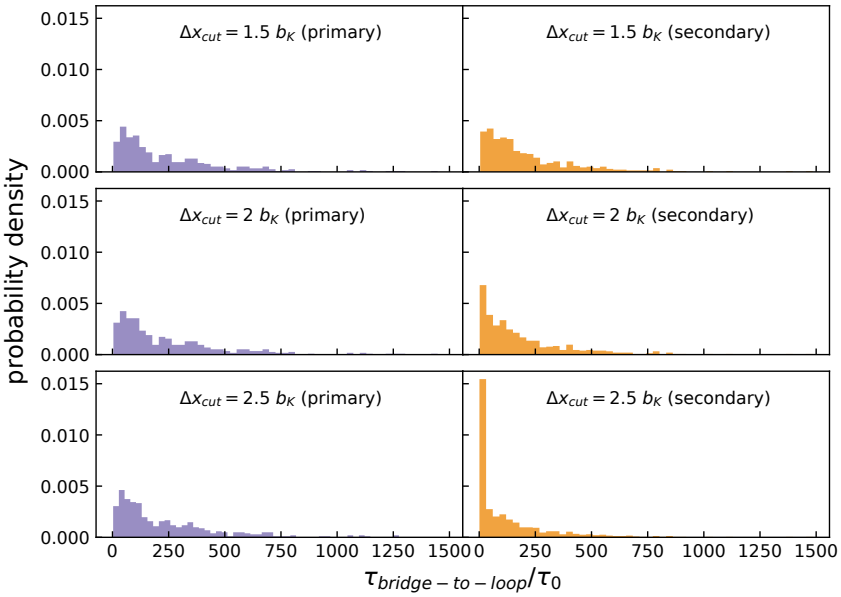

Figure 3.12: Histograms of bridge-to-loop times for varying Δx_{cut} and primary (left, purple) and secondary (right, orange) bridges.

We compare the bridge-to-loop times for varying values of Δx_{cut}, so that we can determine the value of Δx_{cut} at which primary and secondary bridges have approximately equal escape times. Once we have identified an appropriate value of Δx_{cut}, we can use the primary bridge breakage time as representative of the bridge-to-loop time for a polymer in an equilibrated system. Fig. 3.11 shows the bridge-to-loop times for primary and secondary bridges for a range of Δx_{cut} values. The primary bridge-to-loop transition times are nearly independent of Δx_{cut}, since all the sticker particles are initialized in the well minima. However, the secondary transition times decrease significantly with increasing Δx_{cut}, because there is a significant fraction of sticker particles that do not reach the bottom of the potential well, and thus contribute an artificially small bridge-to-loop time. This effect can be seen in Fig. 3.12, which shows the distribution of breakage times for primary and secondary bridges at $\Delta x_{cut} = 2.5 b_K$. There is a large population of very short secondary bridge-to-loop transition times that is absent from the distribution of primary bridge-to-loop transition times.

3.8 Acknowledgements

The computational workflow and data management for this publication were primarily supported by the signac data management framework [64]. This work was supported in part by the National Science Foundation under Grant No. 1707640. Any opinions, findings, and conclusions or recommendations expressed in this material are those of the authors and do not necessarily reflect the views of NSF. This work used the Extreme Science and Engineering Discovery Environment (XSEDE), which is supported by National Science Foundation grant number ACI-1548562 [65]. This research was supported in part through computational resources and services provided by Advanced Research Computing at the University of Michigan, Ann Arbor. This research was also supported in part through computational resources and services provided by Advanced Research Computing at the University of Michigan, Ann Arbor.

CHAPTER 4

Transitioning From Underdamped to Overdamped Behavior in Theory and in Langevin Simulations of Desorption of a Particle From a Lennard-Jones Potential

Disclosure: The content of this chapter has been reproduced from Travitz, A., Mani, E., and Larson, R.G. *Transitioning From Underdamped to Overdamped Behavior in Theory and in Langevin Simulations of Desorption of a Particle From a Lennard-Jones Potential.* Journal of Rheology (accepted), with the permission of AIP Publishing.

4.1 Abstract

We investigate the transition between the overdamped and underdamped regimes in Langevin dynamics simulations with significant conservative forces by comparing direct simulations with theory by Kramers, by Mel'nikov and Meshkov, and by Larson and Lightfoot. The need for clarification is made evident by noting that the most commonly cited theories of Kramers and of Mel'nikov and Meshkov (MM) do not apply in the overdamped limit to escape times from a Lennard-Jones (LJ) potential, because Kramers and MM do not account for the flatness of the LJ potential at the escape position, which allows for a region of nearly free Brownian diffusion near the escape

position. While the little-known Larson-Lightfoot (LL) approach does consider a Lennard-Jones potential, it does not properly consider the underdamped regime, and so a complete description is only achieved by combining the LL and MM results into a single general equation, which we validate for the first time by explicit comparison with Langevin simulations.

4.2 Introduction

Langevin and Brownian dynamics simulations of complex fluids are becoming increasingly common as computational power increases and these tools are being extended to ever more complex systems. While simulations of simple monodisperse polymers and suspensions of spheres have been carried out for many years, such tools can now be applied to more complex systems, including, for example, mixtures of polymers and colloids[66], gelling systems[67], micellar systems[68], semi-flexible polymers, etc.[69]. Open-source tools for such simulations are often used instead of homegrown code due to their efficiency, flexibility, and reproducibility. Such open-source software, including the well-known LAMMPS and HOOMD-blue packages, solve the Langevin equation [60, 70]:

$$m_i \frac{d^2 r_i}{dt^2} = -\zeta_i \frac{dr_i}{dt} + F_i^C + F_i^R \tag{4.1}$$

Here, m_i is the mass of i^{th} species, r_i is the particle position, ζ_i is its drag coefficient, F_i^C is the conservative force due to inter- and intra-species interactions, and F_i^R is the random force due to solvent interactions (Gaussian noise). This equation is typically solved at constant NVT (canonical ensemble). In HOOMD-blue, the drag coefficient is directly defined, while in LAMMPS, one specifies the drag coefficient, ζ, via an inertial time defined for each species as

$$t_{in} = \frac{m}{\zeta} \tag{4.2}$$

where the subscript, i, denoting the i^{th} species, is omitted here for clarity. Because t_{in} is inversely proportional to the drag coefficient, viscous damping actually becomes weaker as this so-called

"damping parameter," as defined in LAMMPS, becomes larger. When $t \ll t_{in}$, a free particle (with $F_i^C = 0$) undergoes ballistic motion dominated by inertia due to its mass m, while for $t \gg t_{in}$, it undergoes diffusive motion dominated by its drag coefficient, ζ. That is, it attains the overdamped regime at long times, where inertia becomes unimportant. The limit in which particle mass is taken to be zero is the overdamped limit, and solutions of corresponding equations, lacking the acceleration term in Eq.4.1, are referred to as "Brownian dynamics," since apart from conservative forces only Brownian forces drive particle motion.

Since most problems of interest in such simulations are concerned with behavior in the overdamped regime, when solving the Langevin equation, one must be careful to choose to achieve the overdamped regime where particle masses no longer affect the results. A simple "rule of thumb" for doing so is to make sure that the inertial time t_{in} is less than any relaxation time relevant to the physical problem, so that inertial effects present at short times have decayed by the time the physics of interest emerge in the solution. While choosing a small value for t_{in} helps ensure attainment of the overdamped regime, smaller values can be computationally wasteful, since time step sizes generally must be on the order of, or smaller than, t_{in}, unless the mass is set to zero.

Although the above criterion, $t \gg t_{in}$ for attaining the overdamped limit applies to free particle diffusion in the absence of a conservative force, it is well known that when a potential is present, the escape time of the particle from a potential can be affected by inertia even when the particle's escape time is much longer than t_{in} [71]. Much literature addresses this escape time in the presence or absence of inertia, including the classic paper of Kramers[71], the more recent and complete work of Mel'nikov and Meshkov (MM) [72] and the little-noticed work of Larson and Lightfoot [61] (LL, where this Larson is not an author of our paper). However, we have found that the application of this literature to complex fluid simulations can be confusing, because of several points that need clarifying:

1. When an attractive potential is present, attainment of the overdamped regime is not controlled only by the timescale of the escape relative to the inertial time, $t_{in} = m/\zeta$, but is influenced by the depth and shape of the potential well.

2. The standard Kramers theory, and even the more complete theory by Mel'nikov and Meshkov, only apply to the overdamped regime if the escape from a potential well occurs at a local maximum with downward curvature in the potential. Therefore, these approaches do not apply to conventional and widely used Lennard-Jones potential wells, which become flat at the position where the particle escapes the well.

3. The only theory that considers particle escape from a Lennard-Jones potential is the little-cited work by Larson and Lightfoot. However, their work is also incomplete in its description of the transition to the fully underdamped regime because it does not account for the action of the particle or the entire shape of the potential in limit of small friction.

4. The slope of the potential at the point of escape is irrelevant in the underdamped regime, so that the Mel'nikov-Meshkov (MM) theory correctly describes particle escape in this regime even for a Lennard-Jones potential. As a result, a complete description of particle escape from the LJ potential is obtained by combining the LL theory for the overdamped limit with the MM theory for the underdamped regime.

Because few of those simulating complex fluids seem to be aware all of the above points, as demonstrated by earlier work in our group which includes errors resulting from this ignorance, it is useful to review carefully the implications of the key papers by Mel'nikov and Meshkov (MM), Larson and Lightfoot (LL), and Kramers [71, 72, 61, 22]. It is also important to compare the predictions of these theories with Langevin simulations of the escape of a particle from a Lennard-Jones potential well, so that the various regimes and effects of the different approximations are clearly demonstrated and the conditions for transition between underdamped and overdamped regimes are clearly defined. We also seek to provide an expression for the average escape time from a Lennard-Jones potential well that encompasses all regimes of inertia and well depth that can be used in mesoscopic simulations.

4.3 Evaluating theoretical approaches

One-dimensional transport of a particle in either free space or in a potential well is described by a Fokker-Planck equation for position and momentum, given in multiple sources[71, 61, 73]. The non-dimensionalized mean first passage time for particle escape, τ_{esc}/τ_0, is defined as the time for first crossing of a distance criteria, z_{cut} (typically near or at the upper edge of a potential well), where τ_0 is a characteristic frictional time defined as $\tau_0 \equiv \zeta a^2/k_BT$. Assuming a fixed value of z_{cut}, this dimensionless escape time τ_{esc}/τ_0 is a function of two dimensionless groups, namely the dimensionless well depth ε/k_BT and the dimensionless friction constant $\alpha \equiv \frac{\zeta^2 a^2}{mk_BT}$, where a is the distance unit comparable to the width of the well. The classical and best-known solutions to this problem define the crossing point for escape of the particle to be at the local maximum of the potential well, denoted as z_{cut} in Fig.4.1A, providing an unambiguous location for escape beyond which the potential acts as a barrier to re-entry.

The most complete solutions to this problem are those of Kramers and of Mel'nikov and Meshkov, both using a pseudo-steady-state (PSS) approximation, but with Kramers' most "general" solution also assuming that α is "not so small that energy uptake from the heat bath... is a limiting factor in determining the escape rate"[71, 72, 61]. Kramers handled the limit of "very small" α with a separate asymptotic formula, which was not encompassed by his otherwise "general" solution for damping ranging from moderately damped to overdamped. The Mel'nikov-Meshkov solution, however, does encompass the case of arbitrarily small α and provides a solution valid for the entire range of α. Both the Kramers and Mel'nikov-Meshkov solutions, however, require the presence of a well-defined potential well $U(x)$ that is sufficiently deep to permit the PSS assumption, with a region of positive curvature defining its bottom, and a region of negative curvature defining its top, which is taken as the point z_{cut} beyond which the particle has escaped (see Fig. 4.1A).

Thus, both Kramers and Mel'nikov-Meshkov solutions, and in fact, almost the entirety of the literature on this problem, exclude one of the most common potentials, the Lennard-Jones (LJ) potential, which has no local maximum, but only a gradual flattening of the potential at large dis-

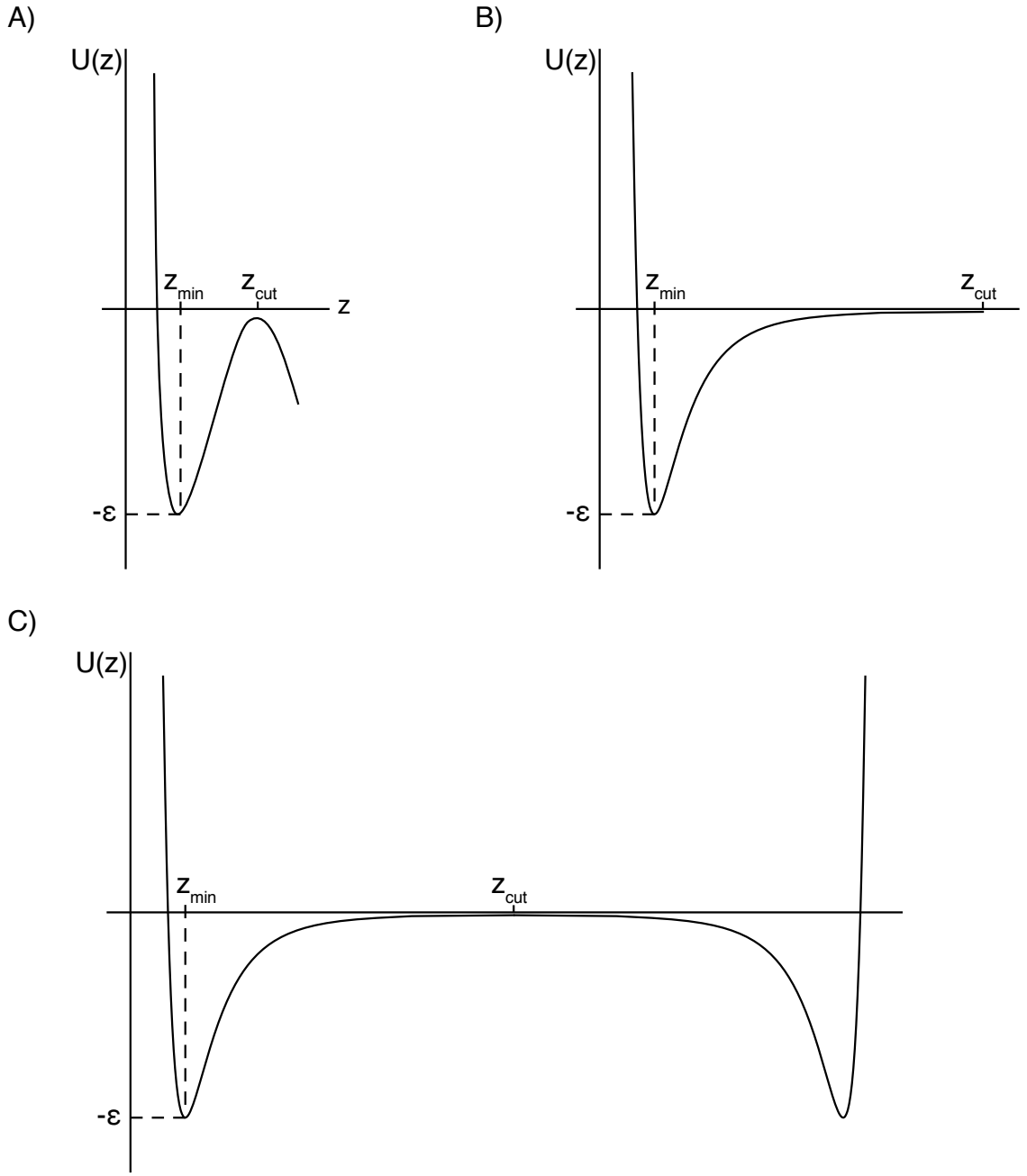

Figure 4.1: Schematic of potential curves wherein a Brownian particle is trapped. A) A potential with both a minimum, z_min, and a local maximum, z_{cut}. B) A Lennard-Jones potential with a minimum, z_min, where z_{cut} is set at some arbitrary position in the flat part of the potential. C) The same as 1B, except superposing a mirror image of the same potential shifted so that z_{cut} of the mirror potential is at the same position as z_{cut} of the original potential.

tances from its minimum, as shown in Fig. 4.1B. In this work we consider the 12-6 Lennard-Jones flat wall potential commonly used in HOOMD-blue, LAMMPS, and other simulation packages:

$$U_{LJ}(z) = \begin{cases} 4\varepsilon\left[(\frac{\sigma}{z})^{12} - (\frac{\sigma}{z})^{6}\right] & z < z_{cut} \\ 0 & z \geq z_{cut} \end{cases} \tag{4.3}$$

Where in our Langevin and Brownian simulations we take $z_{cut} = 2.5a$, $\sigma = 1.0a$, and the potential is slightly shifted vertically so that the it smoothly goes to zero at $z_{cut} = 2.5a$. We are interested in τ_{esc}, the mean time for a particle to travel from the bottom of the potential well, $z_{min} = 2^{1/6}$ a to z_{cut}. All simulations here are performed using the HOOMD-blue Langevin and Brownian integrators in the NVT ensemble.

The one comprehensive paper that explicitly considers the LJ case is that of Larson and Lightfoot (LL), whose solution method is specialized for escape at some arbitrary, relatively large, distance from the local minimum in the LJ potential, which then sets the cut-off value z_{cut} of the potential[61]. While Larson and Lightfoot solved the Fokker-Planck equation for the LJ potential, they did so under the approximation that energy uptake from the heat bath is not limiting, which is not valid for "very small" values of α, as noted above. However, the Kramers and Mel'nikov-Meshkov solutions, while not valid for the LJ potential in the overdamped limit, should become accurate for this potential at small enough α, where only the shape of the potential well around z_min is relevant. Therefore, to solve the problem of escape of a particle from an LJ potential in the overdamped limit, the little-known LL solution is necessary, while to solve the escape problem outside of this limit, and to determine the transitions between the different limits, the Kramers and especially the MM solutions are necessary. Our goal is to provide valid solutions for the escape time in each limit for the LJ potential, to define the conditions necessary for each limit to apply, and to provide a cross-over formula that would allow one to bridge between the limits. This includes defining the ranges of α and of ε/k_BT that distinguish between "small" and of "very small" α, where in the latter case the escape time is set by the rate of energy uptake from the heat bath.

4.3.1 Overdamped particle

We first consider the overdamped regime, where the diffusive behavior of the particle near z_{cut} is dominant. Larson and Lightfoot present two approaches for calculating the escape rate of a particle from a Lennard-Jones well in the overdamped regime. The first is in the overdamped limit, using the Smoluchowski equation, which is valid for $t_{in} \to 0$, or $\alpha \to \infty$.

$$\tau_{esc} = \tau_0 \Big(\frac{\pi k_B T}{\varepsilon}\Big)^{1/2} \frac{\frac{z_{cut}}{a} - (\frac{4\varepsilon}{k_B T})^{1/n} \Gamma(1 - \frac{1}{n})}{n 2^{1/n}} e^{\varepsilon / k_B T} \tag{4.4}$$

Here the dimensional escape time is τ_{esc}/τ_0, and $n = 6$ is the exponent in the 12-6 LJ potential.

Larson and Lightfoot carried out "exact" calculations confirming these expressions for $z_{cut} = 10a$, which is considerably larger than the more practical and frequently used cutoff value of $2.5a$, where the potential is already quite flat. Therefore, we wish to assess the accuracy of the LL theory for a range for cutoff values from $2.5a$ to $10a$.

Kramers offers a well-known theory for the escape time of a moderately underdamped to overdamped Brownian particle from a 1-D potential well with upward curved harmonic shape at the bottom and downward harmonic at the top, as shown in Fig 1A. The predicted result depends on the curvatures of the potential at both bottom and top. Near the bottom of the well at z = zmin, the harmonic is defined by[71]:

$$U(z) = -\varepsilon + \frac{1}{2} k (z - z_{min})^2 = -\varepsilon + \frac{1}{2} m \Omega^2 (z - z_{min})^2 \tag{4.5}$$

where ε is the well depth, and k is a "spring" constant defining the curvature at the bottom of the well. For a particle of mass m, in the above equation we express the constant, k, in terms of a characteristic oscillation frequency Ω as $k = m\Omega^2$, where Ω is the frequency of oscillation of the particle in the well in the underdamped limit where friction is negligible. Similarly, near the top of

the well at $z = z_{cut}$, we write

$$U(z) = -\frac{1}{2}k'(z - z_{cut})^2 = -\frac{1}{2}m\Omega^2(z - z_{cut})^2 \tag{4.6}$$

where k' is the magnitude of the curvature around z_{cut}. Expressed in terms of these characteristic frequencies, Kramers' expression for the escape time is

$$\tau_{esc} = \frac{2\pi}{\Omega}\frac{1}{\left[\sqrt{1 + \frac{1}{4\omega^2 t_{in}^2}} - \frac{1}{2\omega t_{in}}\right]}e^{k_B T} \tag{4.7}$$

For $\frac{1}{2\omega} \gg t_{in}$, which is the overdamped limit, Eq. 7 can be approximated as:

$$\tau_{esc} = \frac{2\pi}{\Omega\omega}\frac{1}{t_{in}}e^{k_B T} = \frac{2\pi}{\sqrt{k'k}}\zeta e^{\varepsilon/k_B T} \tag{4.8}$$

Eq. 8 is widely known and used in the overdamped regime, where the escape time depends only on the bead drag coefficient, ζ, and not on the bead mass.

To attempt to apply Eq. 7 to a potential such as the LJ potential that does not have a negative (downward) curvature at the point of escape, we can artificially create such a region by adding to the original potential a mirror reflection of the Lennard-Jones potential around z_{cut} so that we may define z_{cut} as a local maximum, as shown in Fig.4.1C [61]:

$$U_{LJ,m} = 4\epsilon\Big[\Big(\frac{\sigma}{z}\Big)^{12} - \Big(\frac{\sigma}{z}\Big)^{6} + \Big(\frac{\sigma}{2z_{cut} - z}\Big)^{12} - \Big(\frac{\sigma}{2z_{cut} - z}\Big)^{6}\Big] \tag{4.9}$$

We then can use a Taylor expansion to approximate $U_{LJ,m}(z)$ around z_{min} as

$$U_{LJ,m}(z) \approx -\varepsilon + \frac{1}{2}57.15\varepsilon\Big(\frac{z - z_{min}}{a}\Big)^2 \tag{4.10}$$

so long as $\left(\frac{z_{min}}{z_{cut}}\right)^7 \ll 1$. Expanding $U_{LJ,m}(z)$ around z_{cut} gives

$$U_{LJ,m}(z) \approx 2 \times 4\varepsilon\Big[\big(\frac{\sigma}{z_{cut}}\big)^{12} - \big(\frac{\sigma}{z_{cut}}\big)^{6}\Big] + \frac{1}{2} \times 2 \times 4\varepsilon\Big[\frac{156\sigma^{12}}{z_{cut}^{14}} - \frac{42\sigma^{6}}{z_{cut}^{8}}\Big](z - z_{cut})^2 \tag{4.11}$$

The first term amounts to approximately -0.033ε at $z_{cut} = 2.5\sigma$ and decreases for larger z_{cut} values, and thus can be neglected. Thus, only the quadratic term required by Kramers' theory remains. Therefore, the mirrored LJ potential is approximated near z_{cut} as

$$U_{LJ,m}(z) \approx \frac{1}{2}8\varepsilon\Big[\frac{156\sigma^{12}}{z_{cut}^{14}} - \frac{42\sigma^{6}}{z_{cut}^{8}}\Big](z - z_{cut})^2 \tag{4.12}$$

Comparing Eq. 5 with Eq. 10 and Eq. 6 with Eq. 12, we find that for the mirrored Lennard-Jones potential:

$$m\Omega^2 = k = 57.15\frac{\varepsilon}{a} \tag{4.13}$$

$$m\omega^2 = k' = -8\varepsilon\Big[\frac{156\sigma^{12}}{z_{cut}^{14}} - \frac{42\sigma^{6}}{z_{cut}^{8}}\Big](z - z_{cut})^2 \tag{4.14}$$

where for $z_{cut} = 2.5a$, $m\Omega^2 = 0.22\varepsilon$.

4.3.2 Underdamped particle

We now will consider the case of an underdamped particle escaping a Lennard-Jones potential well. Kramers' presented a solution for a particle in the underdamped limit, which assumes that the rate limiting step is energy uptake from the heat bath:

$$\tau_{esc} = \frac{2\pi}{\Omega}\frac{t_{in}}{S_1}e^{k_B T} \tag{4.15}$$

Here S_1 is the "action" per oscillation cycle of the particle, defined as

$$S_1 = 2\int_{1a}^{z_{cut}} \sqrt{-2mU_{LJ}(z)}dz \tag{4.16}$$

We obtain S_1 by numerical integration of Eq. 16 using N-point quadrature with a spacing of $h = 0.025a$, thus taking the entire shape of the potential-well into account. Eq. 15 can be used to calculate the escape time for given values of $\{t_{in}, m \text{ and } \varepsilon\}$ using relationships established above (Eqs. 9-11 and 13-14).

The prediction of Eq. 15 is shown in Fig.4.2 by the dot-dashed lines for small values of α, and Eq. 7 (which converges to Eq. 8 at high α) is shown by solid lines for large values of α. Mel'nikov and Meshkov (MM) proposed a solution to Kramers problem for all damping regimes, which spans Kramers' two limits (although does not account for the flatness of the LJ potential near the point of escape) and is shown by the dotted lines in Fig.4.2A. The MM result, given by Eq. 17, is a more generalized form that encompasses Kramers' Eqs. 7, 8, and 15, and includes the prefactor $1/A(\Delta)$, which accounts for the coupling of the particle to the heat bath[72].

$$\tau_{esc} = \frac{2\pi}{\Omega} \frac{1}{\left[\sqrt{1 + \frac{1}{4\omega^2 t_{in}^2}} - \frac{1}{2\omega t_{in}}\right]} \frac{1}{A(\Delta)} e^{k_B T} \tag{4.17}$$

where

$$\Delta = \frac{S_1}{t_{in} k_B T} \tag{4.18}$$

The function $A(\Delta)$ covering all damping regimes is given by:

$$A(\Delta) = \exp\left[-\sum_{n=1}^{\infty} n^{-1} erfc\left[\frac{\sqrt{n\Delta}}{2}\right]\right] \tag{4.19}$$

Where the sum in Eq. 19 converges within n = 200 for all the cases studied in this work.

This result derived by Mel'nikov and Meshkov (MM) was originally presented as a solution for a potential with harmonic bottom and harmonic top for all damping regimes. However, it can be seen that both the MM and Kramers' solutions fail in the high-α regime, since the harmonic assumption is a poor approximation for the shape of a LJ well near z_{cut}. Thus, we will see that a complete solution to the escape problem for an LJ potential over all friction regimes requires splicing a low-α solution with the LL solution at high α.

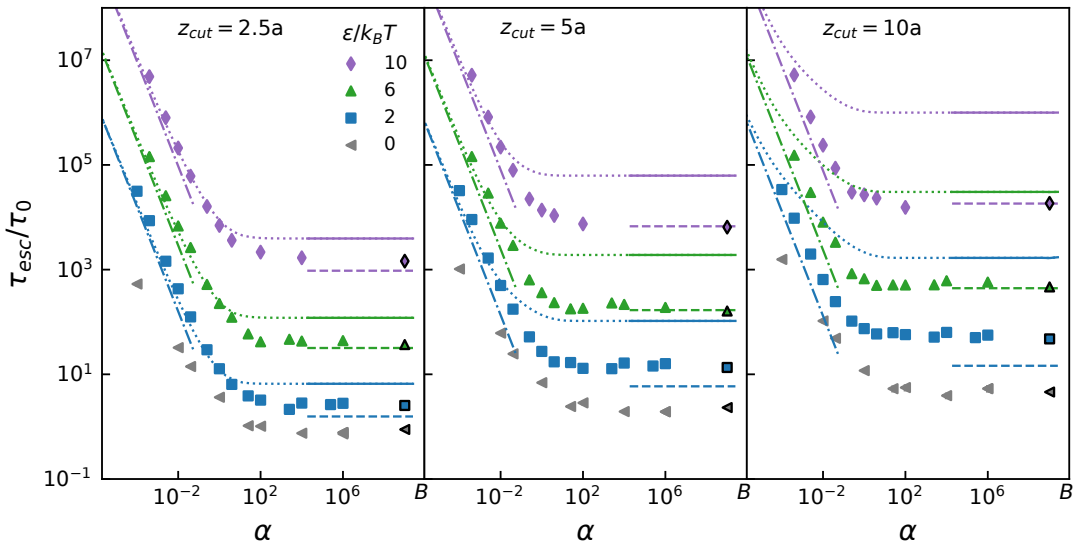

Figure 4.2: Symbols represent simulation results for escape of a particle from the LJ potential given in Eq. 3 using HOOMD-blue's Langevin integrator and are the same in each sub-figure. Symbols outlined in black on the far right of each sub-figure are from simulations using HOOMD-blue's Brownian integrator (denoted on the x axis by "B"). A) Dot-dashed lines represent Kramers' theory for an underdamped particle (Eq. 15), solid lines represent Kramers' theory for an overdamped particle (Eq. 7), and the dotted lines represent Mel'nikov-Meshkov theory for all damping regimes (Eq. 17). Dashed lines represent the high friction limit of Larson and Lightfoot (Eq. 4). Line and symbol color designates a given value of ε/k_BT, shown in the legend. There are no lines corresponding to free diffusion, for which $\varepsilon/k_BT = 0$, for which simulation results are denoted by grey symbols.

4.3.3 Scaling behavior and solution for all damping regimes

From the LL (Eq. 4), Kramers (Eq. 7 and 8), and MM (Eq. 17) solutions, we can determine scaling laws for the dimensionless escape time τ_{esc}/τ_0 in the overdamped and underdamped limits. In both limits, the dimensionless escape time is proportional to $\exp(\varepsilon/k_BT)$, with a prefactor of order unity in the overdamped limit.

In the underdamped limit ($\alpha \to 0$, or $t_{in} \to \infty$), the escape time τ_{esc} from Kramers "general" theory, Eq. 7, and from LL's theory for the underdamped case, approach the scaling of the activated complex theory [61], wherein the prefactor is proportional to the inverse of the oscillation frequency Ω in the potential well, and therefore scales as $a\sqrt{m/\varepsilon}$, which is independent of the

drag coefficient ζ. The normalized escape time τ_{esc}/τ_0, recalling that $\tau_0 \equiv \frac{\zeta a^2}{k_B T}$, therefore has a prefactor that scales as $a\sqrt{\frac{m}{\varepsilon}}/\frac{\zeta a^2}{k_B T} = \sqrt{\frac{k_B T}{\varepsilon}}\alpha^{-1/2}$. It thus scales as the inverse square root of α. As discussed above, however, this result fails in the limit of $\alpha \to 0$, because of lack of equilibrium with the heat bath, which requires the presence of friction because of the fluctuation-dissipation theorem. Reducing friction allows one to approach the regime in which activated complex theory is valid, but one cannot reach this theory at asymptotically small α, because equilibration with the heat bath is lost as $\alpha \to 0$. Kramers therefore provided a separate equation for this limit, whose results are given by the dot-dashed line in Fig.4.2, but only the MM theory bridges to this result continuously as $\alpha \to 0$.

The MM theory in the $\alpha \to 0$ limit therefore differs from Kramers "general" theory, Eq. 7, by the additional factor of$A(\Delta)$ (Eq.19) in the denominator, where Δ scales as $a\sqrt{\frac{\varepsilon}{m}}\frac{\zeta}{k_B T}$. Thus, the low-$\alpha$ behavior of the MM solution depends on the scaling of $A(\Delta)$ with Δ at low Δ. Mel'nikov and Meshkov report that $A(\Delta) \approx \Delta - 0.82\Delta^{3/2}$ at low α, which we can approximate by $A(\Delta) \approx \Delta$ in the asymptotic limit. We thus find that $\tau_{esc}/\tau_0 \sim (a\sqrt{\frac{m}{\varepsilon}})/(\frac{\zeta a^2}{k_B T}\Delta)\exp[\frac{\varepsilon}{k_B T}]$, which is $\tau_{esc}/\tau_0 \sim (\frac{k_B T}{\varepsilon})\alpha^{-1}\exp[\frac{\varepsilon}{k_B T}]$, where there is scaling of dimensionless escape time with α^{-1}, rather than $\alpha^{-1/2}$. This scaling of α^{-1} at low α is consistent with the observed scaling of the MM theory, the Kramers $\alpha \to 0$ limit (Eq. 15), and the Langevin simulations, as seen in Fig.4.2. In dimensional terms, in the underdamped limit, $\tau_{esc} \sim \frac{m}{\zeta}\frac{k_B T}{\varepsilon}$, where $\frac{m}{\zeta}$ is the inertial time, and the escape time is inversely proportional to the drag coefficient ζ , while in the overdamped limit $\tau_{esc} \sim \frac{\zeta a^2}{k_B T}\exp[\frac{\varepsilon}{k_B T}]$ it is proportional to ζ. In between these, in the activated complex theory pseudo-limit, $\tau_{esc} \sim a\sqrt{m/\varepsilon}\exp[\frac{\varepsilon}{k_B T}]$, which is independent of ζ.

When the escape time is scaled by the frictional time τ_0, the prefactor of $\exp(\varepsilon/k_B T)$ from the LL equation for the overdamped limit (Eq. 4) is independent of α and that from Kramers' equation for an underdamped particle (Eq. 15) in the limit of small alpha is proportional to α^{-1}. Combining these two regimes into a cross-over formula gives (Eq. 22). The prefactor of $\exp(\varepsilon/k_B T)$ in the overdamped limit, $B_{LL}(\varepsilon/k_B T)$, is constant with respect to α, while the prefactor of $\alpha^{-1}\exp(\varepsilon/k_B T)$ in the underdamped limit, $B_K(\varepsilon/k_B T)$ is a constant with respect to α

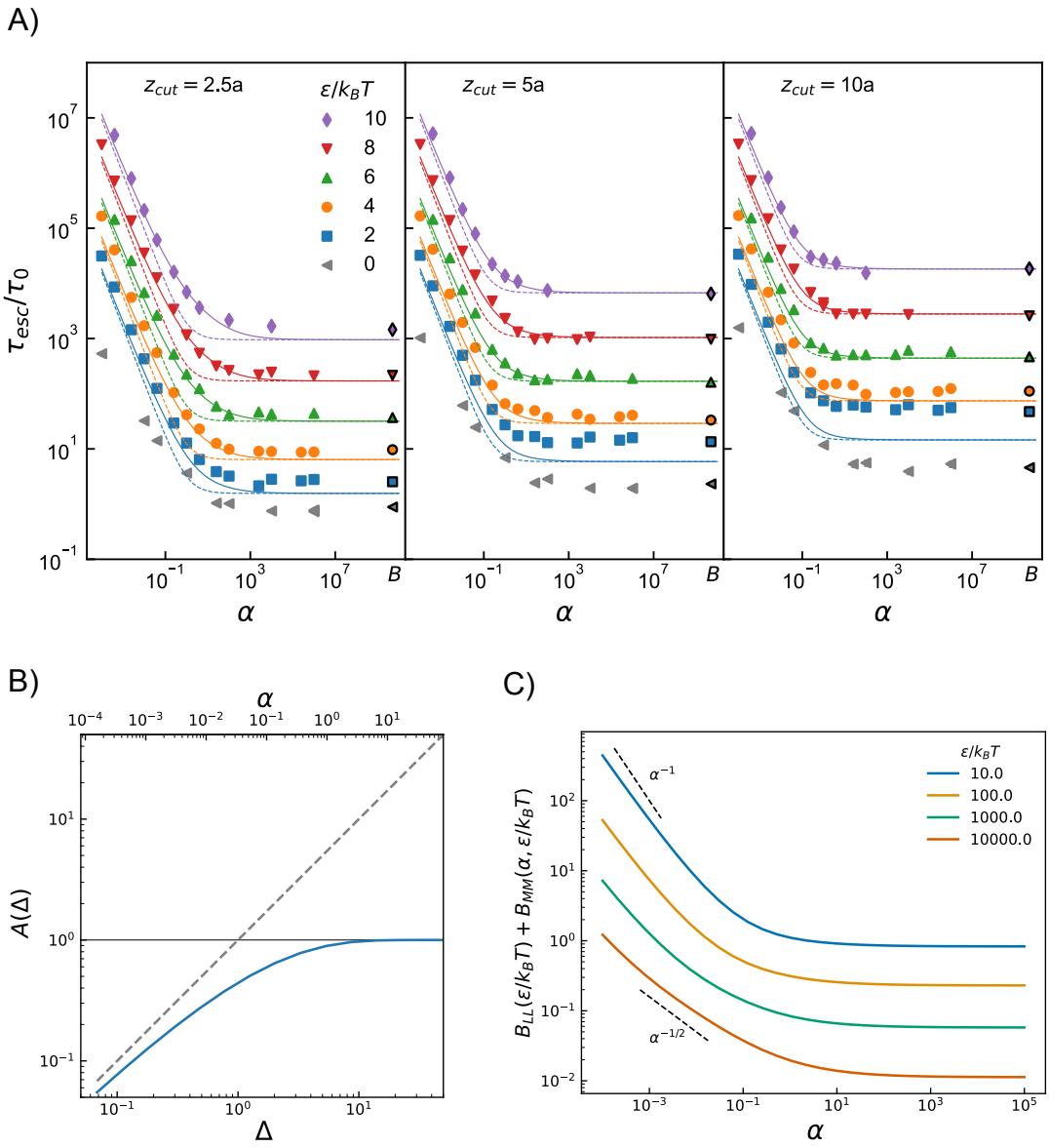

Figure 4.3: A) All symbols are the same as in Fig.4.2. Dashed lines represent Eq. 22, using $B_K(\varepsilon/k_BT)$, and solid lines represent the theory presented in Eq. 24, using $B_MM(\alpha, \varepsilon/k_BT)$. B) Blue line: $A(\Delta)$ as given in Eq. 19 and grey dashed line: $A(\Delta) = \Delta$, both for $\varepsilon = 8k_BT$, $z_{cut} = 2.5a$. C) Prefactor from Eq. 24 for where $z_{cut} = 10a$. Black dotted lines indicate scaling for α^{-1} and $\alpha^{-1/2}$, as indicated on the plot.

from Kramers' Eq. 15. Thus,

$$B_{LL}(\varepsilon/k_BT) = (\frac{\pi k_BT}{\varepsilon})^{1/2} \frac{\frac{z_{cut}}{a} - (\frac{4\varepsilon}{k_BT})^{1/n}\Gamma(1-\frac{1}{n})}{n2^{1/n}} \tag{4.20}$$

$$B_K(\varepsilon/k_BT) = \frac{\pi a k_BT}{\sqrt{2}\sqrt{57.15\varepsilon}} \frac{1}{\int_{1a}^{z_{cut}} \sqrt{-2mU_{LJ}(z)}dz} \tag{4.21}$$

$$\tau_{esc}/\tau_0 = \Big(B_{LL}(\varepsilon/k_BT) + \frac{B_K(\varepsilon/k_BT)}{\alpha}\Big)e^{\varepsilon/k_BT} \tag{4.22}$$

The prediction of Eq. 22 is shown as dashed lines in Fig.4.3A. This result reaches the correct asymptotes for high and very low α, but does not capture the transition between the two accurately and leaves out the activated complex theory pseudo limit which influences the behavior at intermediate α. The reason for this deviation in the region of moderately small α is that while the assumption that $A(\Delta) = \Delta$ holds true in the underdamped limit, this limit is not reached until α is very small, as shown in Fig.4.3B. For a more accurate solution, which also captures the activated complex theory pseudo-limit, we can keep the exact form of the $A(\Delta)$ correction factor in the denominator, thus using the prefactor from Mel'nikov and Meshkov's approach in Eq. 10. In this case, the prefactor of e^{ε/k_BT}, which is $B_{MM}(\alpha, \varepsilon/k_BT)$, is not independent of α, but still scales as α^{-1} in the limit of very small α. That is,

$$B_{MM}(\alpha, \varepsilon/k_BT) = \frac{2\pi}{\Omega}\frac{1}{A(\Delta)\tau_0} \tag{4.23}$$

The form of the general equation is then

$$\tau_{esc}/\tau_0 = (B_{LL}(\varepsilon/k_BT) + B_{MM}(\alpha, \varepsilon/k_BT))e^{k_BT} \tag{4.24}$$

whose predictions, shown by the solid lines in Fig.4.3A, are in much better agreement with the simulation data than are those from Eq. 22, given by the dashed lines in Fig.4.3A. Eq. 24 is

therefore the most complete solution for this case of escape from a Lennard-Jones potential for arbitrary damping.

This solution also allows us to distinguish within the underdamped regime the conditions for which the rate of energy uptake from the heat bath is limiting (i.e., "very small" α) from those for which it is not limiting. To do so, we plot in Fig.4.3C the prefactor of Eq. 24, namely $B_{LL}(\varepsilon/k_BT) + B_{MM}(\alpha, \varepsilon/k_BT)$ against α for various values of ε/k_BT, noting that a clear regime in which the prefactor scales as $\alpha^{-1/2}$ appears only for very high ε/k_BT, around 10,000 or higher. For smaller ε/k_BT, the rate of energy uptake from the heat bath is not limiting only when α is high enough to be out of the underdamped limit, and on the way towards overdamping. Only for very high $\varepsilon/k_BT \geq 10,000$, there is a clear $\alpha^{-1/2}$ underdamped scaling regime between "very small" α (with scaling α^{-1}) and the overdamped regime. The huge value of ε/k_BT required to obtain this regime, and the exponential dependence of escape time on ε/k_BT, imply that this intermediate regime, described by the "Activated Complex Theory" (ACT), for which the escape time is independent of the drag coefficient, is therefore essentially always a rough approximation.

4.4 Example Problem: Colloid-Polymer Mixtures

Here we demonstrate the relevance of these considerations by noting the need for a correction to Wang and Larson's recent report of Langevin dynamics simulations of the multiple relaxation modes displayed in an aqueous suspension of colloidal particles of radii $R = 10a$ or $R = 25a$ and telechelic polymers [22]. The telechelic polymers were modeled by dumbbells, with each bead able to bind to the surface of a colloid, where binding was controlled by an attractive potential well bounding the surface of each colloid. This potential well allowed the formation of polymer loops on a single colloid particle when both beads of a dumbbell were bound to the same colloid, or of bridges between neighboring particles, when the two beads were bound to different colloids[22]. The fastest relaxation times in the simulations involved diffusion of a polymer loops across the surface of the particle, while a slower relaxation process was the breakage of a bridge by escape of

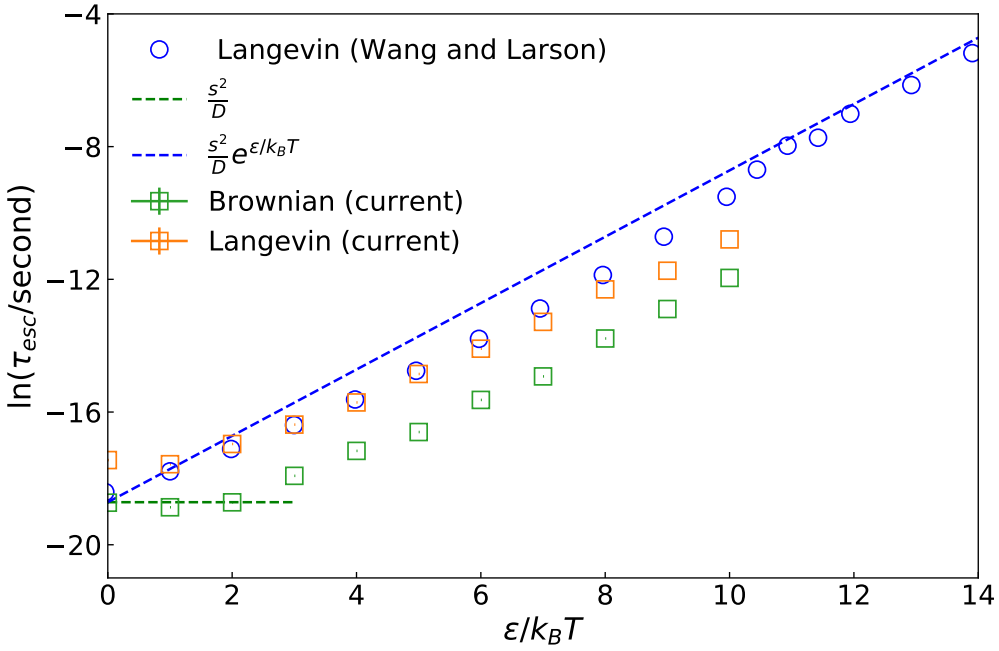

Figure 4.4: Wang and Larson's times of escape, τ_{esc}, of a particle of drag coefficient ζ and diffusivity $D = k_BT/\zeta$ from a potential well of depth ε calculated from Langevin dynamics using LAMMPS (blue circles) compared with escape times from Brownian dynamics (green squares) and Langevin dynamics (orange squares) using HOOMD-blue. Simulations are averages of escape times over 100 stickers, initialized on the surface of a colloidal particle with diameter $D_{colloid} = 20a$, as described in the original paper. Predictions from Pham et al. [6] with and without a potential (blue and green dashed lines) are included for $s = (r_c - r_m) = 1.38a$. Parameters used in these simulations: time step $\Delta t = 0.001\tau_R$, mass $m = 1.0m_0$, and drag coefficient $\zeta = 1.0m_0/\tau_R$.

one of the beads from the colloid surface. The colloid radius was large enough that the diffusion of the loop over the surface of the particle was able to reach the overdamped regime over the time required for chain relaxation, as demonstrated by changing the dumbbell bead friction. Wang and Larson naively assumed that all slower relaxation processes would then also be overdamped using the same Langevin simulator, including the relaxation involving breakage of the bridge.

However, as is evident from our simulations and our above discussion, the slow escape of the bead from a narrow potential binding a dumbbell bead to the colloid can be underdamped even when a faster free diffusion of the same particle is overdamped. Fig.4.4 shows a correction to Wang and Larson's Fig.5, including the original data from Wang and Larson (blue symbols) along

with our replication of the study using HOOMD-blue's Langevin and Brownian integrators (orange and green square symbols, respectively) Our simulations here thus show that the particles' escape from the LJ potential was not overdamped in Wang and Larson's paper, and as a result, the bridge breakage process proved to be outside of the overdamped regime, despite the much faster loop diffusion process being overdamped.

As a result, as shown in Fig.4.5, the predicted results from Wang and Larson for the relaxation modulus of a network of colloids bridged by dumbbells is sensitive to the dimensionless inertial time t_{in}/τ_R down to values of around 10^{-2} rather than reaching convergence at unity, as was naively assumed by Wang and Larson.

The slow bridge breakage was not in the overdamped regime even while the fast loop diffusion was overdamped because the width of the potential well binding the bead was less than the distance of free diffusion required for loops relaxation. This can be anticipated by the results in Fig.4.3, by noting that the transition from underdamped to overdamped behavior is only completed when α

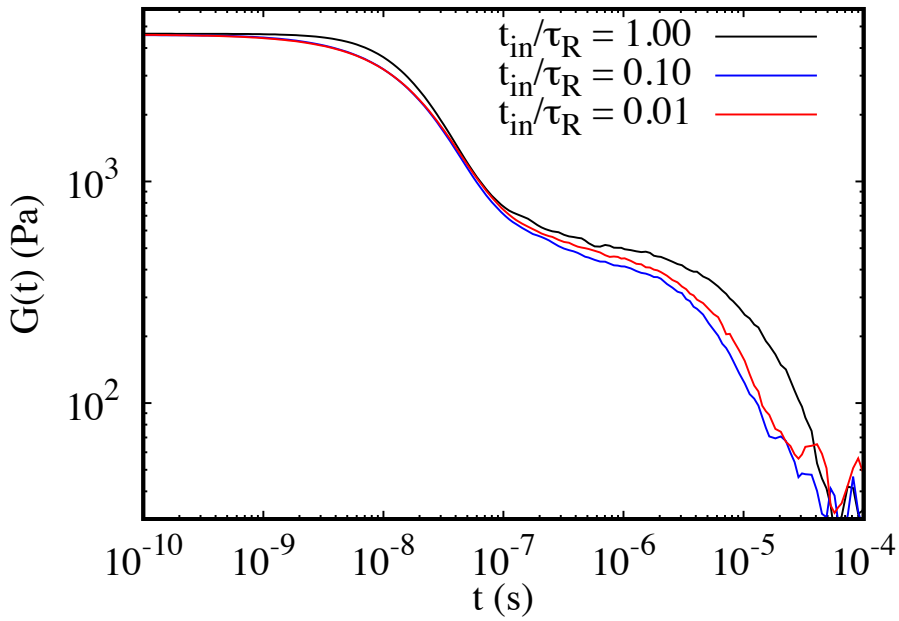

Figure 4.5: Effect of dimensionless inertial time t_{in} on relaxation modulus computed by Langevin simulations, for the problem described in Fig. 4 of Wang and Larson. In the Wang-Larson paper, t_{in}/τ_R was taken to be 1.0, which is outside of the overdamped limit, as shown by its effect on the result.

reaches approximately $10^2 - 10^3$, regardless of the well depth, or even the presence of a potential, as shown by the grey symbols for $\varepsilon = 0$. For free diffusion over the surface of the particle, the relevant length scale is comparable to the colloid radius, and the length scale a in the expression $\alpha \equiv \frac{\zeta^2 a^2}{mK_BT}$ shown be taken as the colloid radius R, while for escape from the potential well, a is the well width, which was an order of magnitude or more smaller than R. Thus, the relevant value of α was high enough to attain the overdamped limit for free diffusion, but too low to attain this limit for the much slower escape from the potential well. Failing to consider the appropriate condition for attaining the overdamped regime when a conservative force was present, Wang and Larson unwittingly presented results that were significantly affected by inertia.

Finally, we note that the combined formula for the escape time given above is valuable not only for determining conditions needed for reaching the overdamped regime in Langevin simulations, but also gives a good estimate of the escape time in situations where a good estimate of the escape time is needed. An example is the case of mesoscale population-balance simulations in which the polymers are included only implicitly and rates of breakage and formation of bridges must be given by explicit formulas[10].

4.5 Conclusions

In Langevin simulations of systems with multiple relaxation processes, especially those involving escape from potential wells, attainment of the overdamped regime requires careful attention to the dimensionless damping coefficient,α. We assessed the validity of theories from Kramers, Mel'nikov and Meshkov (MM), and Larson and Lightfoot (LL) for all damping regimes by comparison to Langevin dynamics simulations of a particle escaping from a 12-6 Lennard-Jones potential. We demonstrate that the standard Kramers theory is not accurate for a Lennard-Jones potential in the underdamped regime because it does not account for the coupling of the particle to the heat bath, and in the overdamped regime because it does not apply to a potential that becomes flat near the escape condition, as is the case for the LJ potential. Because MM theory is accurate in the un-

derdamped regime for an arbitrary potential, and LL theory is accurate in the overdamped regime for the LJ potential, we determine prefactors from each of these approaches that allow presentation of a general equation for arbitrary damping for escape from an LJ potential well. This general theory also shows that the validity of the Activated Complex Theory is limited to extraordinarily high values of the dimensionless well depth.

CHAPTER 5

Improving the Efficiency and Accuracy of Population Balance Brownian Dynamics

5.1 Introduction and Background

The ultimate goal of the prior three chapters is to inform the Population Balance Brownian Dynamics model such that we can simulate experimental systems for run times on the order of seconds. However, Pop-BD was initially developed as a proof-of-concept, and therefore was only used for small system sizes due to its computational inefficiencies[10]. The original population balance Brownian dynamics (Pop-BD) method was developed to capture the behavior of the polymer-colloid system at long time scales by treating all telechelic polymer chains as phantom springs that connect colloidal particles by their centers of mass [10]. It is a coarse-grained model informed and validated by a model that uses LAMMPS to resolve the polymer chains as FENE dumbbells (referred to from here on as the "FENE BD" model) that can migrate on the surface of the colloids, which has been shown to capture four distinct relaxation modes in polymer-colloid mixtures [22].

5.1.1 Overview of Population Balance Brownian Dynamics

The full details of Pop-BD can be found in the work by Hajizadeh and Larson, but the key model components are as follows. Colloidal particles are represtented as Weeks-Chandler-Anderson repulsive spheres, which assumes the colloids are bare and does not account for polymer-mediated

interactions. All polymer chains are implicit and accounted for by a $N_{colloid} \times N_{colloid}$ matrix, where the diagonal matrix component represents the number of loops on the N^{th} colloid, and the off-axis components represent the number of bridges between the i^{th} and j^{th} colloids. Two equations, based on the work of Tripathi and coworkers, describe the bridge-to-loop and loop-to-bridge transition rates [55]. The loop-to-bridge transition rate rate, $L(d_{ij})$ is defined as

$$L(d_{ij}) = \Omega \exp\big[-\frac{1}{k_B T}(\Delta G + U_S(d_{ij} - r_c))\big] \tag{5.1}$$

and the bridge-to-loop transition rate, $M(d_{ij})$ is defined as

$$M(d_{ij}) = \Omega \exp\big[-\frac{1}{k_B T}(\Delta G - U_S(d_{ij}) + U_S(d_{ij} - r_c))\big] \tag{5.2}$$

where Ω is the thermal fluctuation frequency, ΔG is well depth of the attraction potential, r_c is the width of the potential well, and the spring potential $U_s(d)$ is equivalent to U_{FENE} described in the FENE-BD model.

To account for the geometric restrictions the colloid curvature imposes on the loop/bridge transition rates, an "effective cap fraction" S_{cap}/S_{sphere} is defined as the ratio of the area accessible to a polymer for bridge formation normalized by the total surface area of the colloid. The area S_{cap} is determined using a Metropolis scheme, the details of which can be seen in the paper by Hajizadeh et al.[10]

The bridge/loop transition rates determine the probability of a bridge forming or breaking at each times step. The probability of a loop-to-bridge transition at a single timestep is

$$p = L(d_{ij})\Delta t \tag{5.3}$$

and the probability of a bridge-to-loop transition is

$$q = M(d_{ij})\Delta t \tag{5.4}$$

Therefore, the probability of a single bridge forming between two particles i and j from the detachment of a loop on particle i is

$$P_{ij} = N_{ii}\frac{S_{cap}}{S_{sphere}}p(1-p)^{N_{ii}\frac{S_{cap}}{S_{sphere}}-1} \tag{5.5}$$

and the probability of a single loop forming on particle i or j from the breakage of a bridge between particles i and j is

$$Q_{ij} = N_{ij}q(1-q)^{N_{ij}-1} \tag{5.6}$$

Where N_{ii} is the number of loops on particle i and N_{ij} is the number of bridges between particles i and j.

At each time step, the following algorithm is applied to each pair of particles to update the number of bridges and loops on every particle in the system:

1. Compute P_{ij}, P_{ji}, and Q_{ij}
2. Generate uniformly distributed random numbers between 0 and 1:μ_1, μ_2, μ_3, and μ_4
3. If $\mu_1 < P_{ij}$: $N_{ii} -= 1$ and $N_{ij} += 1$
4. If $\mu_2 < P_{ij}$: $N_{jj} -= 1$ and $N_{ij} += 1$
5. If $\mu_3 < Q_{ij}$:
   (a) if $\mu_4 \leq 0.5$: $N_{ii} += 1$ and $N_{ij} -= 1$
   (b) if $\mu_4 > 0.5$: $N_{jj} += 1$ and $N_{ij} -= 1$
6. If $\mu_3 \geq Q_{ij}$: no change

The linear relaxation modulus can be determined from the stress tensor as follows:

$$G(t) = \frac{V}{k_B T}\langle S_{xy}(t)S_{xy}(0)\rangle \tag{5.7}$$

Where V is the system volume and the off-diagonal elements of the stress tensor S_{xy} follow the form of

$$S_{xy} = \frac{1}{V} \sum_{k} d_{k,x} F_{k,y} \tag{5.8}$$

where $d_{k,x}$ is the end-to-end vector of the polymer bridge along the x-axis, $F_{x,y}$ is the chain stretching force along the y-axis, and k iterates over all bridges between particle pairs in the system.

5.1.2 Limitations to Pop-BD and Proposed Solutions

There are two main limitations to Pop-BD's computational efficiency: 1) the autocorrelation method used to compute the stress-relaxation of the system is prohibitively slow, and 2) the original Pop-BD code was a home-grown code written without the optimizations of larger molecular dynamics software packages. This chapter will detail how we address both of these limitations by integrating both the Pop-BD algorithm and an on-the-fly correlation method into HOOMD-blue, an open-source simulation software. HOOMD-blue's user interface is a Python API, which allows for flexibility and customization, while its backend is written in C++ for performance advantages. In the first section, we incorporate an exisiting on-the-fly autocorrelation method into HOOMD-blue as a plug-in, or stand-alone code that is compiled alongside HOOMD. In the section section, we write Pop-BD as a custom 'integration method' that dyanmically adds and removes bonds between particles during runtime. We show that, with these two modifications, we are able to run Pop-BD simulations of sufficiently large system sizes for experimentally-relevant simulations times.

5.2 On-the-Fly Autocorrelation as a HOOMD-blue plug-in

Disclosure: This section includes material adapted from a final project report submitted for NERS 590: *Methods and Practice of Scientific Computing*, completed in collaboration with Alexander Adams, Chemical Engineering, University of Michigan, Ann Arbor, MI.

The FENE-BD model is executed using the LAMMPS package, which offers the option of implementing an on-the-fly autorcorrelation during the simulation run. When the LAMMPS BD

model was coarse-grained to Pop-BD, which is executed as a home-grown code written in C, the on-the-fly correlation functionality was not carried over. Even without the on-the-fly correlation, Pop-BD showed an improvement in run-time for systems with many particles. In this section, we show the benefit of integrating Likhtman's on-the-fly multi-tau correlation with HOOMD-blue, with the ultimate goal of running Pop-BD simulations in HOOMD-blue an autocorrelating its output during runtime.

As with most MD software, one can readily access system or per-particle data, such as volume, temperature, pressure (as a tensor), or particle velocities at each time step during a HOOMD simulation. To compute dynamic properties of the simulation, such as the complex modulus or diffusion coefficients, we process the system data with time correlation functions (hereon referred to as correlation functions) [74]. Many properties calculated from correlation functions rely on the fluctuation-dissipation theorem, which states that a system's response to spontaneous fluctuations within a system is equivalent to its response to small applied force. We take advantage of the fluctuation dissipation theorem and use correlation functions to compute relaxation and transport properties of physical systems. For example, we can autocorrelate the off-axis stress values to calculate the stress relaxation modulus of a system, or autocorrelate particle velocities to determine the related diffusion coefficients. The general form of an autocorrelation function, or a correlation of a property with itself over a delay, is:

$$R(t) = \frac{\sum_{i=1}^{N-\tau} (Y - \overline{Y})(Y_{i+\tau} - \overline{Y})}{\sum_{i=1}^{N} (Y_i - \overline{Y})^2} \tag{5.9}$$

where t is the time point for which the correlation is being performed, Y is the value of a given property at time i, τ is the lag time between measurements, and N is the total number of timesteps. The stress tensor of the system is defined as follows:

$$S_{xy} = \frac{1}{V} \sum d_{k,x} F_{k,y} \tag{5.10}$$

where d_k, x is the end-to-end vector of a chain along the x axis, and $F_{x,y}$ is the chain stretching force between two particles, and V is the volume of the system. The linear relaxation modulus is related to the stress tensor as

$$G(t) = \frac{V}{k_B T} \langle S_{xy}(t) S_{xy}(0) \rangle \tag{5.11}$$

The Likhtman Correlator Calculating correlation functions can require significant compute time and memory, especially if per-particle calculations are necessary. A large part of this overhead is the time and memory required to write all data points to an output file, reading the data into a correlator, then writing an equally large data file containing the correlated values. In 2010, the Likhtman group proposed an algorithm that uses block averaging and a multiple-tau correlation method to produce highly efficient and accurate calculations[74]. As data is correlated, the correlated values at short time scales accumulate redundant data which can be represented accurately as the average of a given time block. Ramirez and coworkers demonstrate that their algorithm maintains accuracy through the block averaging, and that the final amount of raw data produced is greatly reduced. They also use a multiple-tau method, which controls the ratio between the averaging time and and the lag time of the correlator. Parameters m and p are user defined as a way of controlling relative error, the smaller the ratio m/p is, the smaller the relative error. The recommended values (and default values in our implementation) are $m = 2$ and $p = 16$. This is crucial for calculations spanning very long time scales to reduce the memory and minimize error.

Autocorrelation is a computationally heavy process, with the number of operations required to calculate as single value scaling linearly with N. A typical simulation will run for 10^6 to 10^{10} time steps, and we often require autocorrelation functions for more than one value in each simulation. Additionally, a significant amount of the computation time is comprised of reading or writing values to or from a disk. Ramirez and coworkers presented a multiple tau correlation method that utilizes averaging and smoothing for more efficient computing, while also working "on-the-fly" to avoid the in/out bottleneck previously mentioned[74]. The general structure of the multiple-tau algorithm is as follows, but more detail is available in their paper[74].

- User-defined parameters: m, p, and S
- D_{ij} : array to store data (S+1 by p)
- C_{ij} : array to store correlation results (S+1 by p)
- N_{ij} : counter array for calculating averages (S+1 by p)
- A_i : accumulator (S+1)
- M_i: counter (S+1)

At each simulation time step, a new data value ω is sent to correlator level i, and the following algorithm takes place:

1. ω is stored at the first position of D, and all other data values are pushed up one value
2. The correlation array is updated as $C_{ij} = C_{ij} + D_{i0}D_{ij}$ and the correlation counter is incremented $N_{ij} = N_{ij} + 1$ (for maximum efficiency, this calculation iterates of j=0...p-1 at level 0 and j=p/m...p-1 for all other values)
3. w is added to the accumulator as $A_i = A_i + \omega$, and the counter is incremented as $M_i = M_i + 1$

When $M_i = m$, A_i/m is sent to the next level, $(i + 1)$, and A_i and M_i are reset to 0.

The Likhtman group provides their code as a standalone C++ package (hereon referred to as the Likhtman correlator) that can be used as a post-processing method. However, the algorithm is intended to be used during run time as an on the fly method to avoid the large memory and requirements of writing each data point into an external file, then reading the data into the correlator. Our goal is to bring this efficiency to the HOOMD-blue software package.

5.2.1 Software Design

Our design decisions while developing this plug-in were motivated by our conversations with HOOMD's lead developer, Joshua Anderson, Ph.D., and our own experiences as HOOMD users.

The ultimate goal is to develop a plug-in correlator that is simple and customizable. For simplicity, the only required arguments are the quantities to be correlated and the period at which to send values to the correlator; all other arguments are optional and set to default values if no argument is passed. A powerful tool within HOOMD is the ability to use a callback function, which allows the user to define a lamba function that is evaluated at every time step. We defined the `quantities` argument as a HOOMD vector string, which allows the user to pass callback functions to the correlator in the same way they would pass to a standard HOOMD logger. To implement this, the C++ **`Correlator`** class inherits from the Logger class. However, the Correlator directly inherits from the **`Analyzer`** class in Python, since **`Logger`** is not an HOOMD-defined Python class. This gives us all necessary functionalities because Logger inherits directly from **`Analyzer`**, so all inherited methods are preserved.

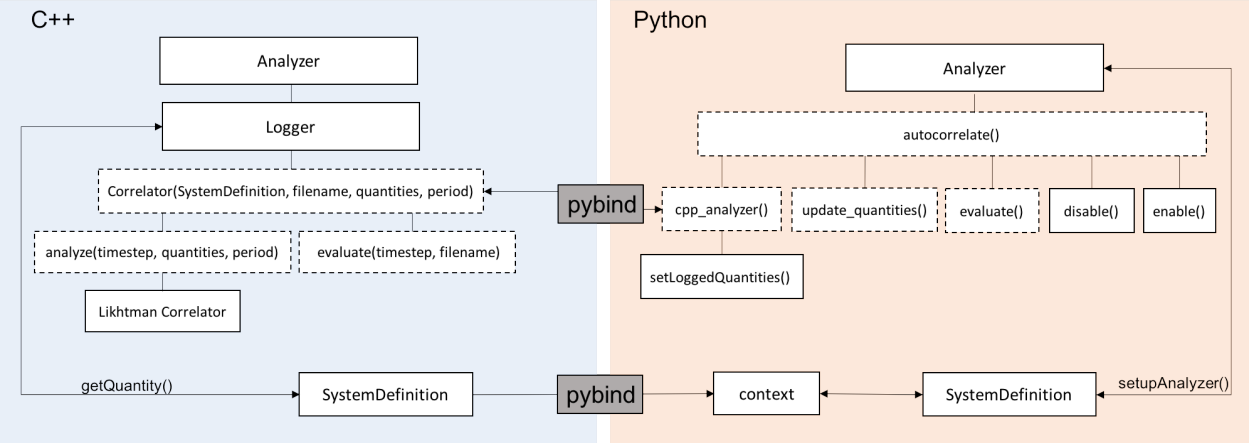

Figure 5.1: Schematic of HOOMD-blue plug-in architecture. Solid boxes indicate external code (HOOMD main code or the Likhtman Correlator), dashed boxes represent our plug-in. Lines represent inheritance, from top down. Arrows represent communication between components.

We integrated the Likhtman correlator into the architecture of HOOMD-blue, evaluated its accuracy and computational performance, and developed both user documentation and a developer guide. Figure 5.1 is a simplified diagram of HOOMD-blue's architecture and depicts how the plug-in is integrated into each level of the software. HOOMD is considerably larger and more complex than we were able to diagram, so we only show the relevant pieces of code that our plug-in directly inherits from or communicates with. HOOMD is a multi-language software package,

where the user interfaces with HOOMD through Python, but the back-end is written entirely in C++. HOOMD uses pybind to communicate between the Python and C++ levels. For this level of implementation, we provided the user with high-level options (file name, quantities to correlate, correlation and logging frequencies) but hard-coded the recommended algorithm parameters (m, p, S) into the C++ code.

Part of the inherent advantage of the Likhtman correlator is its separate functions for correlating and evaluating. During the correlating stage, no values are being actively written to a file, which saves overhead. The `evaulate()` call then iterates over the current data and writes it to a file. This means that the current state of the correlator can be written to a file at any given time step. This flexible output method is useful but must be used carefully. Dumping the data at every time step would defeat the purpose of the on-the-fly method, but writing the data exclusivley at the end of the run can be risky for very long simulations that may experience instabilities or exceed walltime. Therefore, by default we set the correlator to write the data at the end of the simulation, but also created the ”eval_period” parameter. The ”eval_period” allows the user to specify how frequently the correlator data is written to a file. This is recommended to be only a few times throughout the simulation, as a sort of ”safety,” or to allow the user to check in on the progress of their simulation in real time.

We also realize that it may be of interest to evaluate the correlator at specific points in a simulation, such as after volume or temperature are changed in connection with equilibration or other processes. To address this, users can call `correlate.evaluate()` at a specific line in their HOOMD code. The evaluate method is entirely independent from the primary correlator, but both methods access the same instance of LikhtmanCorrelator. This highlights the importance of our decision to define the instance of LikhtmanCorrelator as a class attribute, so that both methods can access the correlator.

5.2.2 Testing and Validation

We designed regression and unit tests to verify the functionality and efficacy of the plug-in as we continued to develop it. We test basic functionality such as intializing the correlator and creating the correct output file as simple unit tests. `TestValues` is a regression test that performs a short simulation and compares Correlator plug-in data to an already-verified post-processing workflow with the same data. Best-practice frameworks such as removing output from routine testing and use of variables are employed to assist with altering or expanding unit testing as further functionality is added.

The performance of the Likhtman algorithm is well studied in [74], which demonstrates that it is more accurate and efficient when compared with a standard single-tau correlator. Therefore, the purpose of our performance testing is not to demonstrate the performance of the algorithm, but to demonstrate accurate implementation and quantitatively compare the efficiency of the correlator plug-in with the correlator used as a post-processing method. The motivation for conducting this performance test is to ensure that our implementation is efficient in its method of communicating the simulation values to the correlator. It is possible, if the plug-in is poorly designed, that the on the fly method would be slower than the post-process method.

We chose a bead-spring network as our testing system because it is computationally inexpensive and we are familiar with its stress relaxation behavior from previous research. The network is composed of spheres connected by dumbbell springs, as seen in Figure 3a. The xy component of the pressure tensor matrix is the correlated property. All units are left as reduced units, since there is no physical relevance to the system and it is used simply for validation purposes.

5.2.3 Performance Testing

The same bead-spring network system used to validate the plug-in was also used for performance testing. The plug-in was tested by equilibrating the system, initializing the correlator, running for the given number of time steps, then evaluating the correlator. The post-processed correlation was tested by equilibrating the system, intializing a logger (a HOOMD method), then running for

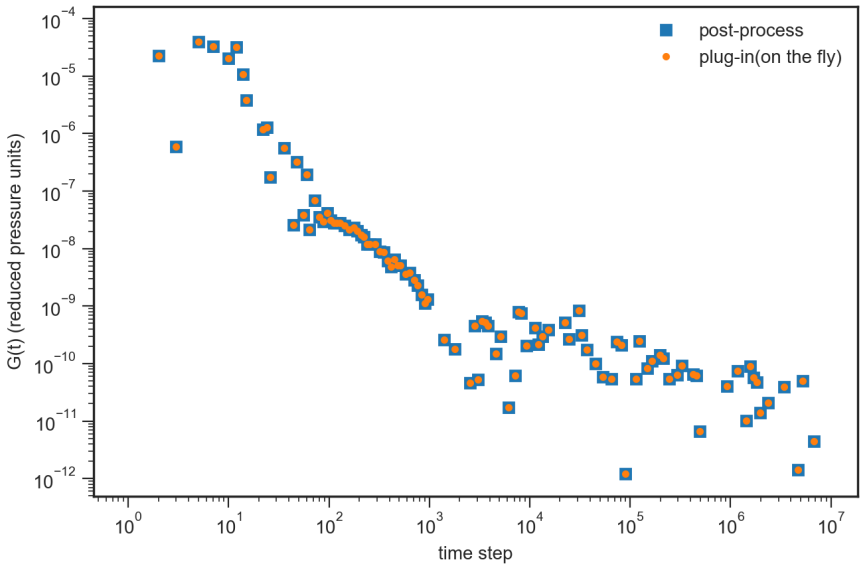

(a)

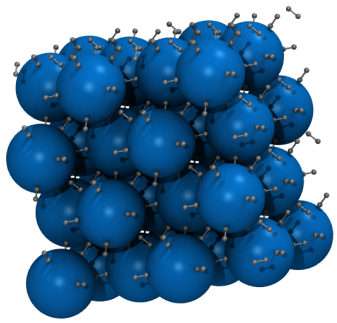

(b)

Figure 5.2: (a) Autocorrelation of xy component of pressure implemented on the fly and as a post-processing method. All units are reduced units. Both simulations were equilibrated for 1×10^5 time steps, then data was sent to the correlator every 10 time steps for 1×10^7 time steps (b) Visualization of the simulation initial configuration. Large spheres are initialized on a face centered cubic lattice and connected with nearest neighbors by harmonic spring dumbbells [7, 8]

.

the given number of time steps. The raw data from the logger was then formatted as a Likhtman correlator input script and passed to the Likhtman correlator. The results of this study, Figure 5.3, show that the plug-in is consistently more efficient than the post-processed implementation. Note that in unit testing validation both cases were run in a single simulation, but to assess the performance of the methods we ran the cases as entirely separate simulations.

Table 5.1: Run Time Analysis of On the Fly and Post-Processed Data

# time steps	**on the fly (sec.)**	**post-process (sec.)**	**seconds per time step**
1.00E+06	151	166	1.50E-05
5.00E+06	669	772	2.06E-05
1.00E+07	1330	1572	2.42E-05
5.00E+07	6497	8933	4.87E-05
1.00E+08	13446	15785	2.34E-05
		average	**2.64E-05**

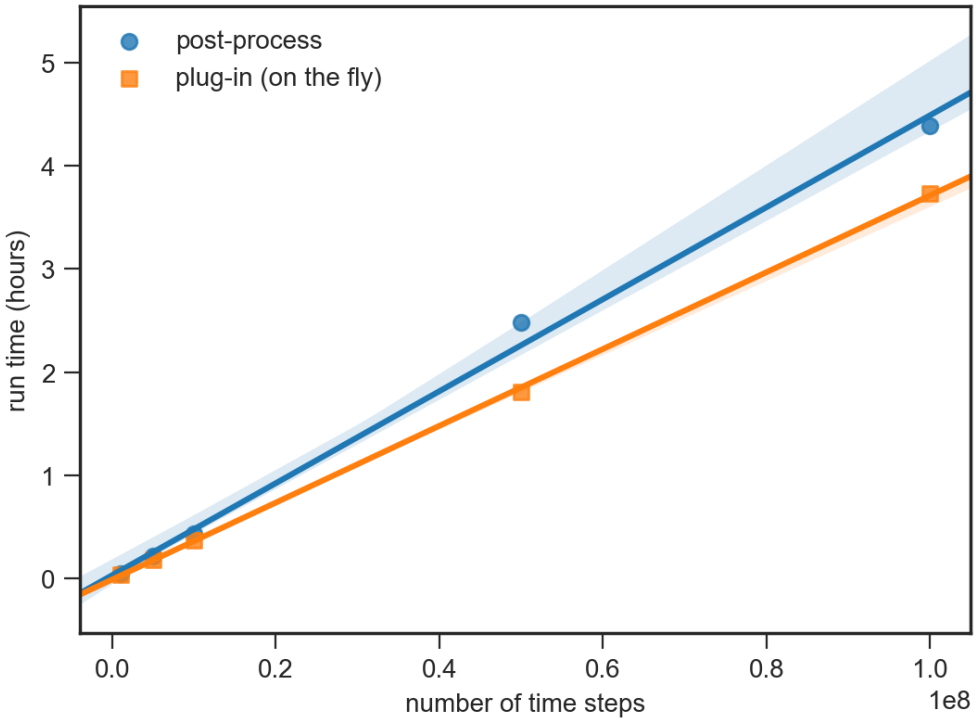

Figure 5.3: Performance data for post-processed and plug-in data. Number of time steps refers to the number of time steps after a 1×10^5 equilibration run. Shaded regions represent a 95% confidence interval.

It is important to note that quantifying this improved efficiency as a percent speed increase would be arbitrary, as the reduced time is only a function of time steps at which data is written. Instead, we present the decrease in time per time step as a metric for understanding the relative speeds. This is a rough calculation, but gives the order of magnitude of time that using the correlator as a plug-in offers as a speed up. It is common for simulations to run for 1×10^8 to 1×10^9 time steps, occasionally more. This translates to a time savings of 45 minutes to 7.5 hours for a single property to be calculated. For simulations where per-particle properties must be calculated, this time savings scales with the number of particles which is often on the order of 1×10^8.

The improved speed is only part of the advantage of the on the fly implementation. To use the correlator as a post-processing method, we must write every time step (or every period) to a file, then parse that file into input file for the correlator. This can result in data files that are several gigabytes for very long time scales. Just as with the run time, if we must calculate per-particle

values, this amount of memory can difficult to store and manage. The autocorrelation output files are only on the order of kilobytes, essentially eliminating the memory storage burden of the correlator.

Conclusions and Future Work In this section, we have produced an open-source functioning autocorrelation plug-in for HOOMD-blue. We also introduced additional features, such as the `evaluate()` function and periodic logging. Our performance testing demonstrates the improved efficiency of implementing the correlator as a plug-in. Currently, we have only tested on individual CPUs, and have not attempted running on GPUs or in parallel. Incorporating GPU compatibility should be a relatively straightforward process of adding in CUDA capabilities through flags in the plug-in. Achieving a correlator that works with a simulation running in parallel should also be straightforward as the entire plugin is lightweight and could be performed on a singular node without performance losses. The last high priority feature is restartable jobs. The framework is there in the periodic logging capabilities, but the process of reading in the multi-tau arrays to initialize the liktman correlator is non-trivial and was not a priority to develop.

Another area of improvement is adding more user-defined parameters. For example, the Likhtman correlator allows for m, p, and S parameters to be defined as a means of tuning error and efficiency. These would be simple to add into our plug-in, but would require additional unit testing. Other helpful plug-in arguments might be file parameters such as headers and delimiters to make plotting and processing the correlated data simpler for the user. It would also be beneficial to the user to include helpful error messages and warnings, which we have not yet included. Although Likhtman's mutiple-tau correlator is favorable for our research, some HOOMD users might prefer a linear correlator. In the future, we can add a linear correlation algorithm into the same plug-in.

5.3 Implementing Population Balance Brownian Dynamics in HOOMD-blue

A primary advantage of the Population Balance Brownian Dynamics method (Pop-BD) is that over the FENE-BD method is that its runtime and memory scale independently of the number of polymers in the system, since all the polymer chains are accounted for in the $N_{colloid} \times N_{colloid}$ bond matrix and a simple multiplicative factor to the transition rates and bond strengths. However, this means that the (usually) sparse bond matrix requires memory that scales as $\mathcal{O}(N^2)$. More critically, because Pop-BD was written as home-grown code that computes the interaction between *every* particle pair in the system at every time step, Pop-BD's runtime scales as $\mathcal{O}(N^2)$. In contrast, the open-source simulation software HOOMD-blue uses many advanced optimizations to perform huge simulations efficiently, but it does not offer the capability to add and remove bonds at runtime. In this section, we detail how we integrated the Pop-BD model into HOOMD-blue, including custom interparticle potentials and bridging transition rates from chapters 2 and 3, as well as a dynamic bonding functionality.

5.3.1 Intercolloidal Potentials

In chapter 2, we demonstrate that we can use self-consistent field theory (SCFT) to predict the loop-mediated repuslive interactions between colloids. To incorporate this new knowledge into Pop-BD, we use the `md.bond.table()` feature, which linearly interpolates a user-provided tabulated potential.

The potentials used to simulate colloids and their adsorbed polymer loops are dependent on the colloid radius, $R_{colloid}$, the number of polymers per colloid, $N_{polymer}$, the chain length of the polymers in Kuhn steps, N_{Kuhn}, and the fraction of chains that have only one sticker end, f_d. Note that, to define a tabluated bond potential using `md.bond.table()`, both the potential, $U(r)$ (denoted $V(r)$ in the HOOMD documentatin), as well as the force, $V(r)$, must be defined. The interparticle force is defined as $F(r) = -\partial V/\partial r$, so we simply calculate this derivative when

constructing the tabulated potential. Although the SCFT approach is highly efficient, we suggest keeping library of intercolloidal potentials, and only rerun the SCFT code needed to compute them for new parameter spaces. Fig. 5.4 shows intercolloidal potentials representative of those used in the updated Pop-BD method.

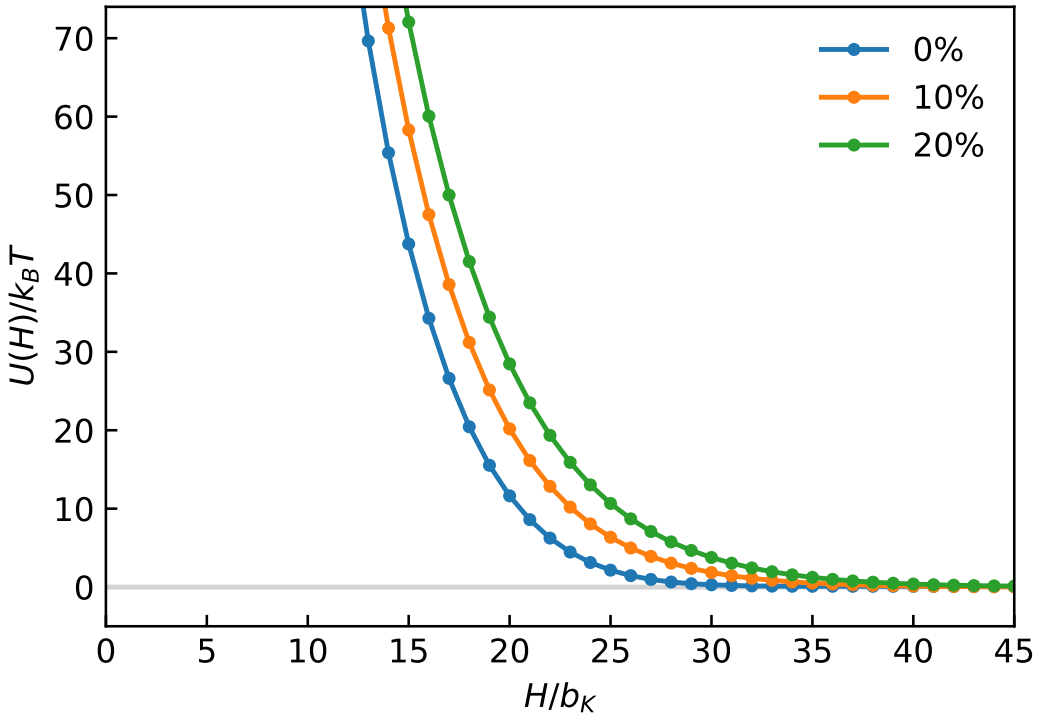

Figure 5.4: Intercolloidal potentials for $R_{colloid} = 60b_K$, $N_K = 200$, and $N_{polymer} = 500$ polymers per particle for 0, 10, and 20 percent of the polymers having only one sticker end (f_d).

5.3.2 Transition Rates

In chapter 3, we showed that loop-to-bridge transition rates can be computed from bridge-to-loop transition rates. We use this relationship when updating the Pop-BD method, but must adjust for the fact that the work in Ch. 3 studies polymer chains that have one sticker that is permanently adsorbed to its anchor wall. When a loop with two weak stickers transitions to a bridge, either sticker can break to form the bridge so that the transition rate is twice that of a a chain with one permanently adsorbed sticker. When a polymer bridging two colloids breaks, it forms a loop on

either particle with an average time of the time for a bridge with an anchored sticker to transition from bridge-to-loop, and so it does not require a correction factor. This means that the updated M and L rates are defined as follows:

$$L(d_{ij}) = 2 \times \frac{1}{\tau_{loop-to-bridge}} \tag{5.12}$$

$$M(d_{ij}) = \frac{1}{\tau_{bridge-to-loop}} \tag{5.13}$$

Similar to the `md.bond.table` feature in HOOMD-blue, we add a `set_rates_from_file()` method in the Pop-BD version of HOOMD-blue. An example of how rates are tabulated for input is shown in Table 5.2.

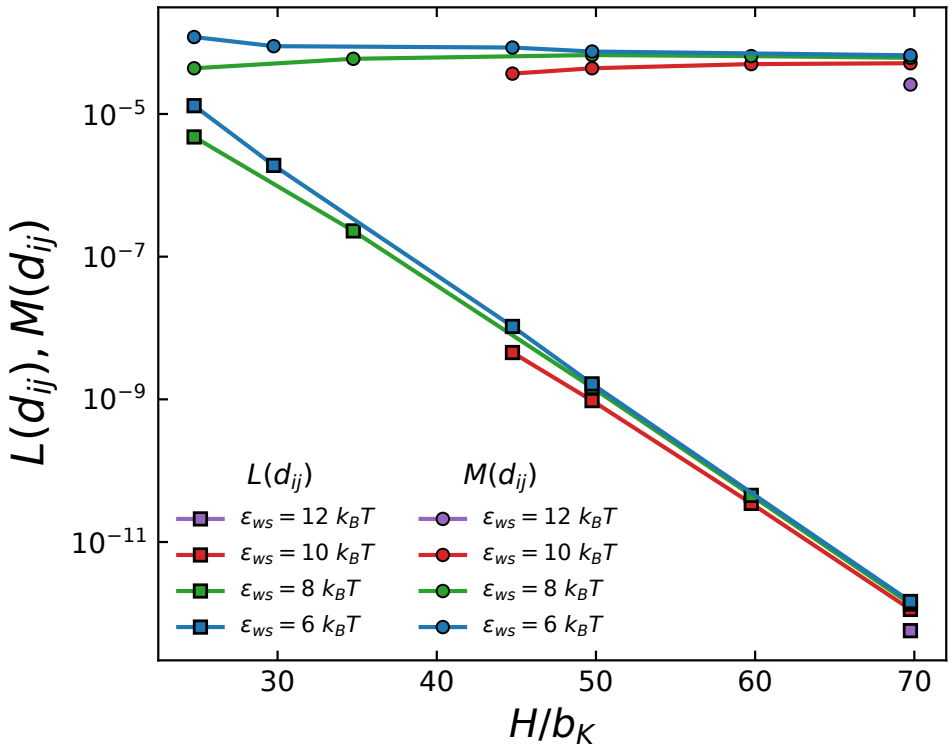

Figure 5.5: Rates for loop-to-bridge ($L(d_{ij})$, square markers) and bridge-to-loop ($M(d_{ij})$, circle markers) transitions.

d	M	L
120	0.0001	0.00008145
122	0.0001	0.00006989
124	0.0001	0.00005972
126	0.0001	0.00005069
128	0.0001	0.00004263
...	...	...

Table 5.2: An example of a reaction rates table used as input to the Pop-BD method in HOOMD-blue, where d is the center-to-center particle distance in units of b_K and the bridge-to-loop (L) and loop-to-bridge (M) rates are in units of $[t]^{-1}$ where the time unit for a Pop-BD simulation $[t]$ is typically taken to be 3.9×10^{-9} seconds.

5.3.3 Dynamic Bonding at Runtime in HOOMD-blue

The biggest challenge of improving the performance of Pop-BD was developing a way to modify HOOMD-blue such that we could add or remove bonds between arbitrary particle pairs during runtime. Trying to implement dynamic bonding at the Python level in HOOMD would require taking a simulation snapshot, reading it, evaluating bridge breakage and formation probablities, updating the snapshot, then re-loading it. Since Pop-BD updates the number of bridges and loops at every time step, it is necessary to develop a more efficient way to translate this to bond formation/breakage in HOOMD. We present a method of passing in the reaction rates, $M(d_{ij})$ and L_{ij}, on the Python level, and then using the PopBD equations on the C++ level of HOOMD-blue to compute the bond breakage and formation probabilities for particle pairs at run time. The solution provided here does re-introduce the time scaling dependency on the number of polymers in the system, since every polymer bridge is represented as a distinct bond in HOOMD-blue. However, this performance sacrifice is significantly less than the benefit gained from HOOMD's other performance enhancements, which vastly improve the time scaling with the number of colloids in the system.

The loop and bridge tracking is significantly different from the original Pop-BD code in that the number of loops on each particle is tracked in a `vector` object, `m_nloops`, where each entry is an `int` that stores the number loops on the particle whose particle tag corresponds to the vector

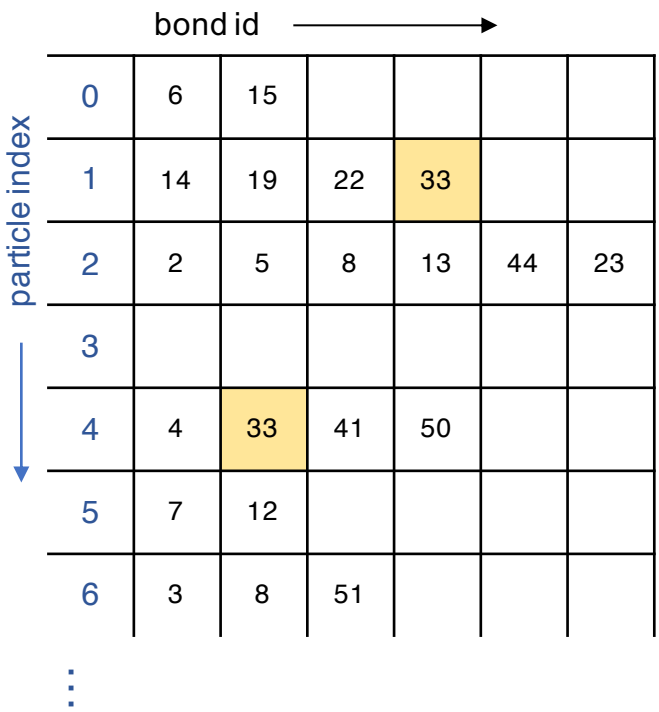

Figure 5.6: An example of a bond table as implemented in HOOMD-blue. Particle indexes are are shown in blue (leftmost column) and bond indexes are shown in black. In this given example, particles 1 and 4 are bonded by bond 33.

index. The number of bridges between particle pairs is stored in `m_nbonds`, a `map` object where the keys are a `pair` of particle tags, `(i, j)`, and the values are an `int` containing the number of bridges between particle pairs. However, `m_nbonds` is a convenience structure, and changing values in `m_nbonds` *will not update the number of bonds in the HOOMD simulation*. HOOMD uses a hash table type data structure to track the bonds in the system. This structure makes it possible to optimize HOOMD to run massively parallel simulations, but assumes that the topology of the system is static. It can be seen in Fig. 5.6 that this structure is not conducive to counting the number of bonds that each particle has, which is a crucial component of Pop-BD. The modifications made to HOOMD are only able to run on a single CPU, but as will be shown later in this section, the performance benefit is still significant.

To add a bond (representing a polymer bridge) between two particles with tags i and j, the **`addBondedGroup()`** method of `m_bond_data` is called, which takes the bond type (this version of

Pop-BD only allows one bond type, so the bond type is always `0`), and the particle tags of particles i and j. It is slightly more complicated to remove a bond from between particles i and j, since it is necessary to find the tag of the bond to remove. Removing a bond between a specific pair of particles requires iterating over all of the bonds in the *system*, and using the `getMembersByIndex` method of `m_bond_data`, which returns the particle pair bonded by the bond number passed to the function. The first bond that is found that connects particles i and j is then removed from the system using `removeBondedGroup`, which takes only the bond tag as an argument.

At each time step, the following actions are performed within the PopBD method.

---

update and access neighborlist
access the bond table, h_bond_table
m_delta_bonds = 0
for i in all particles **do**
  for j in in particle i's neighborlist **do**
    compute distance between i and j
    get number of loops particles i and j
    generate 4 random numbers
    compute bridge-to-loop and loop-to-bridge probabilities, P_{ij}, P_{ji}, Q_{ij}
    update `m_delta_bonds` to tabulate which particle pairs should have bonds added or deleted
  end for
end for
iterate through `m_delta_bonds` and remove or add bonds as necessary

Brownian dynamics and all other components of the simulation are performed elsewhere in HOOMD-blue. PopBD is called within a HOOMD simulation context. Below is an example of how PopBD might be called within a HOOMD simulation:

```
...
nl = md.nlist.cell()
integrator = md.integrate.mode_standard(dt=job.sp.timestep)
md.integrate.brownian(group=hoomd.group.all(), kT=1.0, seed=1)
popbd = md.update.popbd(table_width=rxn_width,
                        group=hoomd.group.all(),
                        nlist=neigh_list,
```

```
                            seed=1,
                            integrator=integrator,
                            period=1,
                            )
popbd.set_params(r_cut=75,
                 bond_type="polymer",
                 n_polymer=500
                 )
popbd.set_rates_from_file("rxn_rates.txt")
nl.reset_exclusions(exclusions=None)
```

Note that it is necessary to pass in a table of reaction rates as a text file, but also to pass in the expected length of the reaction rates table as an argument to the **`md.update.popbd()`** function. This is because memory must be allocated for the reaction rates tables upon intialization of the popbd object.

5.3.4 Performance Testing

We evaluate the performance of the HOOMD Pop-BD implementation against the original Pop-BD method as published by Hajizadeh and Larson [10]. A realistic runtime is 2×10^9 time steps, and so we represent the efficiency both as timesteps per second and the time required to run 2×10^9 time steps, as a practical measure. For both simulation methods, we run the simulation for a few minutes to get an approximation of the average timesteps per second, then use that value to compute how long it would take to run the simulations for 2×10^9 time steps. Fig. 5.7 shows that the original Pop-BD method scales as slightly less than $O(N^2)$, while the HOOMD implementation of Pop-BD scales as close to $O(N)$. This considerable speed-up has a significant practical payoff in that, for 240 particles, the time to run 2×10^9 time steps is on the order of 2 days instead of on the order of 2 weeks. A more robust performance analysis and code profiling would be valuable, as well as a comparison of memory required.

5.4 Conclusions and Future Work

The work in this chapter significantly improves the efficiency of simulations of waterborne coatings using the Pop-BD method by integrating both Pop-BD and an on-the-fly autocorrelation method into HOOMD-blue. Fig. 5.8 shows a diagram of how all of these components come together to generate a prediction of a stress-relaxation curve.

Both the autocorrelation and dynamic bonding components of this chapter can have great benefit to the greater scientific community if they are released as general, standalone packages. The autocorrelation plug-in is already offered as open-source software on github, but could benefit from more peer-review and some additional functionality such as compatability with restartable simulations and the ability to specify the p and m constants. The prodedure used to add, remove, and track bonds in the HOOMD-blue version of Pop-BD has applications beyond simulating waterborne coatings. This type of dynamic bonding is useful for modeling chemical reactions or

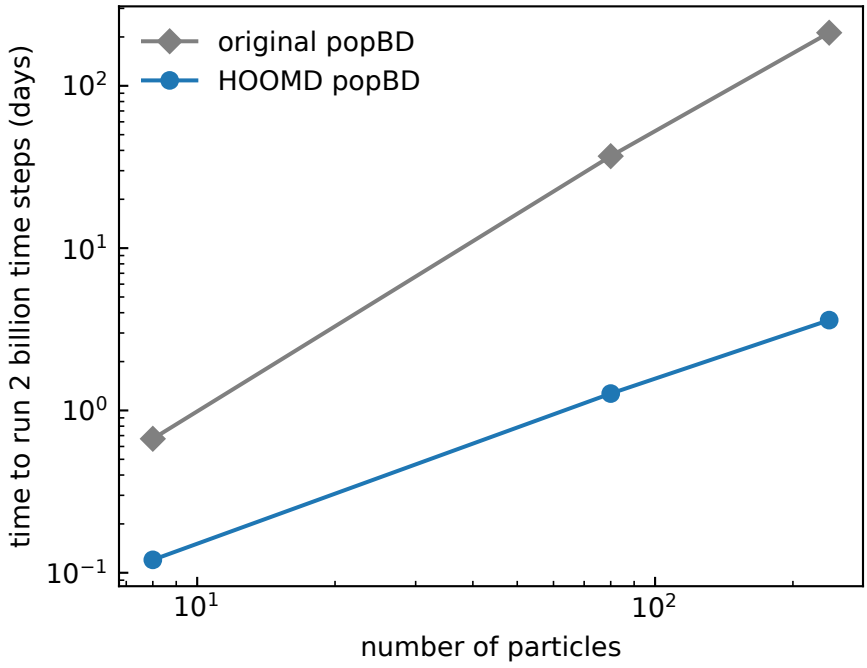

Figure 5.7: Time to run 2×10^9 time steps for the original Pop-BD implementation.

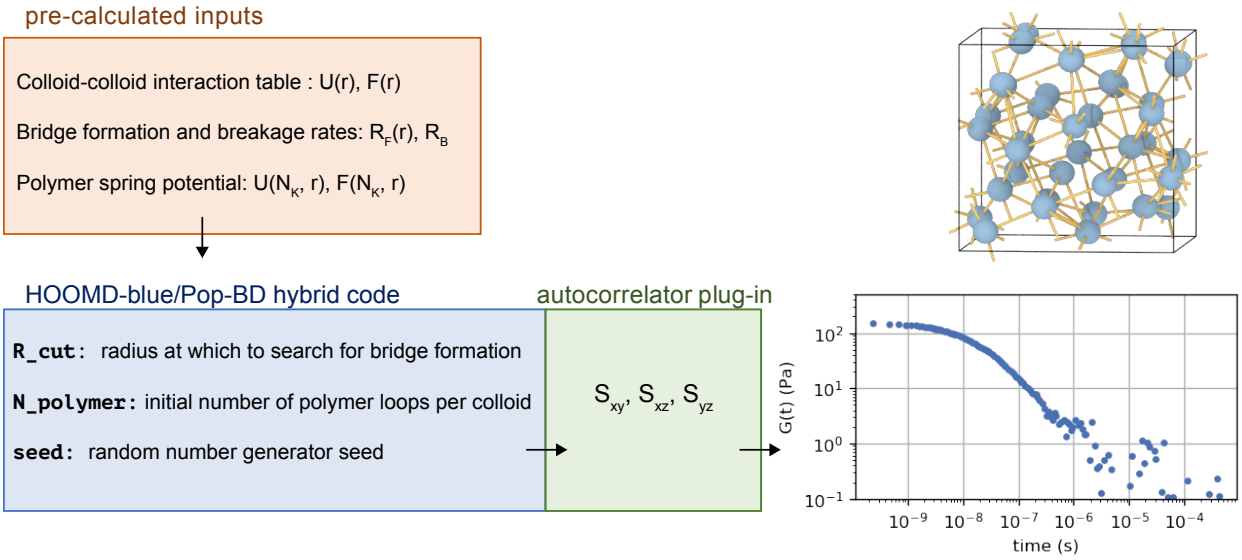

Figure 5.8: A diagram of a workflow using inputs calculated from BD simulations and SCFT (orange), the Pop-BD implementation of HOOMD-Blue (blue), and the on-the-fly autocorrelation method as a HOOMD plug-in (green). The output on the right is an example of the type of stress relaxation curve generated by this workflow.

any other type of dynamic network. Work would need to be done to develop a general API for dynamic bonding, and a bigger challenge would be to make dynamic bonding compatible with parallelization and/or GPU-based simulations.

The efficiency of the Pop-BD package could also be improved. As with a general dynamic bonding implementaiton, it would be incredibly beneficial ot expand Pop-BD to be functional in parallel or GPU-based simulations. If the drawback of representing polymer bridges explicitly becomes a limitation Pop-BD's efficiency, we recommend re-introducing bonds with a multiplicative factor, so that only one bond between particles could represent multiple bridges, as is done in the original Pop-BD method. This approach would require modifying the `bond` class in HOOMD and add a `mult` attribute, which would indicate the number of polymer bridges a given bond represents. We chose not to make this optimization so far, since the number of bonds between particle pairs has not been so high that it hindered performance.

CHAPTER 6

Conclusions and Future Work

6.1 Conclusions

In this work, we present a collection of studies that each contribute either improved accuracy or efficiency to the original Pop-BD method. Individually, each chapter presents an in-depth study of some element of the interactions between rheology-modifying polymers and colloidal particles, using waterborne coatings as a model system.

In chapter 2, we use both lattice self-consistent field theory and Brownian dynamics simulations to quantify the inter-colloidal interactions resulting from the excluded volume effects of HEUR polymers adsorbed on the colloid surfaces. The focus of this work was on the equilibrium distributions of the polymers and resulting effective interactions. We observed that the rearrangements of the polymers due to excluded volume and a "squeeze-out" effect result in non-uniform distributions on the colloids. Using the lattice SCFT method, we accounted for these non-uniform distributions and predicted both the purely-repulsive contributions of polymer loops as well as the total effective interaction potentials that result from a combination of loops and bridges at equilibrium. Monte Carlo simulations using the effective potentials to define colloid-colloid interactions provided insight into the phase stability of experimental systems under quiescent conditions, demonstrating the cruicial stabilizing effects of HEUR chains with only one hydrophobic end cap.

In chapter 3, we showed that the bridge-to-loop and loop-to-bridge transition times can be related using detailed-balance and self-consistent field theory predictions of equilibrium bridge and

loop configuration fractions. By empirically fitting a function to the $\phi_{bridge}/\phi_{loop}$ vs. $H/b_K\sqrt{N_K}$ curve to which 10, 40, and 200 Kuhn step chains all collapse, we present an approach to computing transition times that requires only Brownian dynamics simulations of the faster bridge-to-loop transition time. An analysis of the particle escape and spring retraction stages of the bridge-to-loop transition showed that the approximation that the hydrophobe desorption time is equal to the bridge-to-loop transition time is only valid for very short chains and very high sticker strengths. We ultimately present transition rates for experimentally-relevant chain lengths that can be incorporated into Pop-BD simulations.

Chapter 4 informed chapter 3, in that it focuses on the specific problem of a particle escaping from a Lennard-Jones potential well. We observed an error in prior simulations of polymer-colloid interactions that resulted from a lack of understanding of the effect of damping on the escape time of a particle, and the consquences of this for more complex simulations. This chapter provides a thorough assessment of existing theories' predictions for particle escape times for different damping regimes, and offers a comprehensive formula for predicting particle escape times from a Lennard-Jones potential for all damping conditions.

Finally, chapter 5 incorporates the information obtained from chapters 2 and 3 into a new implementation of Pop-BD. This updated version of Pop-BD is an extension of HOOMD-blue that breaks and forms bonds (representing HEUR bridges) during runtime, using the Pop-BD rate equations. Incorporating the open-source autocorrelation code provided by Ramirez et al. into HOOMD-blue as a plug-in module greatly improves the efficiency of computing stress relaxation curves from Pop-BD simulation data. Both the dynamic bonding developed as a part of the Pop-BD/HOOMD code and the Likhtman autocorrelator plug-in are features that are desired by the greater molecular simulation community.

6.2 Future Work

We know from experimental studies that under shear, the corona of loops on the surface of the colloids deforms anisotropically[56]. If this effect is pronounced, it might be interesting to introduce a force-dependent anisotropic potential that captures this effect. Additionally, we know that the results of the phase diagrams presented in chapter 2 qualitatively agree with experimental results through informal discussion with experimental collaborators, but it would be beneficial to conduct a thorough exploration of how the potentials computed in chapter 2 directly correspond to experimental results.

In chapter 3, we show that there are two regimes for the bridge-to-loop transition, one dominated by τ_{spring} and the other dominated by τ_{esc}. However, where the crossover between these two regimes occurs appears to be dependent on the interparticle gap and chain length of the polymers. Because of these complexities, we continue to use BD simulations to generate tabulated bridge-to-loop transition times. It would be preferable and more efficient to develop a theoretical, semi-empirical, or even machine learning approach to predicting bridge-to-loop transition times. This would allow for the exploration of a wider parameter space using Pop-BD without the need to re-run computationally expensive simulations.

The computational efficiency improvmenets shown in chapter 5 are not limited to the Pop-BD methodology. The autocorrelation method developed by Ramirez and coworkers has wide applications, and is already a part of the LAMMPS simulation package. With some more rigorous unit testing and additional features for flexiblity, the autocorrelation method could either be integrated into HOOMD v3, should there be enough user-interest, or simply be used as a stand-alone plug-in that is compatible with HOOMD-blue.

The modifications we made to HOOMD-blue that allow for bond breakage and formation during run time is a feature that has been requested by several HOOMD-blue users. Simplifying the Pop-BD code to just the dynamic bonding component, then generalizing it appropriately so that other users can apply it to their applicaitons, is an obvious next step. However, Pop-BD does not require massive system sizes to obtain valuable information, but many systems of interest to

HOOMD-blue users do. Because one of the primary reasons users choose HOOMD-blue is because of its ability to scale to large numbers of GPUs, a CUDA-compatible implementation of dynamic bonding should be developed before it is released as a component of HOOMD-blue.

Finally, this thesis presents few results of actual Pop-BD simulations, and instead focuses on the subcompoents and code development necessary to improve it. The ideal next steps for Pop-BD are to run large simulations for long timescale behavior, and begin comparing these results to experimental simulations. Specifically, introducing steady-shear to Pop-BD simulations has been a long-standing target for this project. The modularity of the Pop-BD/HOOMD code also offers opportunity for incorporating machine learning techniques, since it is likely that adjustments will need to be made upon comparison to experimental data. Behavior of waterborne coatings such as non-monotonic viscosity vs. shear curves, negative first normal stress, and G' and G" curves whose scaling are non-Maxwellian and difficult to predict are all of interest and Pop-BD may lend insight intno these areas.

BIBLIOGRAPHY

[1] K C Tam, R D Jenkins, M A Winnik, and D R Bassett. A Structural Model of Hydrophobically Modified Urethane-Ethoxylate (HEUR) Associative Polymers in Shear Flows. *Macromolecules*, 31:4149–4159, 1998.

[2] Ahmad Yekta, Bai Xu, Jean Duhamel, Hendra Adiwidjaja, and Mitchell A Winnik. Fluorescence Studies of Associating Polymers in Water: Determination of the Chain End Aggregation Number and a Model for the Association Process. *Macromolecules*, 28:956–966, 1995.

[3] K Devanand and J C Selser. Asymptotic Behavior and Long-range Interactions in Aqueous Solutions of Poly(ethylene oxide). *Macromolecules*, 24:5943–5947, 1991.

[4] Christopher B Stanley and Helmut H Strey. Measuring Osmotic Pressure of Poly(ethylene glycol) Solutions by Sedimentation Equilibrium Ultracentrifugation. *Macromolecules*, 36(18):6888–6893, 2003.

[5] Y C Chiew and E D Glandt. Percolation behaviour of permeable and of adhesive spheres. *Journal of Physics A: Mathematical and General*, 16(11):2599–2608, 1983.

[6] Q T Pham, W B Russel, and W Lau. Rheology of telechelic associative polymers in aqueous solutions. *Cit. J. Rheol.*, 42:979, 1998.

[7] John Stone. *An Efficient Library for Parallel Ray Tracing and Animation*. Master's thesis, Computer Science Department, University of Missouri-Rolla, April 1998.

[8] William Humphrey, Andrew Dalke, and Klaus Schulten. VMD – Visual Molecular Dynamics. *Journal of Molecular Graphics*, 14:33–38, 1996.

[9] Antony K Van Dyk, Tirtha Chatterjee, Valeriy V Ginzburg, and Alan I Nakatani. Shear-Dependent Interactions in Hydrophobically Modified Ethylene Oxide Urethane (HEUR) Based Coatings: Mesoscale Structure and Viscosity. *Macromolecules*, 2015.

[10] Elnaz Hajizadeh, Shi Yu, Shihu Wang, and Ronald G. Larson. A novel hybrid population balance—brownian dynamics method for simulating the dynamics of polymer-bridged colloidal latex particle suspensions. *Journal of Rheology*, 62(1):235–247, 2018.

[11] Hossein Rezvantalab and Ronald G Larson. Bridging Dynamics of Telechelic Polymers between Solid Surfaces. *Macromolecules*, 21:31, 2018.

[12] Baptiste Quienne, Julien Pinaud, Jean Jacques Robin, and Sylvain Caillol. From Architectures to Cutting-Edge Properties, the Blooming World of Hydrophobically Modified Ethoxylated Urethanes (HEURs). *Macromolecules*, 53(16):6754–6766, aug 2020.

[13] F Molenaar, T Svanholm, and A Toussaint. Rheological behaviour of latexes in-can and during film drying. *Prog. Org. Coatings*, 31:141–158, 1997.

[14] A N Semenov, J.-F Joanny, and A R Khokhlov. Associating Polymers: Equilibrium and Linear Viscoelasticity. *Macromolecules*, 28:1066–1075, 1995.

[15] Tom Annable, Richard Buscall, Rammile Ettelaie, and Diane Whittlestone. The rheology of solutions of associating polymers: Comparison of experimental behavior with transient network theory. *J. Rheol. (N. Y. N. Y).*, 37(4):695–726, 1993.

[16] F Tanaka and SF Edwards. Viscoelastic properties of physically crosslinked networks Part 3. Time-dependent phenomena. *J. Non-Newtonian Fluid Mech. Non-Newtonian Fluid Mech*, 43(43):289–309, 1992.

[17] Valeriy V. Ginzburg, Tirtha Chatterjee, Alan I. Nakatani, and Antony K. Van Dyk. Oscillatory and Steady Shear Rheology of Model Hydrophobically Modified Ethoxylated Urethane-Thickened Waterborne Paints. *Langmuir*, 34(37):10993–11002, sep 2018.

[18] Kebede Beshah, Aslin Izmitli, Antony K Van Dyk, John J Rabasco, James Bohling, and Susan J Fitzwater. Diffusion-Weighted PFGNMR Study of Molecular Level Interactions of Loops and Direct Bridges of HEURs on Latex Particles. *Macromolecules*, 46:2216–2227, 2013.

[19] Fang Yuan and Ronald G Larson. Multiscale Molecular Dynamics Simulations of Model Hydrophobically Modified Ethylene Oxide Urethane Micelles. *J. Phys. Chem. B*, 119:29, 2015.

[20] Shihu Wang and Ronald G Larson. A Coarse-Grained Implicit Solvent Model for Poly(ethylene oxide), CnEm Surfactants, and Hydrophobically End-Capped Poly(ethylene oxide) and Its Application to Micelle Self-Assembly and Phase Behavior. *Macromolecules*, 48:7709–7718, 2015.

[21] Valeriy V Ginzburg, Antony Keith, Van Dyk, Tirtha Chatterjee, Alan Isamu Nakatani, Shihu Wang, and Ronald G Larson. Modeling the Adsorption of Rheology Modifiers onto Latex Particles Using Coarse-Grained Molecular Dynamics (CG-MD) and Self-Consistent Field Theory (SCFT). *Macromolecules*, 48:8045–8954, 2015.

[22] Shihu Wang and Ronald G Larson. Multiple relaxation modes in suspensions of colloidal particles bridged by telechelic polymers. *J. Rheol. (N. Y. N. Y).*, 62:371, 2018.

[23] Hsieh Chen and Alfredo Alexander-Katz. Structure and dynamics of blood-clotting-inspired polymer-colloid composites. *Soft Matter*, 9:10381–10390, 2013.

[24] Hsieh Chen, Mohammad A Fallah, Volker Huck, Jennifer I Angerer, Armin J Reininger, Stefan W Schneider, Matthias F Schneider, and Alfredo Alexander-Katz. Blood-Clotting-Inspired Reversible Polymer–Colloid Composite Assembly in Flow. *Nature Communications*, 4(1):1333, 2013.

[25] Tirtha Chatterjee, Alan I. Nakatani, and Antony K. Van Dyk. Shear-dependent interactions in hydrophobically modified ethylene oxide urethane (heur) based rheology modifier–latex suspensions: Part 1. molecular microstructure. *Macromolecules*, 47(3):1155–1174, 2014.

[26] Federica Lo Verso, Leonid Yelash, Sergei A Egorov, and Kurt Binder. Effect of the Solvent Quality on the Structural Rearrangement of Spherical Brushes: Coarse-Grained Models. *Soft Matter*, 8:4185–4196, 2012.

[27] Federica Lo Verso, Leonid Yelash, Sergei A. Egorov, and Kurt Binder. Interactions between polymer brush-coated spherical nanoparticles: the good solvent case. *The Journal of Chemical Physics*, 135(21):214902, 2011.

[28] Scott T Milner and Thomas A Witten. Bridging Attraction by Telechelic Polymers. *Macromolecules*, 25:5495–5503, 1992.

[29] Surita R Bhatia and William B Russel. End-Capped Associative Polymer Chains Between Nanospheres: Attractions in Ideal Solutions. *Macromolecules*, 33(15):5713–5720, 2000.

[30] Xiao-Xia Meng and William B Russel. Telechelic Associative Polymers: Interaction Potential and High Frequency Modulus. *Journal of Rheology*, 50(2):169–187, feb 2006.

[31] Vincent Testard, Julian Oberdisse, and Christian Ligoure. Monte Carlo Simulations of Colloidal Pair Potential Induced by Telechelic Polymers: Statistics of Loops and Bridges. *Macromolecules*, 41(19):7219–7226, 2008.

[32] E B Zhulina and A Halperin. Lamellar Mesogels and Mesophases: A Self-Consistent-Field Theory. *Macromolecules*, 25(21):5730–5741, 1992.

[33] S T Milner, T A Witten, and M E Cates. Theory of the Grafted Polymer Brush. *Macromolecules*, 21(8):2610–2619, August 1988.

[34] S T Milner. Polymer Brushes. *Science*, 251:905–914, 1991.

[35] G Subramanian, D.R.M Wulliams, and P. A. Pincus. Escape Transitions and Force Laws for Compressed Polymer Mushrooms. *Europhysics Letters*, 29(4):285–290, feb 1995.

[36] J M H M Scheutjens and G J Fleer. Statistical Theory of the Adsorption of Interacting Chain Molecules. 1. Partition function, Segment Density Distribution, and Adsorption Isotherms. *The Journal of Physical Chemistry*, 83(12):1619–1635, jun 1979.

[37] J M H M Scheutjens and G J Fleer. Statistical Theory of the Adsorption of Interacting Chain Molecules. 2. Train, Loop, and Tail Size Distribution. *The Journal of Physical Chemistry*, 84(2):178–190, jan 1980.

[38] Michelle D Lefebvre, Monica Olvera de la Cruz, and Kenneth R Shull. Phase Segregation in Gradient Copolymer Melts. *Macromolecules*, 37(3):1118–1123, feb 2004.

[39] Nicholas B Tito, Scott T Milner, and Jane E G Lipson. Self-assembly of Lamellar Microphases in Linear Gradient Copolymer Melts. *Macromolecules*, 43(24):10612–10620, dec 2010.

[40] Nicholas B Tito, Scott T Milner, and Jane E G Lipson. Ball-of-yarn Conformation of a Linear Gradient Copolymer in a Homopolymer Melt. *Macromolecules*, 45(18):7607–7620, sep 2012.

[41] S T Milner. Compressing Polymer "Brushes": a Quantitative Comparison of Theory and Experiment. *Europhysics Letters*, 7(8):695, dec 1988.

[42] Valeriy V Ginzburg, Antony Keith Van Dyk, Tirtha Chatterjee, Alan Isamu Nakatani, Shihu Wang, and Ronald G Larson. Modeling the Adsorption of Rheology Modifiers onto Latex Particles Using Coarse-Grained Molecular Dynamics (CG-MD) and Self-Consistent Field Theory (SCFT). *Macromolecules*, 48(21):8045–8054, November 2015.

[43] R J Baxter. Method of Solution of the Percus-Yevick, Hypernetted-Chain, or Similar Equations. *Physical Review*, 154(1):170–174, February 1967.

[44] R J Baxter. Percus–Yevick Equation for Hard Spheres with Surface Adhesion. *The Journal of Chemical Physics*, 49(6):2770–2774, September 1968.

[45] Peter J Lu, Emanuela Zaccarelli, Fabio Ciulla, Andrew B Schofield, Francesco Sciortino, and David A Weitz. Gelation of Particles with Short-range Attraction. *Nature*, 453(7194):499, May 2008.

[46] N. A. Seaton and E. D. Glandt. Aggregation and percolation in a system of adhesive spheres. *The Journal of Chemical Physics*, 86(8):4668–4677, 1987.

[47] Mark A Miller and Daan Frenkel. Competition of Percolation and Phase Separation in a Fluid of Adhesive Hard Spheres. *Physical Review Letters*, 90(13):135702, April 2003.

[48] Felix Seiferling, Daniel de las Heras, and Margarida M. Telo da Gama. Percolation in binary and ternary mixtures of patchy colloids. *The Journal of Chemical Physics*, 145(7):074903, 2016.

[49] J A Anderson, C D Lorenz, and A Travesset. General purpose molecular dynamics simulations fully implemented on graphics processing units. *Journal of Computational Physics*, 227(10):5342–5359, may 2008.

[50] Joshua A. Anderson, M. Eric Irrgang, and Sharon C. Glotzer. Scalable Metropolis Monte Carlo for Simulation of Hard Shapes. *Comput. Phys. Commun.*, 204:21–30, jul 2016.

[51] Michael P. Howard, Joshua A. Anderson, Arash Nikoubashman, Sharon C. Glotzer, and Athanassios Z. Panagiotopoulos. Efficient neighbor list calculation for molecular simulation of colloidal systems using graphics processing units. *Comput. Phys. Commun.*, 203:45–52, jun 2016.

[52] L Martínez, R Andrade, E G Birgin, and J M Martínez. Packmol: A package for building initial configurations for molecular dynamics simulations. *Journal of Computational Chemistry*, 30(13):2157–2164, 2009.

[53] Ł Baran and S Sokołowski. Effective Interactions between a Pair of Particles Modified with Tethered Chains. *The Journal of Chemical Physics*, 147:44903, 2017.

[54] F Tanaka and S.F. Edwards. Viscoelastic properties of physically crosslinked networks Part 2. Dynamic mechanical moduli. *J. Nonnewton. Fluid Mech.*, 43:273–288, 1992.

[55] Anubhav Tripathi, Kam C Tam, and Gareth H. McKinley. Rheology and dynamics of associative polymers in shear and extension: Theory and experiments. *Macromolecules*, 39(5):1981–1999, 2006.

[56] Tirtha Chatterjee, Alan I. Nakatani, and Antony K. Van Dyk. Shear-dependent interactions in hydrophobically modified ethylene oxide urethane (heur) based rheology modifier–latex suspensions: Part 1. molecular microstructure. *Macromolecules*, 47(3):1155–1174, 2014.

[57] Tirtha Chatterjee, Antony K Van Dyk, Valeriy V Ginzburg, and Alan I Nakatani. Formulation-Controlled Positive and Negative First Normal Stress Differences in Waterborne Hydrophobically Modified Ethylene Oxide Urethane (HEUR)-Latex Suspensions. *ACS Macro Lett.*, 6:716–720, 2017.

[58] Wenlin Zhang, Alyssa Travitz, and Ronald G. Larson. Modeling Intercolloidal Interactions Induced by Adsorption of Mobile Telechelic Polymers onto Particle Surfaces. *Macromolecules*, 52(14):5357–5365, jul 2019.

[59] Michael Rubinstein and Ralph H. Colby. *Polymer Physics*. Oxford University Press, 2003.

[60] Joshua A. Anderson, Jens Glaser, and Sharon C. Glotzer. HOOMD-blue: A Python package for high-performance molecular dynamics and hard particle Monte Carlo simulations. *Comput. Mater. Sci.*, 173(April 2019):109363, 2020.

[61] Richard S. Larson and Edwin J. Lightfoot. Thermally activated escape from a Lennard-Jones potential well. *Phys. A Stat. Mech. its Appl.*, 149(1-2):296–312, mar 1988.

[62] P. S. Virk. Drag reduction fundamentals. *AIChE J.*, 21(4):625–656, 1975.

[63] Alyssa Travitz, Ethayaraja Mani, and Ronald G. Larson. Transitioning from underdamped to overdamped behavior in theory and in Langevin simulations of desorption of a particle from a Lennard-Jones potential. *J. Rheol.*, 2021.

[64] Carl S. Adorf, Paul M. Dodd, Vyas Ramasubramani, and Sharon C. Glotzer. Simple data and workflow management with the signac framework. *Comput. Mater. Sci.*, 146:220–229, apr 2018.

[65] J. Towns, T. Cockerill, M. Dahan, I. Foster, K. Gaither, A. Grimshaw, V. Hazlewood, S. Lathrop, D. Lifka, G. D. Peterson, R. Roskies, J. Scott, and N. Wilkins-Diehr. Xsede: Accelerating scientific discovery. *Computing in Science & Engineering*, 16(05):62–74, sep 2014.

[66] Michael P. Howard, Arash Nikoubashman, and Athanassios Z. Panagiotopoulos. Stratification in Drying Polymer–Polymer and Colloid–Polymer Mixtures. *Langmuir*, 33(42):11390–11398, aug 2017.

[67] Ahmad K Omar and Zhen-Gang Wang. Shear-Induced Heterogeneity in Associating Polymer Gels: Role of Network Structure and Dilatancy. *Phys. Rev. Lett.*, 119, 2017.

[68] Hao Wu, Jeffrey M. Ting, Boyuan Yu, Nicholas E. Jackson, Siqi Meng, Juan J. de Pablo, and Matthew V. Tirrell. Spatiotemporal Formation and Growth Kinetics of Polyelectrolyte Complex Micelles with Millisecond Resolution. *ACS Macro Lett.*, 9(11):1674–1680, nov 2020.

[69] Ting Ge, Michael Rubinstein, and Gary S. Grest. Effects of Tethered Polymers on Dynamics of Nanoparticles in Unentangled Polymer Melts. *Macromolecules*, 0(0), aug 2020.

[70] Steve Plimpton. Fast Parallel Algorithms for Short-Range Molecular Dynamics. *J. Comput. Phys.*, 117(6):1–19, 1995.

[71] H.A. Kramers. Brownian motion in a field of force and the diffusion model of chemical reactions. *Physica*, 7(4):284–304, apr 1940.

[72] V. I. Mel'nikov and S. V. Meshkov. Theory of activated rate processes: Exact solution of the Kramers problem. *J. Chem. Phys.*, 85(2):1018–1027, jul 1986.

[73] Eli Pollak and Joachim Ankerhold. Improvements to Kramers turnover theory. *J. Chem. Phys.*, 138:164116, 2013.

[74] Jorge Ramirez, Sathish K Sukumaran, Bart Vorselaars, and Alexei E Likhtman. Efficient on the fly calculation of time correlation functions in computer simulations. *The Journal of Chemical Physics*, 133, 2010.